Ultrafast Electron Dynamics in Fe(CO)$_5$ and Cr(CO)$_6$

Dissertation

zur Erlangung des akademischen Grades
doctor rerum naturalium
(Dr. rer. nat.)
in der Wissenschaftsdisziplin
Experimentalphysik

eingereicht an der
Mathematisch-Naturwissenschaftlichen Fakultät
der Universität Potsdam

von
Henning Schröder

Potsdam und Berlin, 2016

Abstract

In this thesis, the two prototype catalysts $Fe(CO)_5$ and $Cr(CO)_6$ are investigated with time-resolved photoelectron spectroscopy at a high harmonic setup. In both of these metal carbonyls, a UV photon can induce the dissociation of one or more ligands of the complex. The mechanism of the dissociation has been debated over the last decades. The electronic dynamics of the first dissociation occur on the femtosecond timescale.

For the experiment, an existing high harmonic setup was moved to a new location, was extended, and characterized. The modified setup can induce dynamics in gas phase samples with photon energies of $1.55\,eV$, $3.10\,eV$, and $4.65\,eV$. The valence electronic structure of the samples can be probed with photon energies between $20\,eV$ and $40\,eV$. The temporal resolution is $111\,fs$ to $262\,fs$, depending on the combination of the two photon energies.

The electronically excited intermediates of the two complexes, as well as of the reaction product $Fe(CO)_4$, could be observed with photoelectron spectroscopy in the gas phase for the first time. However, photoelectron spectroscopy gives access only to the final ionic states. Corresponding calculations to simulate these spectra are still in development. The peak energies and their evolution in time with respect to the initiation pump pulse have been determined, these peaks have been assigned based on literature data. The spectra of the two complexes show clear differences. The dynamics have been interpreted with the assumption that the motion of peaks in the spectra relates to the movement of the wave packet in the multidimensional energy landscape. The results largely confirm existing models for the reaction pathways. In both metal carbonyls, this pathway involves a direct excitation of the wave packet to a metal-to-ligand charge transfer state and the subsequent crossing to a dissociative ligand field state. The coupling of the electronic dynamics to the nuclear dynamics could explain the slower dissociation in $Fe(CO)_5$ as compared to $Cr(CO)_6$.

Contents

List of Abbreviations

BBO   bariummetaborat

BESSY   Berliner Elektronenspeicherring für Synchrotron-
                    strahlung

CP   calcite plate

DFT   density functional theory

EMG   exponentially modified Gaussian

ESCA   electron spectroscopy of chemical analysis

FLASH   free-electron-laser in Hamburg

FWHM   full width at half maximum

GDD   group delay dispersion

GRENOUILLE   grating-eliminated no-nonsense observation of ultrafast
                    incident laser light e-fields

HH   high harmonics

HHG   high harmonic generation

HOMO   highest occupied molecular orbital

LF   ligand field

LUMO   lowest unoccupied molecular orbital

MCP   micro-channel plate

MLCT   metal-to-ligand charge transfer

PE   photoelectron

PES   photoelectron spectroscopy

PMT   photomultiplier tube

SB	sideband
SFG	sum-frequency generation
SHG	second harmonic generation
SMA	SubMiniature version A
SPIDER	spectral phase interferometry for direct electric-field reconstruction
THG	third harmonic generation
trPES	time-resolved photoelectron spectroscopy
WP	waveplate

Introduction

Catalysts are essential for the modern lifestyle. Catalysts can reduce the activation energy and improve the rate of a reaction. One example for a catalytic reaction is the Haber-Bosch process. The development of the Haber-Bosch process in the first half of the 20$^{\text{th}}$ century allowed the production of ammonia on an industrial scale [1]. Ammonia is a precursor for fertilizers which strongly increase agricultural yields. Thereby, ammonia sustains about 40 % of the world's population [2]. Feeding the population of this planet would be difficult without it. Other important industrial applications of catalysis include the production of synthesis gas and the cracking of crude oil.

The market integration of renewable energies today requires the improvement of energy storage. Splitting water into hydrogen and oxygen via a catalyst presents one possible solution to this problem. Such a system is active in the oxygen-evolving complex in all photosynthetic organisms on this planet. The complex requires the energy of four photons of visible light in order to split two water molecules. The photons are collected stepwise, and the energy is stored in oxidizing equvilants. Each photon removes one electron from the complex. The combined energy is released in one step and splits the water molecules [3]. Understanding the details of this natural catalyst or designing an efficient artificial photocatalyst remains one of the grand challenges of our times.

For this purpose, the absorption of light by a molecule has to be studied at a fundamental level. Light-induced processes such as vibrational relaxation, vibrational motion, and dissociation reactions take place on the ultrafast timescale i.e., on the order of femto- to picoseconds [4]. A photon can change the electronic structure of a molecule, thereby promoting it from the ground state to an excited state. The properties of the molecule in the excited state can differ significantly from the ground state species. The nuclei adapt to the changes in the electronic configuration. In photocatalysts, the excited state can lead to a reactive intermediate or induce a photodissociation followed by additional chemical reactions on the ultrafast timescale [5].

In this thesis, I study the photodissociation of metal carbonyls. A metal carbonyl $M_m(CO)_n$ is a complex composed of m metals with n carbonyl ligands. The metal-carbonyl $Fe(CO)_5$ is a prototype catalyst. $Fe(CO)_5$ is stable at ambient conditions. A UV photon causes the dissociation of the complex into smaller fragments including the reactive intermediate $Fe(CO)_4$. This undersaturated intermediate is known to activate the C-H bond [6, 7]. The photodissociation of $Fe(CO)_5$ occurs ultrafast i.e., in under 100 fs. The details of the dissociation have been debated in the last decades [8]. As part of this debate, the question rose whether the ligands are lost sequentially or

concertedly. Experimental results could be found for both scenarios. Other questions in the debate are: What states are involved in the reaction, and what are the energies of these states? How does the electronic and the nuclear structure change during the reaction? Is a spin-flip involved and what are the differences between the reactions in the gas phase and the liquid phase?

Various techniques have contributed to provide a detailed picture of the dynamics. The current model of the reaction describes how the UV photon brings the molecule into an electronically excited state. From there, $Fe(CO)_5$ decays in less than $100\,fs$ to $Fe(CO)_4 + CO$ [9]. Observing the short-lived excited-state intermediates and determining the rate of the reaction steps has been difficult. Separating the different species at a sufficient time resolution is challenging for many experimental methods. Can I revise the model for the photodissociation or even find a new perspective on the dynamics of $Fe(CO)_5$? This endeavor requires a method, which can probe the electronic structure during the reaction. Techniques based on light, such as synchrotrons, X-ray free electron lasers, and high harmonic generation sources, give us access to these dynamics. They can deliver femtosecond light pulses and the photon energies necessary to study the valence electrons that participate in the bonding. Synchrotrons and X-ray free electron lasers are well suited if the experimental method requires reaching deep core levels or high brilliance. In comparison, high harmonic generation sources are jitter-free and independent of a large-scale facility. Such sources can probe the occupied valence states via photoelectron spectroscopy. A time-resolved measurement allows for the observation of changes in the electronic configuration or, in other words, the electronic dynamics.

I have modified and characterized an existing high harmonic setup at the Helmholtz-Zentrum Berlin. The setup, its improvements, and its characterization are described in detail in chapter two. With this setup, I have induced the photodissociation in two metal carbonyls: iron pentacarbonyl $[Fe(CO)_5]$ and chromium hexacarbonyl $[Cr(CO)_6]$ in the gas phase. The dissociation is initiated with a UV-vis pulse. A second extreme UV pulse probes the electronic structure via photoelectron spectroscopy. I can resolve the dynamics in the dimension of time by varying the delay between the two pulses. For the first time, electronically excited intermediate states of $Fe(CO)_5$ in the gas phase can be detected with photoelectron spectroscopy. The spectra allow us to draw conclusions on the pathways along the potential energy curves. The results largely confirm the latest model on the excited-state dynamics of $Fe(CO)_5$. The preliminary analysis of the $Cr(CO)_6$ spectra can also be interpreted in agreement with current models. In this study, the dynamics of the two metal carbonyls are compared. The electronic structure, the photoelectron spectra, and the pathways in the energy landscape are discussed in chapter three.

Chapter 2

# Time Resolved Photoelectron Spectroscopy with High Harmonic Generation

2.1 Photoelecton Spectroscopy

Photoelectron spectroscopy (PES) is an element specific spectroscopic technique to measure the binding energy of electrons in molecules, in liquids, and on surfaces. The technique is based on the external photoelectric effect, discovered by G. Hertz and interpreted by A. Einstein. The photon energy E_{ph} is equal to the product of the Planck constant h and the frequency of the light ν: $E_{ph} = h\nu$. To remove an electron from a sample in the gas phase, E_{ph} has to be greater than the binding energy E_{bin} of the electron. The free electron then carries the excess photon energy as kinetic energy E_{kin}

$$E_{kin} = h\nu - E_{bin} \tag{2.1}$$

With higher photon energy, stronger bound electrons can be extracted and studied. The development of XUV and X-ray sources allowed access to lower laying valence states and even core states. K. Siegbahn et al. discovered that shifts of the binding energy reveal information on the chemical state and the local environment of the sample [10, 11]. He and his group used PES and founded the field of Electron Spectroscopy of Chemical Analysis (ESCA). Historically, the core levels were first used for the chemical analysis. In the sixties, the valence electronic states came into focus [12]. PES allows one to measure occupied valence electronic states. The molecule CO in the ground state, for example, has six occupied orbitals, as illustrated in Figure 2.1 a). The diagram presents a single-electron picture. The photoelectron spectrum of the valence states is shown in Figure 2.1 b). The spectrum presents a multi-electron picture. The relative intensities in the spectrum are proportional to the cross-section which depends on the photon energy. The molecular orbital diagram and the spectrum will be discussed in chapter three.
We can see that the orbitals energies are similar to the location of the peaks. However, PES does not allow for the direct observation of the ground state. When probing a molecule, with N electrons, at least one electron is removed by the light to investigate the structure. However, the electron tells us only about the configuration of the
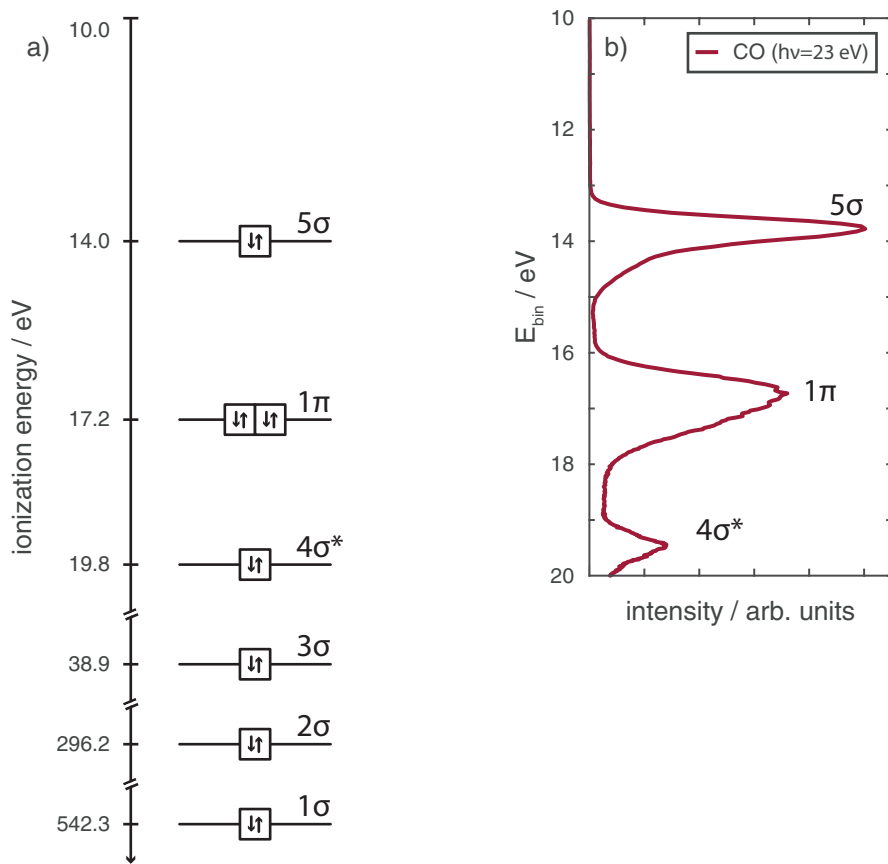
Figure 2.1: a) A molecular orbital diagram for carbon monoxide. The energies are taken from Reference [13]. b) The photoelectron spectrum of the carbon monoxide (gas phase) valence states, as measured.

molecule with $N-1$ electrons, which we call the final ionic state. The kinetic energy of the free electron reveals only information about the projection of the ground state onto the final ionic state.

Let us consider the following scenarios to understand the impact of this limitation: We probe a molecule with a XUV photon during a reaction, see Figure 2.2 a). The molecular potential depends on the reaction coordinate. A wave packet is lifted from the ground state (black line) into a virtual state in the vacuum (gray line). The kinetic energy of the free electron (green arrow) corresponds to the difference between the virtual state and the final ionic state (purple line). We measure the kinetic energy of the free electron at different points of the reaction coordinates. From the kinetic energy of the ejected electrons, the potential energy curve of the ground state is calculated. In this way, we approximate the potential curve (black circles) on which the electron was prior to the arrival of the XUV photon. In the approximation known as Koopmans's theorem the binding energy or ionization energy of the electron is equal in magnitude to the orbital energy [14]. In this case [a)], the potential is well approximated because the final ionic state does not strongly depend on the reaction coordinate.

However, the experimental results can differ if the final ionic state is not constant. An example is illustrated in case b). Here, the final ionic state considerably depends on the reaction coordinate. This results in a large difference between the actual ground state potential and the calculated potential. In our experiment, we probe an

electronically excited state. This situation is illustrated in case c). A photon (red arrow) lifts the wave packet into an excited state (yellow line) before the system is probed. The nearly constant final ionic state allows a good approximation of the excited state potential curve. In case d), the final ionic state dependence significantly on the reaction coordinate. The excited state potential and its approximation differ to a larger extent as compared to case c). In quantum mechanical calculations the effect of the final ionic state can be switched on and off. The calculations enable the transfer from experimental observations on complexes with $N-1$ electrons to complexes with N electrons.

From this line of thought, we learn about the limitations of PES and the importance of calculations. The calculation of the final ionic state holds the key to interpreting and understanding the experimental results.
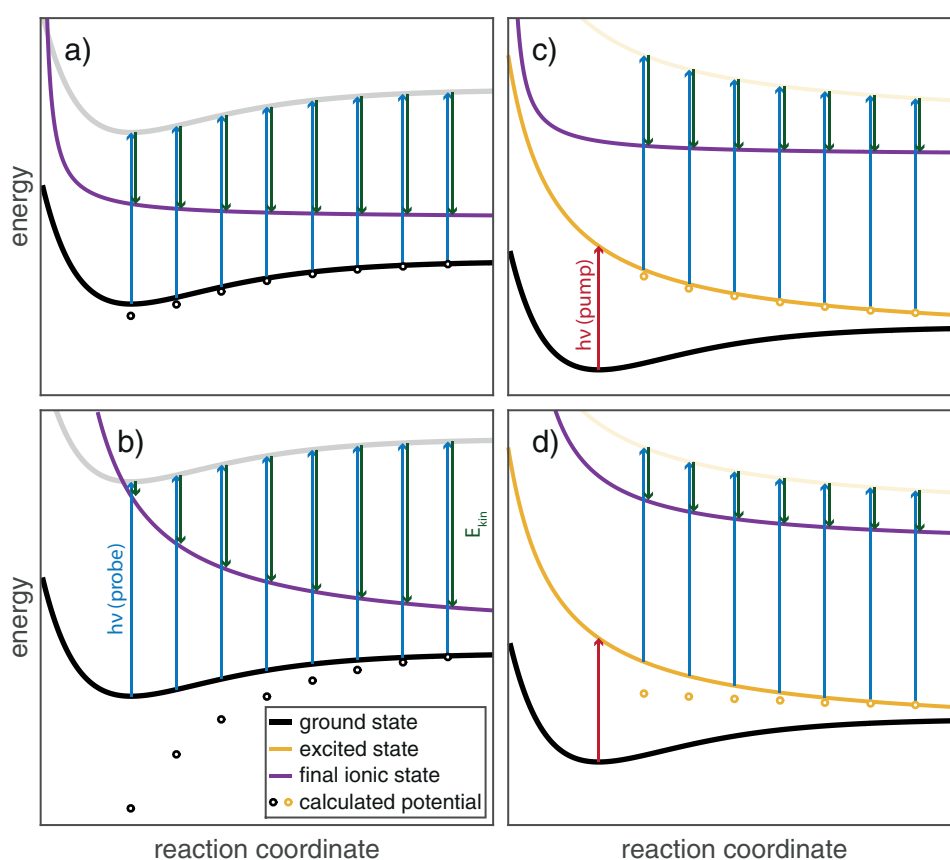
Figure 2.2: An illustration of the of the measurement process with photoelectron spectroscopy. A sample in the ground state (a and b) or in the excited state (c and d) is probed with an XUV photon. The original potential of the electron is approximated from the kinetic energy of the electron. The dependence of the final ionic state on the reaction coordinate limits the quality of this approximation.

2.2 Ultrafast Lasers

Ultrafast lasers are pulsed sources where each pulse has a duration of atto- to nanoseconds. A laser pulse can be understood as the temporal variation of an electromagnetic field $E(t)$

$$E(t) = E_0 \, e^{-(t/\tau)^2} e^{it\omega(t)} \tag{2.2}$$

t is the time, ω the frequency, and τ the duration of the pulse, the envelope of the electric field is $|E(t)|$. The observable is the intensity $I(t) = |E(t)|^2$. For a Gaussian pulse, I will refer to the Full With at Half Maximum (FWHM) of the intensity in the dimension of time $\Delta t_{FWHM} = 2\sqrt{2ln(2)}\tau$ as the duration of a pulse or as the temporal pulse length. The spectral width (FWHM), or bandwidth, is termed $\Delta\omega$. The two parameters Δt and $\Delta\omega$ are related through a Fourier transformation. Their product is limited by the following relationship

$$\Delta\omega\Delta t \geq 2\pi c_B \tag{2.3}$$

The constant c_B depends on the pulse shape and is 0.441 for an Gaussian pulse profile. Pulses, where $\Delta\omega\Delta t = 2\pi c_B$, are called 'bandwidth limited' or 'Fourier limited' [15, 16]. The spectral width of a bandwidth limited pulse is shown in Figure 2.3.

If such a pulse travels through an optical element, e.g. a lens, the pulse becomes chirped, that is the frequency components become separated in the dimension of time. It is the second order phase coefficient or group delay dispersion (GDD) ϕ" which linearly chirps the pulse

$$\phi" = \frac{\lambda^3 L}{2\pi c^2} \frac{d^2 n}{d\lambda^2} \tag{2.4}$$

L is the length and n the refractive index of the optical material, λ the wavelength, and c the speed of the light in the vacuum [17]. The duration of the chirped pulse Δt_{out} is

$$\Delta t_{out} = \sqrt{\Delta t^2 + \left(4\,ln(2)\frac{\phi"}{\Delta t_{in}}\right)^2} \tag{2.5}$$

The broadening of a $10\,mm$ BK7 glass ($\phi" = 43.96\,fs^2/mm$) is negligible for a $60\,fs$ pulse, but the effect is strong for a sub $30\,fs$ pulse, see Figure 2.3 c). The broadening for a $50\,fs$ pulse as a function of the path length in BK7 or fused silica is shown in Figure 2.3 d). Fused silica has a lower group delay dispersion than BK7 glass at the same wavelength. However, the pulse broadening is still more severe for a $266\,nm$ pulse in fused silica than for a $800\,nm$ pulse in BK7 glass [17]. For an experiment that aims for a sub-$100\,fs$ resolution, it is essential to minimize the temporal broadening. In my setup, I minimize the number of optical elements and the path length within these elements.

The light source for the setup is an amplified Ti:sapphire laser system (Red Dragon laser system from KM-Labs), which can deliver laser pulses of $44\,fs$ duration at a rate of $3\,kHz$ at a center wavelength of $795\,nm$. The pulse energy is $1.7\,mJ$. The beam has a diameter of $(7.7 \pm 0.1)\,mm$ and is p-polarized.

Each pulse is split at a ratio of 80/20. The smaller fraction is directed onto the 'pump path'. The larger fraction is directed onto the 'probe path', where the high harmonics (HH) are generated.
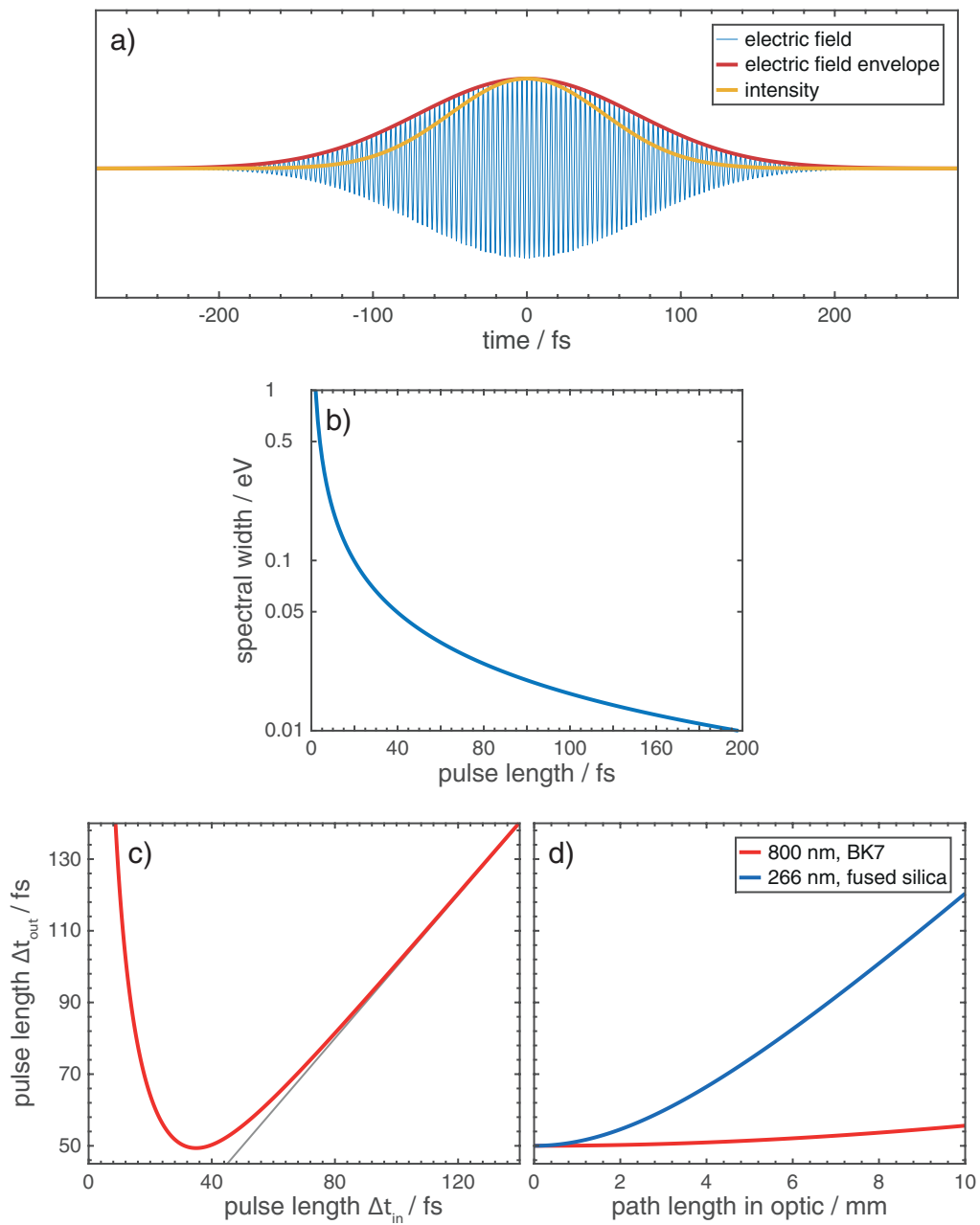
Figure 2.3: a) Depicted is the electric field of a $50\,fs$ laser pulse of only one color ($800\,nm$). b) Shown is the spectral width of a Fourier limited pulse as a function of the pulse duration. c) Dispersion in a $10\,mm$ BK7 glass increases the pulse length. d) The pulse length of an originally $60\,fs$ long laser pulse as a function of the path length in two glasses.

2.3 Second Harmonic and Third Harmonic Generation

At high intensities the optical properties of a material, such as the polarization, respond nonlinearly to the electric field. Only one year after the invention of the laser in 1960, second harmonic generation (SHG) was discovered in visible light [18–20].
The conversion can be experimentally quite simple, via a non-linear crystal, as illustrated in Figure 2.4. In this section, I briefly introduction the theoretical aspects of the harmonic generation and discuss the experimental realization.
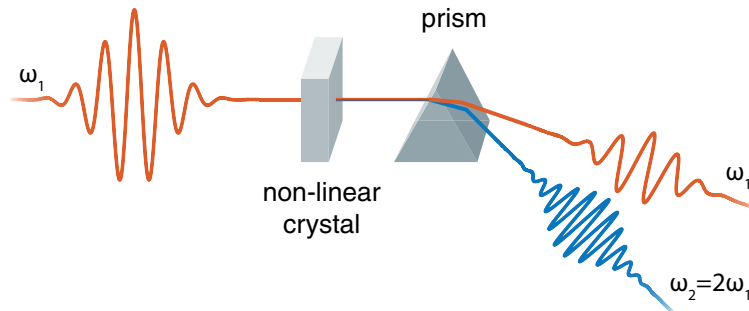
Figure 2.4: An illustration of the second harmonic generation in the non-linear crystal. A prism separates the two outgoing pulses.

The electromagnetic field of the laser causes a polarization $P(t)$ of a dielectric medium

$$P(t) = \epsilon_0 \chi E(t) \tag{2.6}$$

ϵ_0 is the vacuum permittivity, and χ is the susceptibility of the material. If $P(t)$ is expanded in a Taylor series, we can separate the linear term $\chi^{(1)} E(t)$ from the nonlinear terms, as in the following equation:

$$P(t) = \chi^{(1)} E(t) + \chi^{(2)} E^2(t) + \chi^{(3)} E^3(t) + ... \tag{2.7}$$

The second order term can cause efficient SHG in crystals without an inversion symmetry if the phase matching condition is fulfilled

$$\vec{k_1} + \vec{k_2} = \vec{k_3} \tag{2.8}$$

The wave vector of two incoming photons $\vec{k_1}$ and $\vec{k_2}$ must match the wave vector $\vec{k_3}$ of the outgoing photon. For SHG, the two incoming photons are equal $\vec{k_1} = \vec{k_2}$. Hence, the frequency of the outgoing photon ω_2 must be twice as large as the frequency of the two incoming photons ω_1. The process is collinear, which allows us to simplify $\vec{k_1} = k_1$. As a result, the phase matching condition can be written as

$$
\begin{aligned}
2k_1 &= k_3 \\
\Leftrightarrow \frac{2n_1\omega_1}{c} &= \frac{n_2 2\omega_1}{c} \\
\Leftrightarrow n_1 &= n_2
\end{aligned} \tag{2.9}
$$

c is the speed of light, and n the index of refraction of the material. Any material shows dispersion $n = n(\omega)$ and can in principle not fulfill equation 2.9. Bifringe crystals, however, have two optical axes. The light polarized perpendicular to the optical axis of

the crystal is called the ordinary ray and it experiences n_o. The perpendicular polarized light is called the extraordinary ray and experiences n_e. n_e is a function of the cutting angle θ of the crystal, while n_o is independent of θ. The phase matching condition can, hence, be met by cutting the non-linear crystal at a specific angle. There are several types of bifringe crystals which can be used for SHG. The material Beta Barium Borate (BBO), combines a high efficiency and a high damage threshold. Type I phase matching with $800\,nm$ laser light can be achieved in a BBO crystal with a cutting angle of $\theta = 29.2°$. The details of the generation are described in Reference [20].

A longer path within the crystal allows in principle for more conversion, but the optimal length is limited. This is primarily due to the dispersion, but also depends on the pump intensity and the chirp [21]. During the process of SHG, the crystal stretches, chirps, and separates the pulses of the two frequencies ω_1 and ω_2. For type I phase matching, the second harmonic is generated with a polarization orthogonal to the fundamental harmonic. If one desires to combine the two pulses again via sum-frequency generation (SFG), then these effects have to be compensated for. For now, we assume that it is possible and the two pulses can be overlapped in a second BBO to generate the third harmonic. This process is the more general case of SHG. In SFG, $k_1 = k_2$ is no longer a requirement, however, $k_1 + k_2 = k_3$ remains necessary. For generating the third harmonic ω_3, we mix ω_1 and ω_2

$$\omega_3 = \omega_2 + \omega_1 \tag{2.10}$$

The phase matching in a BBO crystal can, in this case, be partially be achieved with a cutting angle of $\theta = 44.3°$. Full phase matching can not be achieved since there are three colors involved. We require the first and the third harmonic in our experiment. Let us now switch from the theoretical aspects of the second and third harmonic generation to experimental aspects.

The setup is illustrated in Figure 2.5. A periscope transports the $20\,\%$ fraction of the fundamental laser beam into the pump-path on a second optical table. During this operation the polarization is turned by $90°$. A variable filter wheel can reduce the intensity by up to one order of magnitude. The light passes several additional mirrors. The leak light of one mirror is focused on a photodiode to trigger an oscilloscope. This trigger can be used to find the temporal overlap between the pump and the probe as we will see later (section 2.6).

The pump beam is then directed onto a motorized delay-stage (OWIS LIMES 120). The stage controls the arrival time of the pump pulse relative to the probe pulse with a precision of $2\,\mu m$, or $13\,fs$. A Galilean type telescope ($f_1 = 175\,mm$, $f_2 = -100\,mm$) reduces the beam size and the divergence [22].

The second and third harmonic are generated with a slightly modified commercial system called femtokit (EKSMA OPTICS FKE-800-050-M). The kit includes two BBO crystals (SHG-BBO and THG-BBO), a waveplate (WP), and a compensation plate (CP), see Figure 2.5. We typically use a pulse energy of $P_{800nm} = 360\,\mu J$. While the $800\,nm$ pulses travel through the first BBO crystal ($200\,\mu m$ thickness), the second harmonic is generated. The polarization is rotated by $90°$ with respect to the fundamental. A waveplate (WP) turns the polarization of the fundamental pulse to match the $400\,nm$ pulse. A calcite plate (CP) or a BBO can compensate the delay between the fundamental and the second harmonic because the materials are birefringent i.e., the refractive index is different for the ordinary and the extraordinary
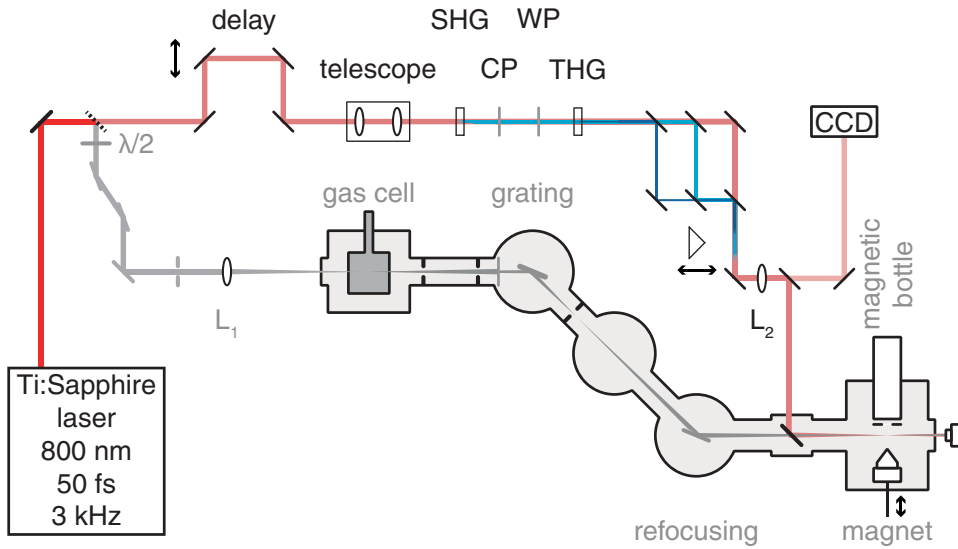
Figure 2.5: Depicted is a schematic layout of the pump path for the generation of the second and third harmonic

wave, the two photon energies are delayed with respect to each other. A second $50\,\mu m$ type I BBO mixes the two pulses via SFG and generates the third harmonic.

The spectrum of the three harmonics (first, second, and third) is shown in Figure 2.6. They have a center wavelength of $787\,nm$, $394\,nm$, and $263\,nm$, respectively, and a width (FWHM) of $27.4\,nm$, $5.3\,nm$, and $2.4\,nm$, respectively, see Table 2.1). The center wavelength can vary on a day-to-day basis by a few nm. In the following, I will refer to the first, second, and third harmonic with their approximate wavelength of $800\,nm$, $400\,nm$, and $266\,nm$, respectively. The pulse power is measured behind the set of mirrors which separate the harmonics.
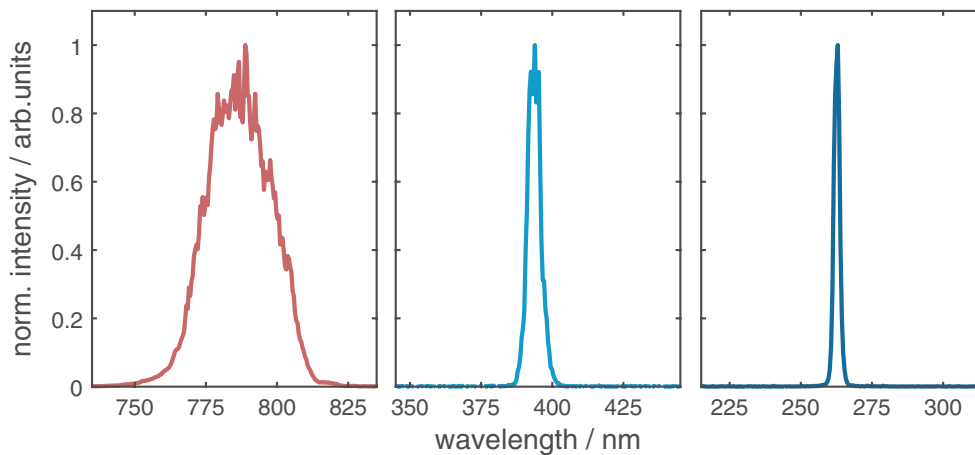
Figure 2.6: Shown are the spectra of the pump pulses: first, second, and third harmonic.

The conversion efficiency of the SHG and the THG depends on various parameters, such as the pulse power, pulse duration, beam size, beam divergence, and crystal thickness. Many of these parameters differ in setups of different groups, which limits the comparability of the performance. The manufacture reaches a conversion rate of $\eta_{SHG} = 50\,\%$ and $\eta_{THG} = 8\,\%$ for the generation. These rates where reached using

harmonic	E_{photon}/eV	$\Delta E_{photon}/eV$	λ/nm	$\Delta\lambda/nm$	$E_{pulse}/\mu J$
H01	1.58	0.055	787	27.4	360
H02	3.15	0.042	394	5.3	
H03	4.71	0.043	263	2.4	6

Table 2.1: Listed are the properties of the harmonics on the pump path.

longer pulses, thicker crystals, and pulse power densities above the damage threshold of the crystals. Zhang et al. reached $\eta_{SHG} = 38\,\%$ with a $500\,\mu m$ BBO and an intensity of $40\,GW/(cm)^2$ [21].

With the $200\,\mu m$ SHG-BBO and a pulse energy of $350\,\mu J$, we reach $\eta_{SHG} = 25\,\%$ and $\eta_{THG} = 2\,\%$. For the experiments, we limit the conversion rate of the third harmonic to $\eta_{THG} = 1.4\,\%$.

The SHG conversion efficiency as function of the fundamental pulse energy reaches a plateau at half the pulse energy typically used in the experiment, see Figure 2.7. The dependence is similar to the one found by Zhang et al. and indicates that the conversion is not limited by the pulse energy [21]. An increased beam size did not improve the conversion efficiency. It is assumed that a deviation from a Gaussian shaped beam profile is the limiting factor.
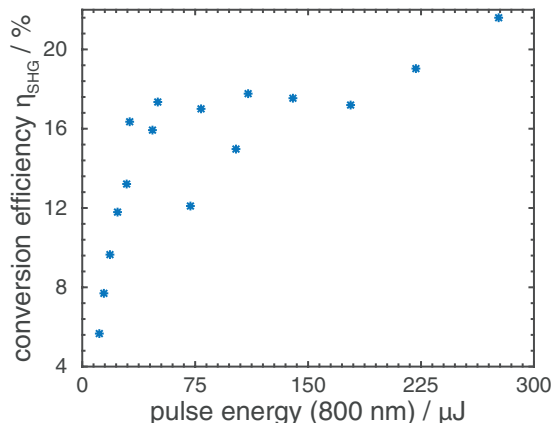
**Figure 2.7:** Shown is the conversion efficiency for the generation of the second harmonic in the setup

All three harmonics exit the THG-BBO colinearly. A set of mirrors allows the separation of the harmonics. For intensity measurements of the individual photon energies, a prism is placed in the optical path. Otherwise, the beam is directed through a focusing lens ($f = 1000\,mm$ for $800\,nm$) via an in-coupling mirror towards the interaction zone in the vacuum. The leak light from the in-coupling mirror is guided onto a CCD ('BladeCam-XHR' from Dataray) for monitoring the beam position and the beam size in the virtual focus.

About $30\,\%$ of the third harmonic is transmitted to the interaction zone. Losses are due to optics, such as the mirrors, the lens, the vacuum window (without anti-reflection coating), as well as the absorption by air. For the experiments with the metal carbonyls, the pulse energy was further reduced to prevent damage to the BBOs and nonlinear effects in the sample with a typical pulse energy of $0.5\,\mu J$ (third harmonic).

2.4 High Harmonic Generation

High harmonic generation (HHG) is a non-linear effect in the field of optics. A mono-chromatic light pulse, with a fundamental photon energy $E_{H01} = h\nu$, can be converted into a polychromatic pulse with discrete photon energies $E_{HHG} = (2n + 1) \cdot E_{H01}$. The polychromatic pulse is then composed of the HH of the fundamental. High intensities are required to cause this phenomenon. The light must be coherent and linear polarized. HH have been generated in gases and solids [23, 24]. HHG is an important light source for spectroscopy in the XUV energy range.

In 1967, a few years after the invention of the laser, New et al. were the first to observe the third harmonic in a gas [25]. The race for the highest harmonic, the highest flux, and the shortest pulse had begun. However, it took until 1987 to access the 17th harmonics [26]. With an increasing photon energy stronger bound core states could be studied. In 1993 the 135th harmonic was reached and today even the 1000th harmonic can be generated [27, 28]. An example for such generation is illustrated in Figure 2.8
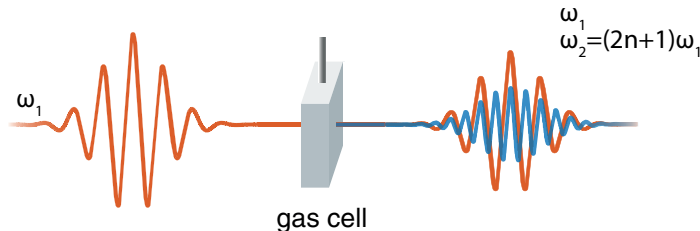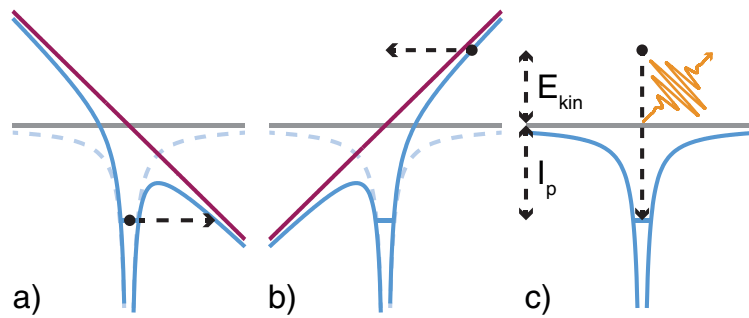

Figure 2.8: An illustration of the high harmonic generation in a gas cell.

The field of the laser light polarizes the atoms in the gas, similarly to the generation of the second harmonic (compare section 2.9). The higher order terms in the Taylor expansion cause the generation of the HH. To achieve a significant contribution from these terms, strong fields are required. With laser intensities $I = (10^{13} - 10^{16})\ W/(cm)^2$, the field strength can become comparable to that of the Coulomb field of the atom. The atomic potential can be distorted to the extent in which the bound electrons can tunnel from the atomic potential well to the free field, see Figure 2.9 a). Before the electron can get too far from the mother ion, the phase of the laser field changes and the electron is accelerated towards its origin, see step b). Upon recollision with the ion, the electron emits one high energy photon. The energy of this photon can be as high as the sum of electrons kinetic energy, E_{kin}, and the ionization energy, I_p, of the atom, see step c). These three steps are part of the 'three-step model' by Corkum [29].

The intensity distribution of the emitted light reflects the dynamics driven by the laser field. The described ionization takes place twice during each laser cycle with the period T and many times within one *fs*-laser pulse. We can approximate each elongation of the field during a half-cycle with a Gaussian pulse shape. The field $E(t)$ can be approximated as a train of these Gaussians. The Fourier transformation allows to change the perspective from the time domain $E(t)$ into the frequency domain $E(\omega)$. The shape of each Gaussian is conserved by the transformation. However, the factor 1/2 is transformed to 2. This results in a separation of the pulses in the frequency domain by $2\,n\omega$ with $n = 1, 2, 3, ...$ The actual energy of the HH is $E_{HHG} = (2n+1)h\nu$. In contrast to to the approximation, the intensity is distributed over a limited energy

Figure 2.9: The 'three-step model' of the high harmonic generation is illustrated [29], see text for details.

range. The lower limit is given by the fundamental photon energy, the upper limit is given by the 'cut off law'.

$$E_{cutoff} = 3.17 \cdot U_p + I_p \tag{2.11}$$

U_p refers to the ponderomotive energy of the laser field and I_p to the ionization potential of the given conversion medium.

$$U_P = \frac{e^2 I \lambda^2}{8\pi^2 \epsilon_0 c^3 m_e} \tag{2.12}$$

I is the laser intensity, e is the charge and m_e the mass of an electron, c is the speed of light, and ϵ the vacuum permittivity. E_{cutoff} depends, hence, on the wavelength of the fundamental laser, its intensity, and the choice of conversion gas.

Depending on the ratio of U_P and I_P, different dynamics occur. The Keldysh parameter γ defines the transition between the regimes [30].

$$\gamma = \sqrt{\frac{I_P}{2U_P}} \tag{2.13}$$

In our experiment, two cases are of importance. For $\gamma > 1$ multi-photon ionization is the most likely ionization process to occur. n photons of the energy $h\nu < I_P$ are absorbed by one atom of the gas. The atom is ionized, and the free electron carries a kinetic energy E_{kin} of

$$E_{kin} = nh\nu - I_P \tag{2.14}$$

In the second case of $\gamma \ll 1$, tunnel ionization is the dominating process. It was described above as the first step of the three-step model. The details of the process are well described in Reference [31].

Similar to SFG, the efficiency of the generation increases if the phase velocity of the fundamental and the HH match. How can this 'phase matching' be achieved in a dispersive medium like a noble gas? The wave vector is given by

$$k \approx \frac{2\pi}{\lambda} + \frac{2\pi N_a n(\lambda)}{\lambda} - N_e r_e \lambda \tag{2.15}$$

Where N_a is the density of the neutral atoms of the generation gas, n the refractive index, N_e the density of the free electrons, and r_e the electron radius [32]. The first term describes the contribution of the vacuum, the second term that of a neutral gas,

and the third term the plasma dispersion. The plasma dispersion can compensate the other two terms. The phase matching condition for the qth harmonic

$$\Delta_q = qk_{laser} - k_{HHG} = 0 \tag{2.16}$$

can be met by adjusting the pressure and the ratio of the neutral gas to the plasma. A longer path L increases the conversion. However, the absorption by the plasma also increases for a larger L [32–34].

For this experiment, an existing setup was moved to a new laboratory and received a dedicated laser system [35, 36]. I will now discuss the alterations and improvements. The new setup is illustrated in Figure 2.10
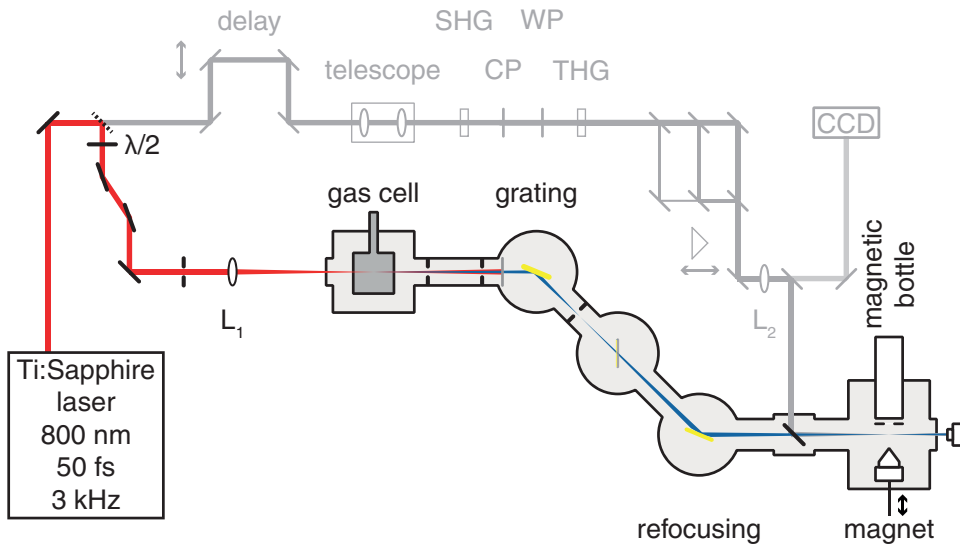
Figure 2.10: Sketched is the probe path of the experiment. The laser beam is focused to generate high harmonics in a gas cell. The high harmonics travel through a vacuum environment and pass a concave focusing grating and a focusing mirror before they reach the experimental zone.

The laser beam in beginning of the 'probe section' has a width of $d_{FWHM} = 7.7 \pm 0.1\,mm$. I have implemented a new intensity control. A waveplate ($\lambda/2$-plate) and two polarizing mirrors adjust the power $P_{800\,nm}$ of the fundamental beam. The waveplate rotates the linear polarized light to a desired orientation. The mirror reflects only the s-polarized part of the pulse, while the p-polarized part of the light is transmitted and removed. The rotation of the waveplate controls the intensity without effecting the polarization. A diaphragm cuts the outer parts of the laser beam profile, thereby enhancing the HH intensity by up to one order of magnitude with respect to the uncut beam. The non-attenuated pulses have a pulse energy of $P_{800nm} = 700\,\mu J$. A lens ($f = 400\,mm$) focuses the beam down to $26\,\mu m$ (FWHM) or $32\,\mu m$ ($1/e$)), which corresponds to an area of $A_{FWHM} = 41 \cdot 10^{-12}\,m^2$ or $A_{1/e} = 50 \cdot 10^{-12}\,m^2$. The intensity in the focus is $I = 233 \cdot 10^{18}\,\frac{W}{m^2}$ or $I = 285 \cdot 10^{18}\,\frac{W}{m^2}$. With this intensity, we can approximate the ponderomotive potential $U_P = 36.3\,eV$ according to formula 2.4.

The described intensity is reached in the focal plane of the laser. The gas jet has to be located close to this focus and should have a vacuum surrounding, as the mean free

path for photons with an energy $E_{photon} = 20\,eV$ in standard atmosphere is only $20\,\mu m$. Various schemes have been invented to combine a gas volume for the generation with a well transmitting vacuum surrounding. We use a gas cell filled with Ar or Xe. The cell is $5\,mm$ long and located $3\,mm$ in front (upstream) of the focus in the vacuum section of our setup. The center volume is enclosed by $100\,\mu m$-thick copper foil on either side. The laser itself burns a hole through both foils with a size of $40 \pm 20\,\mu m$. The pressure of the generation gas is controlled by a fine valve. The HH are typically generated with Ar at a pressure of $8\,mbar$ or with Xe at a pressure of $1\,mbar$.

The ionization energies are $I_P(Ar) = 15.76\,eV$ and $I_P(Xe) = 12.13\,eV$ [37–40]. These values suggest a cut off

$$E_{cutoff} = 3.17 \cdot U_p + I_p \tag{2.17}$$

at $131\,eV$ and $127\,eV$. These values are clearly too high. Most likely due to an overestimation of the ponderomotive potential.

For the experiment it is necessary to block the fundamental light and choose but one harmonic. A $150\,nm$ thick Al filter absorbs $800\,nm$ light and transmits above $17\,eV$. We use a commercial monochromator (LHT 30 from Jobin-Yvon) to select a specific harmonic. The grating was changed from a $500\,l/mm$ grating to a $200\,l/mm$ grating with the intention to reduce the temporal broadening at the cost of energy resolution. The toroidal grating is operated at a constant deviation angle of $142°$. Slits of the size $100\,\mu m$, $250\,\mu m$, and $500\,\mu m$ can be placed in both foci at a distance of $320\,mm$ to the grating. The slit behind the monochromator is called exit slit. Here, the slit reduces the bandwidth at the cost of flux. A calibrated GaAsP photodiode (Hamamastu G1127-04) can be moved in the optical path behind slit to measure the intensity of the HH [41]. I have determined the conversion to translate the monochromator position to energy by fitting all first order harmonics, see Table 2.2.

harmonic	λ/nm	E/eV	monochromator position
H11	73	17.05	283
H13	62	20.15	244
H15	53	23.25	216
H17	47	26.35	194
H19	42	29.45	176
H21	38	32.55	163
H23	35	35.65	151
H25	32	38.75	141
H27	30	41.85	-

Table 2.2: Calibration of the new monochromator grating ($200\,l/mm$)

As discussed above the cut off, the intensity, and the width are three important parameters which depend on the generation gas. Figure 2.11 shows the HH as a function of energy generated with a) argon and b) xenon. Discrete intensity maxima are visible in the spectra of both gases. The maxima are separated by $3.1\,eV$. Photon energies of $42\,eV$ can be reached with argon, $37\,eV$ with xenon respectively. The highest intensities can be reached with xenon up to a photon energy of $32\,eV$. Above $32\,eV$ the generation is more efficient with argon. For both gases spectra were recorded with a $500\,\mu m$ exit slit and a $250\,\mu m$ exit slit. The intensity is in all cases slightly greater for the wider slit, while the tighter slit allows for the improvement of the energy

resolution. If the harmonics are generated with xenon and a $500\,\mu m$ exit slit a stable and reproducible flux of $10^{10}\,photons/s$ can be achieved behind the monochromator. If not otherwise stated all experiments presented in this thesis are carried out with the H15 at $23\,eV$ and an exit slit size of $500\,\mu m$ generated with xenon.
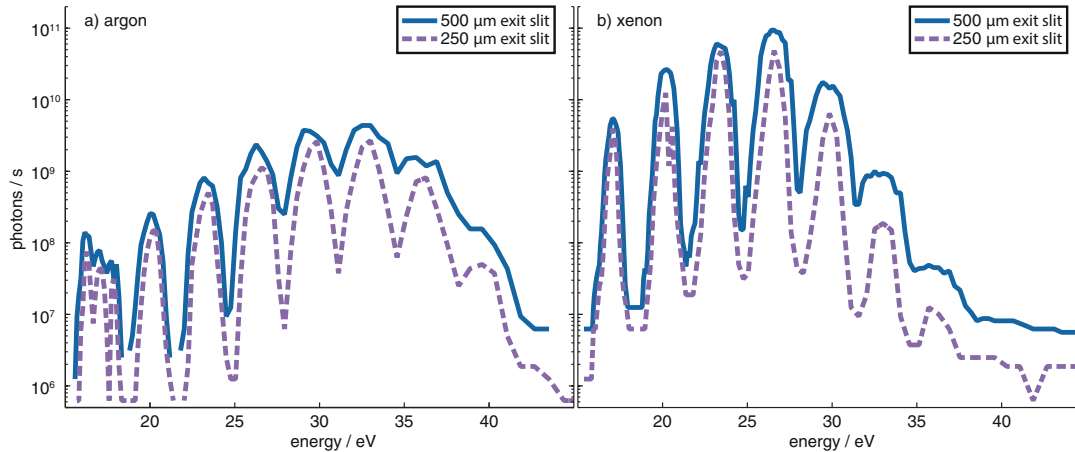
Figure 2.11: Depicted is the logarithmic intensity of the high harmonics generated with a) argon and b) xenon as function of the photon energy

A gold coated diagnostic mirror was temporarily placed in the optical path to reflect the HH onto a X-ray CCD. The mirror is located between the grating and the refocusing section of the probe path, see Figure 2.10. The CCD is located at a distance of $(48 \pm 2)\,cm$ to the exit slit. The CCD records the beam profile of the HH. The projection on the CCD is 1.3 times the size of the beam on the grating. The size of the beam profile allows the estimation of the beam divergence which will be discussed later.

If the diagnostic mirror is removed from the optical path then light continues towards the refocusing mirror. This mirror controls the shape and position of the focus in the interaction zone. The position of the gold coated toroidal mirror can be adjusted with five micrometer screws. A second X-ray CCD, was placed in the interaction zone for the alignment and to characterize the beam profile.

2.5 The Detection System

Both optical paths overlap in the interaction region within the experimental chamber. I have increased the beam height of the to paths to $1417\,mm$. This is considerably higher than in the older version of the setup and allows to attach various diagnostic systems or experimental chambers, which are designed for the height of the beam lines at the Berliner Elektronenspeicherring für Synchrotronstrahlung (BESSY II).
The experimental chamber consists of three main parts: a z-manipulator with diagnostic tools, the gas inlet, and the magnetic bottle [36]. The manipulator includes a Ce:YAG crystal for the optical alignment of the pump and the probe beam as well as coaxial cable to determine the temporal overlap, see below. A camera with a macro-zoom-lens observes the back of the Ce:YAG crystal and facilitates the spatial alignment of the two beams.
The gas inlet consists of a steel pipe and a valve system which allows to transport a gas sample from outside the vacuum system to the interaction zone and to control the flow. The pipe can be connected to lecture bottles or to a $16\,mm$ wide, $25\,mm$ high steel cylinder for the evaporation or sublimation of a sample. in order to avoid contamination, a cut reagent-tube (glass) is placed in the steel cylinder as sample holder. The pressure of both sources can be regulated with a fine valve. Typically the experiments are run at a pressure of $10^{-6}\,mbar$ to $10^{-5}\,mbar$ while $3 \cdot 10^{-8}\,mbar$ is the typical background pressure in the experimental chamber.

To study the electronic structure of the target gas, the molecules are ionized with the XUV photons. The laser beam is marked with a red dot in Figure 2.12. During this process, electrons are emitted in all directions. A permanent magnet with $0.5\,T$ pushes them into the magnetic bottle. A mesh with a retardation potential filters slow background electrons. A grounded mesh at the entrance of the drift tube ensures that the electron flight path is not disturbed by external electrical fields. The solenoid around the drift tube is driven by a current of $600\,mA$. A micro-channel plate (MCP) enhances the signal by producing an electron cascade for each detected electron. A phosphor screen turns this electronic signal into an optical one, which then again gets detected with a photomultiplier tube (PMT). The PMT signal is filtered by a constant fraction discriminator. The signal below a threshold is dismissed, the passing signal is turned into standardized pulses which are digitized by a commercial multiple event time digitizer (FAST ComTec 'P7886'). Electrons from the sample with flight times between $1\,ns$ to $4096\,ns$ are detected.
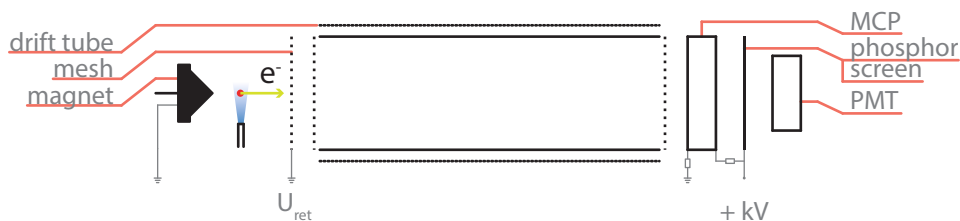
Figure 2.12: The layout for the magnetic bottle is sketched. The laser (red) ejects electrons from the molecular gas jet (blue). The magnet, the drift tube, and electric potentials guide the electrons onto a micro-channel plate (MCP). The electron cascade from the MCP causes luminescence on the phosphor screen which is detected by a photomultiplier tube (PMT).

2.6 Characterization of the Setup

Spatial Structure of the two Beams

Along the optical path there are four locations where the size of the beam profile is of great importance for the performance of the experiment. The first location is within the HHG cell. Here, the poderomotive potential U_p is proportional to the intensity I, which again is anti-proportional to the beam radius w^2. This affects the HH conversion efficiency and the cut off. The second location is on the monochromator grating. The temporal broadening Δt of the HH pulses is proportional to the amount of illuminated lines N. The third location is in the femtokit, where the second and third harmonic are generated (see section 2.3). Here, the conversion efficiencies η_{SHG} and η_{THG} are strongly influenced by the pumping intensity $I \sim \frac{1}{w^2}$. In the interaction zone, the spatial resolution is defined by the size of the probe beam. The size of the pump beam should at this point be slightly larger than the size of the probe beam to allow for beam drifts and pointing instabilities.

The beam profile were recorded between the monochromator and the refocusing mirror with an X-ray CCD. The divergence Θ and the horizontal beam size on the grating $D_{grating}$ of the monochromator are estimated from the beam size D_{CCD} on the X-ray CCD and the distance $l = 48\,cm - 32\,cm = 16\,cm$ using

$$\Theta = 2arctan\left(\frac{D_{CCD} - D_{grating}}{2\,l}\right) \tag{2.18}$$

The FWHM and the divergence for the harmonics H11-H21 are summarized in Table 2.3. This information will be used in the discussion of the temporal resolution, see section 2.6.

	FWHM/ μm	divergence/ $mrad$
H11	720	2.2
H13	827	2.6
H15	853	2.7
H17	407	1.3
H19	587	1.8
H21	1027	2.2

Table 2.3: Horizontal size (FWHM) of the harmonics

The beam profiles of the HH were also recorded in the interaction zone. An X-ray CCD was placed on a rail along the optical axis. This allowed to adjust the five degrees of freedom of the refocusing mirror and optimize the beam focus. The size (FWHM) of the H15 beam in the focus is $105\,\mu m$ (horizontal) by $35\,\mu m$ (vertical), see Figure 2.13. This is $45\,\%$ of the beam area compared to the prior version of the setup [36].

A UV CCD recorded the pump beam profiles. The last mirror outside of the vacuum was used as a beam splitter. The leak radiation is directed onto the CCD. The distance between the final focusing lens and the interaction zone is the same as the distance between the final focusing lens and the CCD. The focus of the transmitted laser beam,
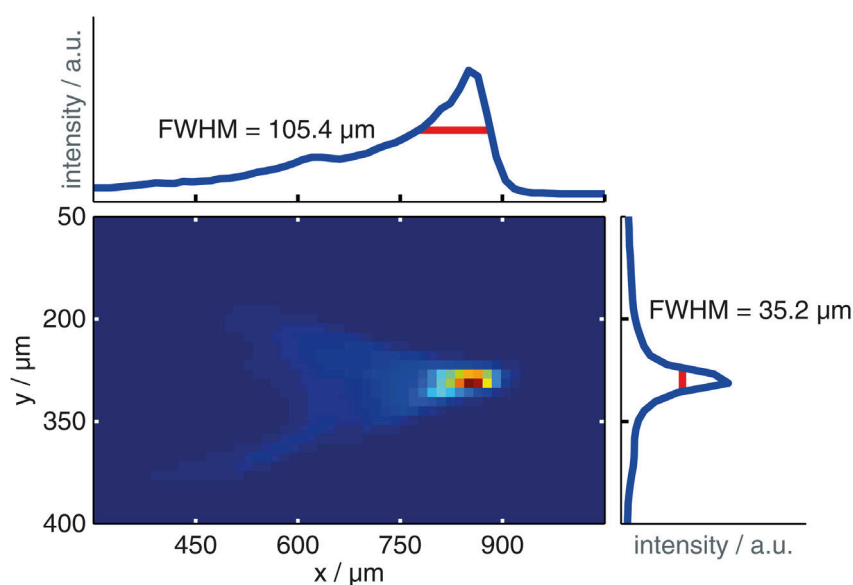
Figure 2.13: Shown is a measurement of the beam profile of the H19 (probe beam) in the interaction zone and the vertical and horizontal projection of the intensity

close to the CCD, is the virtual focus. The CCD monitors the beam size and the beam position during experiments. The position of the lens L_2, see Figure 2.5, can be adjusted to change the beam size in the interaction zone. The observed beam profile has a Gaussian shape. We set the standard size of $105\,\mu m$ by $108\,\mu m$ (FWHM) for the first and third harmonic, see Figure 2.14. The beam size of the third harmonic could be reduced to $50\,\mu m$ by $50\,\mu m$. However, at this size multi-photon ionization were observed in the target gas.

The beam sizes of the first harmonic (pump), second harmonic (pump), and H19 (probe) are summarized in Table 2.4.
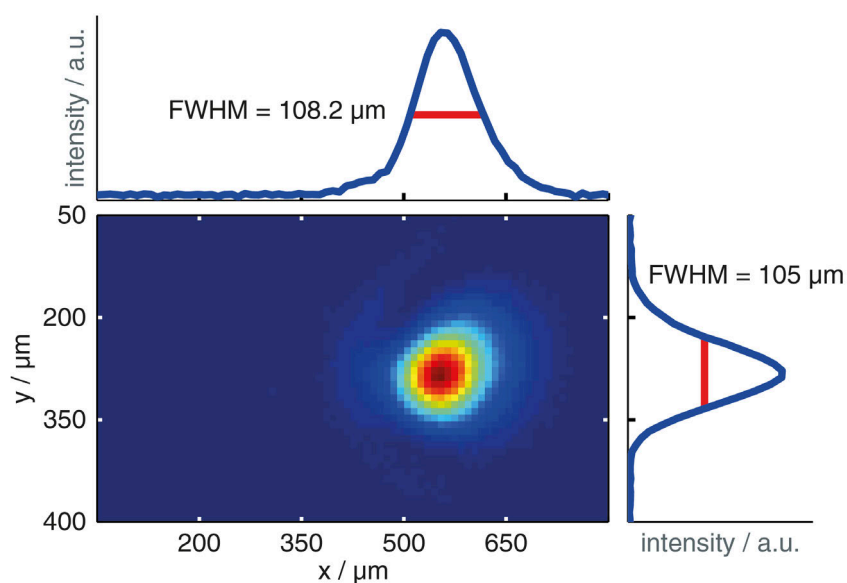
Figure 2.14: Shown is a measurement of the beam profile of the first harmonic (pump beam) in the interaction zone

	horizontal FWHM/ μm	vertical FWHM/ μm
1st	105	108
3rd	100	100
H19	35	105

Table 2.4: Beam size (FWHM) in the interaction zone of pump and probe pulses

Energy Calibration of the Spectrometer

The spectrometer records the intensity, or number of electrons, as function of flight time t. For our understanding it is much easier to think in terms of intensity as a function of the kinetic E_{kin} or the electron binding energy E_{bin}. As first step, the transformation from flight time to kinetic energy was calculated. Without a retardation potential the energy is given by

$$E_{kin} = \frac{1}{2} \frac{m_e \, d^2}{e^- \, t^2} = \frac{1.82 \cdot 10^{-12} eV s^2}{t^2} \tag{2.19}$$

m_e is the mass and e^- the charge of an electron and d the length of the drift tube with $d = 80 \, cm$. the spectrometer was calibrated with the Ar $3p_{1/2}$ and $3p_{3/2}$ lines. The two lines have an energy of $E_{bin} = 15.9 \, eV$ and $E_{bin} = 15.7 \, eV$, respectively, see Figure 2.15. A spectrum recorded in zeroth order shows Ar $3p_{1/2}$ and $3p_{3/2}$ lines from each harmonic, see Figure 2.16. The peak maxima are fit to calculate the kinetic energy as a function of the flight-time
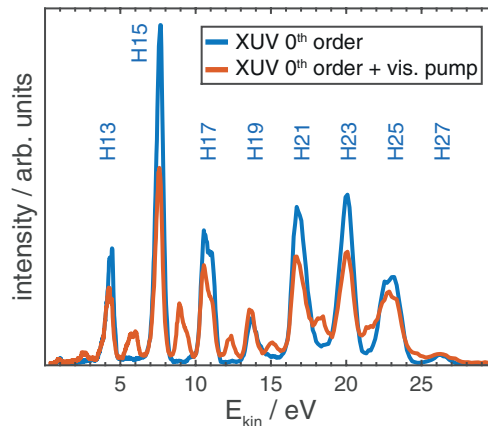
$$E_{kin}(t) = E_0 + \frac{a}{(10^9 t - t_0)^2} \tag{2.20}$$

The fit returns the following values: $E_0 = -0.43 \pm 0.13$, $a = (1.61 \pm 0.08) \times 10^6$, and $t_0 = 60.8 \pm 6.9$. The Gaussian fit components one and two have a width of $\Delta E_{FWHM} = 297 \, meV$.
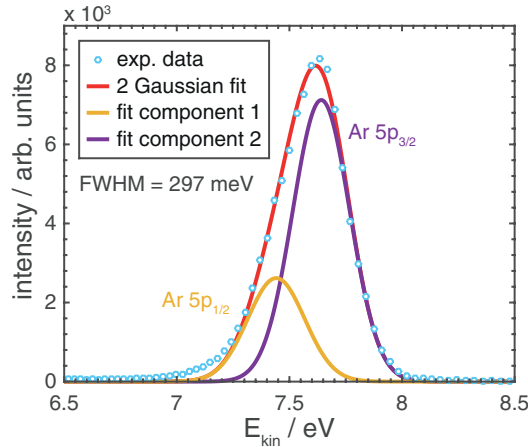
Figure 2.15: In the Spectrum of Ar, two valence states $3p_{1/2}$ at $E_{bin} = 15.9 \, eV$ and $3p_{3/2}$ at $E_{bin} = 15.7 \, eV$ can be observed. This spectrum was recorded in first order, that is with the H15 $(23.25 \, eV)$ only.

Figure 2.16: Shown is the Ar $3p$ line recorded in zeroth order. Each peak corresponds to the ionization of the $3p_{1/2}$ and $3p_{3/2}$ states with one of the n different harmonics (blue line). In between these peaks new peaks appear if the pump and probe pulses are spatially and temporally overlapped. These additional peaks are the sidebands (red line).

Now we can calculate the binding energy

$$E_{bin} = h\nu - E_{kin} + U_{ret} \tag{2.21}$$

We have to keep in mind that the spectra recorded as a function of the flight time t. Each detection window dt has a constant width. However, the transformed window size $dE(t)$ does not remain constant. To keep the integrability, the intensities must be multiplied by the determinant of the transformation

$$I(E) = I(t) \cdot \left| \frac{dE}{dt} \right| \tag{2.22}$$

The determinant $\frac{dE}{dt}$ is proportional to $\frac{1}{t^3}$ [42].

Energy Resolution

The energy resolution of the setup depends on the bandwidth of the HH and the resolution of the magnetic bottle type spectrometer. The exchanged of the monochromator grating could have increased the linewidth of the harmonics.
The fundamental pulse has a bandwidth of $27\,nm$ or $55\,meV$, the third harmonic pulse has a bandwidth of $2.4\,nm$ or $43\,meV$ (see Table 2.1 in section 2.3). These values are small compared to the bandwidth of the XUV pulses and are, hence, neglected in the discussion of the energy resolution of the setup.

As first step, the bandwidth of the harmonics H11-H23 was determined. As second step, the photoelectron lines of Ar and Xe were recorded to determine the bandwidth of the magnetic bottle. The linewidth measured with the magnetic bottle is up to a factor 2 smaller than the bandwidth of the harmonics.
The bandwidth of the harmonics was determined by fitting the HH spectrum, see Figure 2.11, with a set of Gaussians. The spectrum includes the harmonics H11 to H23 and was recorded using a $250\,\mu m$ or a $500\,\mu m$ exit slit. The peaks show a spectral width ΔE_{XUV} between $380\,meV$ and $2.0\,eV$, see Table 2.5. For all photon energies

	$\Delta E_{XUV}\,/\,eV$ $250\,\mu m$	$\Delta E_{XUV}\,/\,eV$ $500\,\mu m$
H11	0.38	0.61
H13	-	0.84
H15	0.62	1.01
H17	0.65	1.31
H19	0.79	1.64
H21	1.25	2.00
H23	1.96	-

Table 2.5: Bandwidth of the harmonics generated with xenon using an exit slit size of $250\,\mu m$ and $500\,\mu m$

the bandwidth decreases for a smaller exit slit size. The bandwidth increases with increasing photon energy. Different generation conditions can be responsible for the observed increase.

Is this overall instrumental energy resolution further limited by the magnetic bottle? The photoelectron (PE) spectra of Ar have been analyzed with respect to the linewidth, see Figure 2.15. The Ar lines $5p_{3/2}$ and $5p_{1/2}$ can not be resolved directly. The data are best fit with a two Gaussian model. Each Gaussian G(E) is defined as

$$G(E) = a\,exp\left(-\frac{(E-b)^2}{2c^2}\right) \tag{2.23}$$

The distance between the two Gaussians is fixed to $200\,meV$ [43]. The full width at half maximum (FWHM) was calculated by

$$FWHM = 2\sqrt{2ln2}c \tag{2.24}$$

and is $297\,meV$ for each component for the H15 for the data shown in Figure 2.16. I have studied the Xe linewith for the harmonics H17 and H19 for the exit slit sizes $100\,\mu m$, $250\,\mu m$, and $500\,\mu m$, see Table 2.6. The impact of the slit size on the Xe PE linewidth is negligible. The FWHM of the H19 is with $610\,meV$ larger than the $220\,meV$ observed by Wernet et al. [36]. A larger width of the harmonic is expected in the current setup because of the lower spectral resolution of the new grating.

harmonic	slit size $/\mu m$	$\Delta E/meV$
H17	500	0.42
H17	250	0.43
H17	100	0.49
H19	500	0.61
H19	250	0.53
H19	100	0.61

Table 2.6: Spectral width (FWHM) of Xe PES lines

The spectral width of the Xe and the Ar photoelectron lines as recorded with the magnetic bottle are considerably smaller than the spectral width of the harmonics.

This discrepancy could be explained by different HH generation conditions for the different measurements. The photoelectron lines were recorded with a larger XUV divergence compared to the measurements of the harmonics. The bandwidth decreases with increasing divergence, because the resolution R of a monochromator grating depends inversely on the number of illuminated lines N and the diffraction order m

$$R = \frac{\lambda}{\Delta\lambda} = mN \tag{2.25}$$

The characterization via the Ar photoelectron line is the closest to the experimental conditions for the study of the molecular dynamics. It is plausible to assume an energy resolution between $0.3\,eV$ and $0.6\,eV$.

For the earlier version of the setup an energy resolution of $200\,meV$ was determined via the Ar photoelectron lines for the H13 with an $500\,\mu m$ exit slit and a $500\,l/mm$ grating [36].

Temporal Resolution

The temporal resolution is an important characteristic of the setup as it limits the observation capabilities of the fast molecular dynamics. The resolution is limited by the duration of the pump and the probe pulses and is defined as the cross-correlation of the two. I will first discuss the pulse duration of the fundamental beam, the $800\,nm$ pump, the $266\,nm$ pump, and the HH probe and later discuss the cross-correlation with the side-band measurements.

Spectral phase interferometry for direct electric-field reconstruction (SPIDER) and Grating-eliminated no-nonsense observation of ultrafast incident laser light e-fields (GRENOUILLE) are both optical techniques and the names for the corresponding instruments which permit the characterization of ultrashort laser pulses [44–47] In the setup, the SPIDER measures the length of the fundamental laser pulses close to the source. The pulse length is $\Delta t_{source} = (44 \pm 2)\,fs$.

The GRENOUILLE is a portable device which allows the study of the pulse length in various sections of the setup. Though the device could be constructed for $266\,nm$ light, our device can measure only the $800\,nm$ pulses. A measurement of the pulse length of the fundamental beam at the source confirms the SPIDER measurements with $\Delta t = 45\,fs$. A measurement of the probe beam behind the experimental chamber was not possible, due to the beam divergence.

The $800\,nm$ pump beam was measured in two configurations: the typical divergent beam and a collinear beam. The GRENOUILLE is designed to work with a colliniear beam only. However, the optics required to pre-collimate the beam affect the pulse duration. The pulse length was measured for both configurations as a function of the chirp. The chirp is the spread of a pulse with respect to the different frequency components. The chirping of pulse occurs in all dispersive optics. If the components of the pulse arrive at different times the pulse is stretched. A prism sequence allows to compensate the chirp. The femtokit was not included in the optical path during these pulse length measurements. The minimum pulse length of the collinear $800\,nm$ pump beam behind the experimental chamber is $\Delta t_{800nm,pump} = 57\,fs$. The minimum pulse length for the divergent $800\,nm$ beam with the same chirp is $\Delta t_{source} = 56\,fs$.

The divergent beam has a pulse length of $\Delta t_{800nm,pump} = 55\,fs$ if we optimize the

pulse length behind the experimental chamber by pre-chirping the pulse.

If, on the other hand, the pulse length is optimized for the source with no pre-chirp the pulse lengths are $\Delta t_{source} = 45\,fs$ at the source, $\Delta t_{800nm, pump} = 66\,fs$ for the divergent beam behind the experimental chamber, and $\Delta t_{800nm, pump} = 79\,fs$ for the collinear beam behind the experimental chamber.

The sidebands are an effect of multi-photon absorption [48]. If argon is probed with the H17, one intensity maximum can be observed in the PE spectrum. This is shown for Ar in Figure 2.17 b) (blue curve). If, in addition to the XUV pulse, a second pulse $h\nu_{vis}$ is present the emitted electron can carry the kinetic energy

$$E_{kin} = h\nu_{xuv} - E_{bin} \pm nh\nu_{vis} \tag{2.26}$$

The number of sidebands increases with increasing intensity of the visible pulse. The duration of the sideband indicates the cross-correlation of both pulses [49]. The first set of sidebands was measurement directly after measurement of the pulse length with the GRENOUILLE. The sidebands were recorded with the monochromator in zeroth order, see Figure 2.17 a) and c) as well as in first order, see b) and d). In first order, seven sidebands at the higher energy side of the Ar mainline are observed. The first sideband was fit in time with a Gaussian. The shortest cross-correlation $(800\,nm + H15)$ found was $\Delta t_{total} = 111\,fs$. The probe pulse length Δt_{HHG} can be calculated with the information on the pump pulse length Δt_{pump} from the measurements with the GRENOUILLE

$$\Delta t_{total} = \sqrt{\Delta t_{pump}^2 + \Delta t_{HHG}^2} \tag{2.27}$$

The minimal pulse length is achieved with the same chirp setting as used to optimize the pulse length at the source. The XUV pulse length for this chirp is then $\Delta t_{HHG} = 82\,fs$ in first order, see Figure 2.17 f) and $69\,fs$ in zeroth order. The difference of $dt = 13\,fs$ between first zeroth order and first order is due to the pulse stretching by the monochromator grating

$$dt = \frac{mN\lambda}{c} \tag{2.28}$$

Where m is the order of diffraction, N the number of illuminated groves and λ the wavelength, and c the speed of light [50]. Solved for N we find 73 illuminated groves, which corresponds to a horizontal beam size of $366\,\mu m$ on the grating. This size is lower than the $d_{FWHM,x} = 853\,\mu m$ estimated from the beam profiles but on the same order of magnitude.
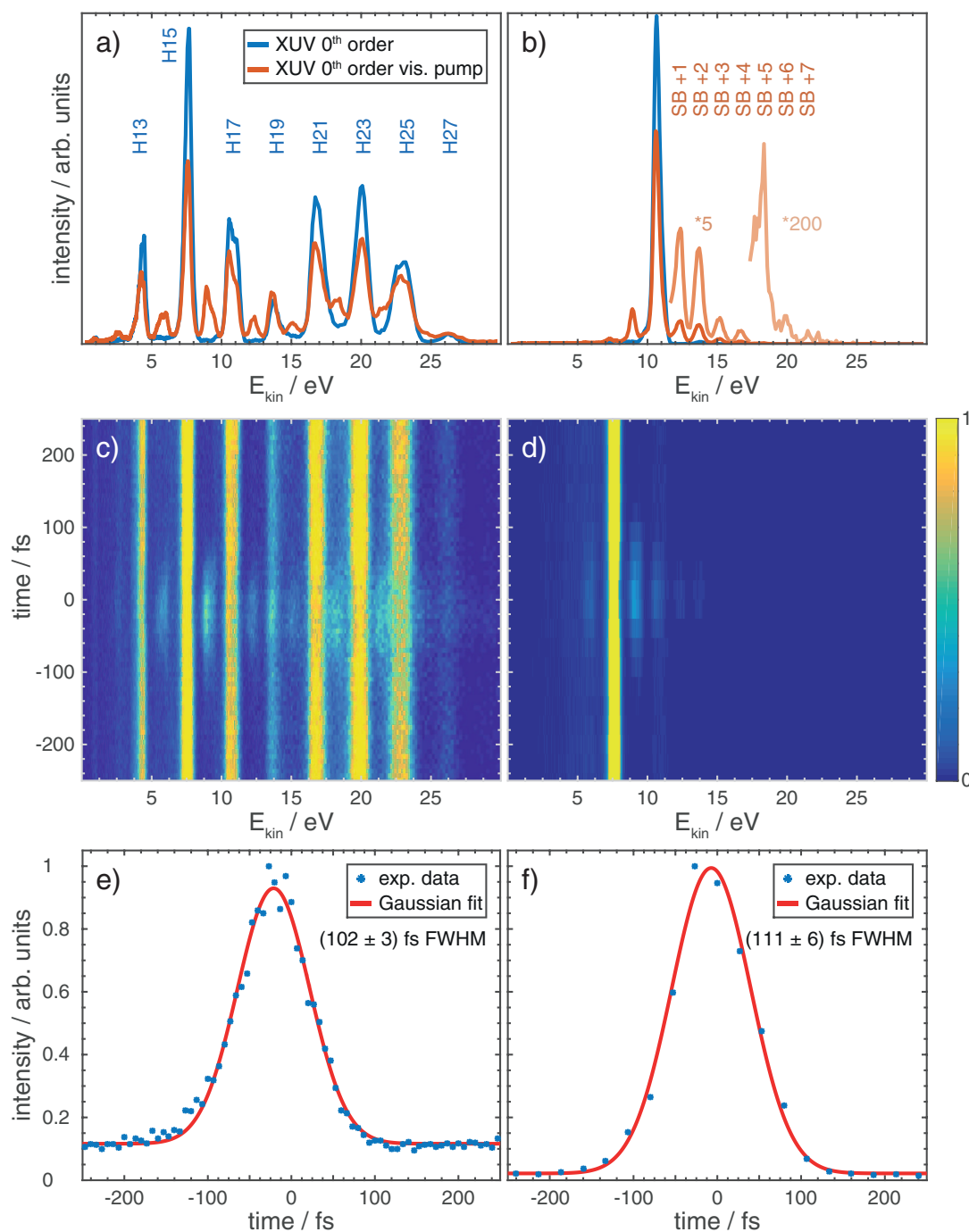
Figure 2.17: Shown are the Ar $3p$ photoelectron spectra pumped with $800\,nm$ and probed with high harmonics in 0th order [a), c), and e)] and in 1st order [b), d), and f)]. The static Ar spectra were taken with no delay between the pump and probe pulse. Each maximum (blue) stems from a different harmonic. Sidebands (SB) can be observed if the visible light pump is also present (red). (a, same as Figure 2.16) The spectra recorded with the non-monochromized 0th order probe light and (b) with the harmonic 17 (H17), monochromized in first order. The signal at higher energies was multiplied by a factor of 5 and 200 for illustration purposes. Ar $3p$ photoelectron spectra as a function of time probed with 0th order XUV light (c) and with 1st order H15 (d). Energy integrated intensity of the +1 SB of the H15 in 0th order (e) and 1st order (f)

The cross-correlation length increases for the higher order harmonics. The values range from $98\,fs$ to $143\,fs$, see Table 2.7. The increase in the pulse length could be due to an increase in the illuminated area on the monochromator grating. A specific harmonic is selected by the angle of the grating. Does the difference in the angle result in a difference of the number of illuminated lines and, hence, the temporal broadening? The difference in the grating angle for light of $10\,nm$ and $100\,nm$ is less than $1°$. For a beam size on the grating of $366\,\mu m$, the rotation of the grating by $1°$ affects the beam size by $1.6\,\%$. The effect on the temporal broadening should be proportional. However, the measured broadening increases by $46\,\%$ from H13 to H23. It is therefore plausible that the difference in pulse length between the harmonics is caused by another effect. Possibly the generation conditions for the different harmonics differ to the extent that the increase of the illuminated area can be explained by an increase in the divergence [51].

harmonic	$\Delta t/fs$
H13	98 ± 4
H15	109 ± 4
H17	114 ± 3
H19	131 ± 3
H21	123 ± 4
H23	143 ± 9

Table 2.7: Pulse duration Δt of the high harmonics was calculated from the cross-correlation signal.

So far, we have concentrated on the $800\,nm$ pump. How does the cross-correlation change when the optics of the femtokit are included, in particular with a $266\,nm$ pump wavelength? Unfortunately, the THG intensity in our experiment is not high enough to allow for the analysis of the cross-correlation as a function of multiple parameters. However, the Ar sideband could be recorded in a six hour long measurement using H15 for probing and $266\,nm$ for pumping. The spectrum is shown in Figure 2.18 a). The Ar mainline at $E_{kin} = 4.6\,eV$ was so intense during the data acquisition that the MCP detector became saturated. The mainline is cut off. This is not a problem if one is only interested in the peaks at higher kinetic energy, which are recorded before the detector is saturated. I can identify three additional peaks. Two of them are at $+3.1\,eV$ and $+6.2\,eV$ of the mainline. The peaks represent a contamination of the probe pulse with the light of the H17 and H19. This contamination occurs to a small degree also in the experiments with the metal carbonyls, see below. At $+4.7\,eV$ above the mainline a time dependent signal can be observed. I assign this peak as the sideband of the mainline because the energy difference coincides with the photon energy of the pump pulse. The cross-correlation for the $266\,nm$ and the H15 pulses is shown in 2.18b). The Gaussian fit of the peak has a width of $\Delta t = (262 \pm 26)\,fs$. The $266\,nm$ pulse length is $249\,fs$ if we assume that the XUV pulse width remained the unchanged. This resolution is surprisingly large. The chemical dynamics, which we will discuss later, indicate a temporal resolution on the same order of magnitude. The cross-correlation also allows for a precise determination of the pump probe overlap which will be discussed in the next section.
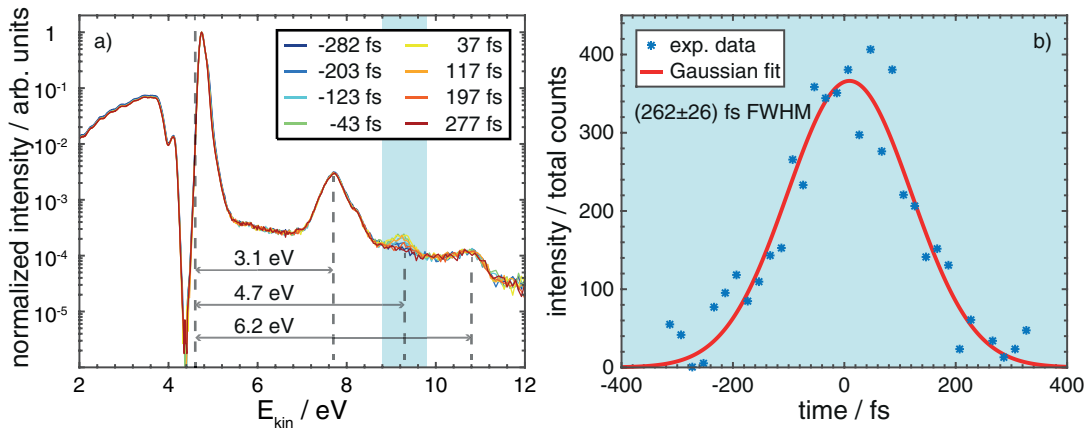
Figure 2.18: a) The spectrum of Ar is shown at different delays with respect to the $266\,nm$ pump. The first sideband is located at about $E_{kin} = 9\,eV$. b) Trace and fit of the energy-integrated sideband.

Establishing the Temporal Overlap Between the Pump and the Probe

How can the arrival time of two pulses be matched on the femtosecond timescale? A difference in the arrival time below $10\,fs$ implies a difference of about $3\,\mu m$ on the path length of over $10\,m$. As a first approximation, the path length is measured with a ruler and the length is matched by adjusting a delay stage. The accuracy of this method is $\pm 5\,cm$ or $\pm 170\,ps$.

A more accurate method is based on the SHG. The $800\,nm$ light of both paths are overlapped on a BBO for SHG behind the experimental chamber. The intensities where sufficient to detect a SHG signal in-spite of the divergence of the light on the probe path. The accuracy of the temporal overlap for the $800\,nm$ - $800\,nm$ correlation is about $50\,fs$. However, the $266\,nm$ beam takes a different path at the separating mirrors behind the femtokit which is why the temporal overlap for the $800\,nm$ - $800\,nm$ light and the $266\,nm$ - $800\,nm$ light is different. The $266\,nm$ intensity did not suffice to establish the temporal overlap via SFG of the two colors, $266\,nm$ - $800\,nm$. An alternative to establish the temporal overlap between the $800\,nm$ and $266\,nm$ pulses had to be found. We desired a method which is sensitive to the energy range from the visible to the XUV and which allows for the determination of the timing with an a accuracy of a few picoseconds.

A clean cut SMA-type cable is emplyed as detector for the pulses in the interaction zone. The use of such a coaxial cable for the synchronization of two pulses has been described by Krupin et al. for higher energies [52]. The technique is base on an Austen-Switch [53]. The cable functions as an antenna. The light pulses are focused on the $1.2\,mm$ thick inner conductor of the SMA cable where they cause a photo-electric effect and induce a potential-difference between the copper core and the copper shield. This difference is measured with an oscilloscope. The $800\,nm$ pulses on both paths in (0th order), the third harmonic on the pump path, as well as the H13-H19 on the probe path could be detected. Pulses of the two paths can be aligned temporally. The precision is limited by the bandwidth of the electrical components. The vacuum-feed-trough has a bandwidth of $2\,GHz$, oscilloscope ('Tektronix DPO72504D') $25\,GHz$, and the two cables of $2\,m$ outside of the vacuum $> 25\,GHz$. The combined bandwidth

is approximated with $\Delta\omega = 25\,GHz$. This would lead to a broadening of a Gaussian shaped femtosecond pulse by

$$\Delta t \geq \frac{2\pi c_B}{\Delta\omega} = 112\,ps \tag{2.29}$$

Indeed, such a broadening can be observed. The temporal difference between two pulses was determined via the inflection point of the rising edge. Figure 2.19 shows exemplary oscilloscope traces (measured potential vs time). Each of the two traces is an average of 1000 pulses. The observed jitter and therefore the accuracy of the synchronization of the pulses is $1.2\,ps$. The limiting factor is not the pulse width but the $3\,ps$ jitter introduced by the photodiode which triggers the oscilloscope. The averaging reduces the jitter to the $1.2\,ps$. This can be further improved by employing a second SMA cable as detector for the trigger pulses.
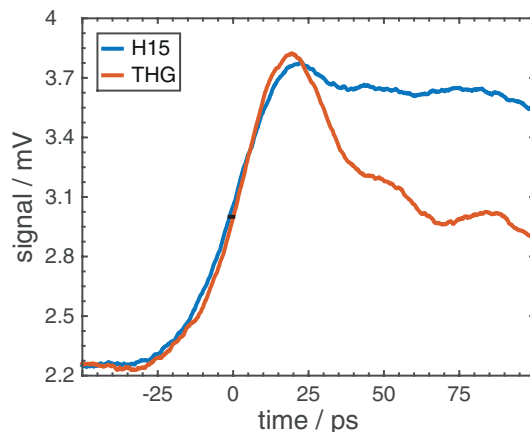
Figure 2.19: The arrival time of the third harmonic (pump) and the H15 (probe) are matched with an accuracy of $1.2\,ps$.

The potential and the fluence dependence were studied for three photon energies. The potential of the SMA cable depends on the photon energy and the pulse energy. Table 2.8 lists the highest detected potentials for three photon energies. The detected potential was reproduced several times with intermediate disablement of the components.

E_{photon}/eV	E_{pulse}	U/mV
1.55	$400\,\mu J$	60
4.65	$380\,nJ$	6
23.25	$22.3\,pJ$	1.6

Table 2.8: The potential U was measured on SMA cable for different photon and pulse energies.

The energy required to remove one electron from a Cu solid is $W_{Cu} = 4.65\,eV$ [54]. Hence, one XUV photon or one $263\,nm$ photon can eject one electron from the Cu core. However, three $787\,nm$ photons are required to eject one electron. We can calculate

the number n of photons from the pulse energy E_{pulse}

$$n = E_{pulse}/E_{ph} \tag{2.30}$$

A pulse with $E_{pulse} = 400\,\mu J$ and $E_{ph} = 1.55\,eV$ consists of $2 \cdot 10^{15}$ photons. A pulse with $E_{pulse} = 400\,nJ$ and $E_{ph} = 4.71\,eV$ consists of $5 \cdot 10^{11}$ photons. A pulse of the H15 with $22.3\,pJ$ consist of $6 \cdot 10^{6}$ photons. Hence, currents of $I(800\,nm) = 300\,\mu A)$, $I(266\,nm) = 15\,mA)$, and $I(H15) = 2\,nA)$ are expected.

The fluence dependence was studied for the three photon energies. The amplitude and the integrated potential both depend linearly on the pulse energy for all three photon energies, see Figure 2.20. The following dependence for the potential maximum U as function of the pulse energy E_{pulse} were determined:

$$
\begin{aligned}
U(800\,nm) &= 171.5\,V/J \cdot E_{pulse} - 9.7\,mV \\
U(266\,nm) &= 14.4\,kV/J \cdot E_{pulse} + 63.5\,\mu V \\
U(H15) &= 165.0\,kV/J \cdot E_{pulse} + 38.5\,\mu V
\end{aligned}
$$

This calibration allows for the determination of the photon flux in the interaction zone in future experiments.
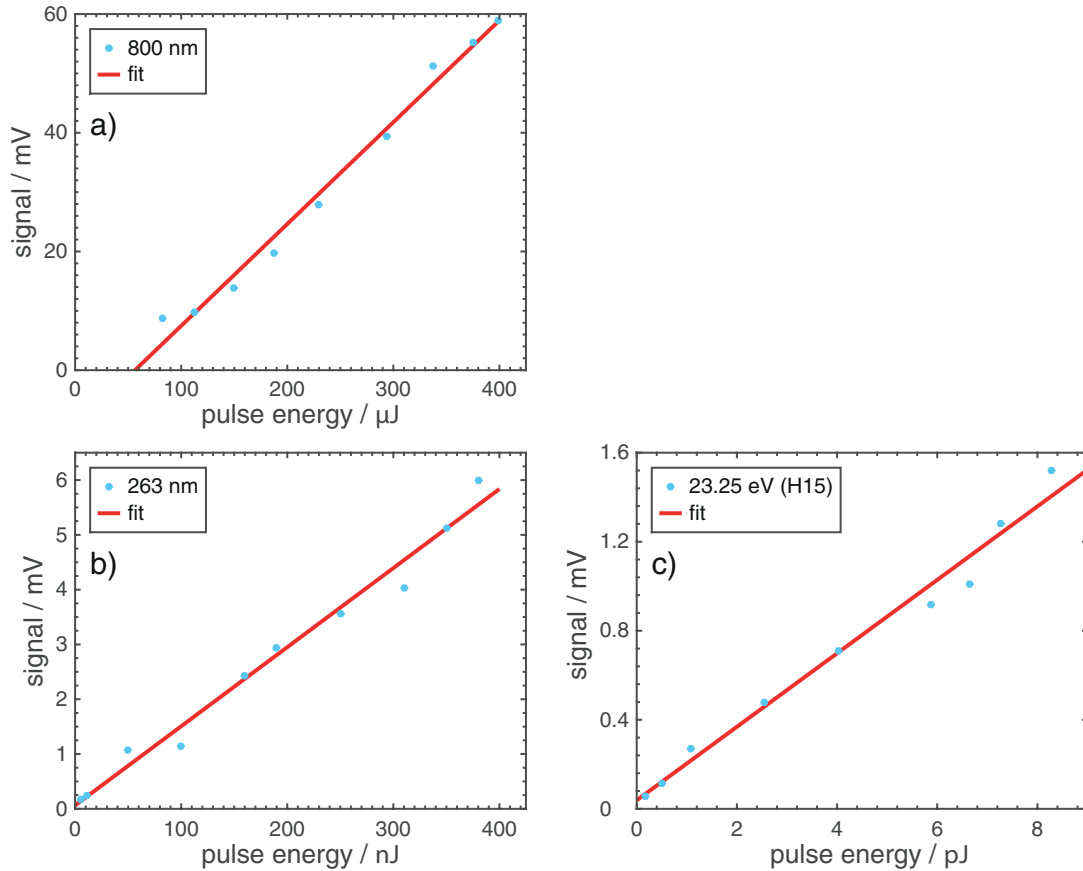
Figure 2.20: Shown is the fluence dependence of the SMA-potential as function of the pulse energy for three different wavelengths. The correlation is in all three cases linear.

t_0 is determined with an accuracy of $100\,fs$ using the ultrafast dynamics of $Fe(CO)_5$. Even more precise is the determination of the temporal overlap with the sidebands. Narrowing down the scan range with the SMA cable and the $Fe(CO)_5$ dynamics makes a sideband scan feasible. To the best of our knowledge, this is the first time that the cross-correlation of a $263\,nm$ pulse and a HH pulse has been measured. The Ar sideband reveals the delay position of the temporal overlap with a precision of $\Delta t = 26\,fs$, see Figure 2.18.

In summary, I have moved an existing HH setup to a new laboratory, characterized, and improved it. The new setup has a dedicated laser system with an average power of $5\,W$ at about $800\,nm$ and a repetition rate of $3\,kHz$. The laser pulses are optically split for jitter-free pump-probe experiments. The second and third harmonic are generated on the pump path for the optical excitation of the samples. The typical THG conversion efficiency is about $\eta_{THG} = 1.4\,\%$ with an pulse energy of $E_{pulse} = 0.5\,\mu J$ at the sample. The sample can be probed with XUV light in the range of $17\,eV < E_{ph} < 42\,eV$ with the odd harmonics of the fundamental laser. A photon flux of $10^{10}\,photons/s$ can be generated reproducibly with Xe for at least one harmonic. The generation conditions can be manipulated to strengthen a specific harmonic. The HH have a horizontal width of $105\,\mu m$ and a vertical width of about $35\,\mu m$ on the sample, while the third harmonic is slightly larger with a width of $100\,\mu m$ in both dimensions. The bandwidth of the harmonic H19 was determined to about $600\,meV$. The pulse length was studied for different photon energies with various methods. We found that the source can deliver pulses of $45\,fs$. The HH have a pulse length between $98\,fs$ and $143\,fs$ at the location of the sample. The overall temporal resolution is given by the cross-correlation which is $262 \pm 26\,fs$ for experiments with the third harmonic and H15. The temporal overlap can easily be established in a two step process. An SMA-type cable detects the pulses of the HH and the third harmonic. The arrival time can be matched with a precision of up to $1.2\,ps$ with a $25\,GHz$ system. The precision can be improved in a second step either via the sideband measurements or the photo induced dynamics in metal carbonyls.

Chapter 3

Molecular Dynamics

In this chapter, I introduce general aspects of the metal carbonyls, such as their stability, the characteristics of the metal-carbonyl bond, as well as the insights from IR, visible light, and X-ray spectroscopy. This discussion leads us into the experiments with $Fe(CO)_5$ and with $Cr(CO)_6$ which are analyzed in the second and third section. The results of the two complexes are compared and the implication for the model of the electronic dynamics are discussed in section three.

3.1 Bonding in Metal Carbonyls

Metal centers play an important role in chemistry and biology. Often one or more metal atoms are found at the active site of a catalyst. The catalyst reduces the activation energy and increases the rate of a specific reaction. The catalytic reaction does not only depend on the metal itself but also on the local environment surrounding the metal. We are only beginning to understand catalysis and only few well performing catalyst have been developed by design.

Carbon monoxide (CO) is an important ligand for metal centers. It is famous as poisonous gas from incomplete combustion. If it binds to the hemoglobin carbon monoxide prevents the transport of oxygen. Less famous is its important role in the human body as neurotransmitter and as regulator for an inflammatory responses [55, 56].

Even simple compounds with only one transition metal and a few carbonyl ligands have the ability to catalyze reactions. They are important for organometallic synthesis, biological processes, and materials chemistry [57] (and references therein).

$Ni(CO)_4$ was the first transition metal carbonyl to be discovered by Mond, Langer, and Quincke in 1890 [58]. Today, it is known that many of the transition metals can form metal carbonyl complexes. Irving Langmuir predicted that transition metal complexes which follow the 18 electron rule are most stable [59]. The metal can reach a full valence shell, or noble gas configuration, by sharing electrons with the ligands or other metal atoms.

A carbonyl ligand provides two valence electrons to the bond. The number of valence electrons provided by the metal coincides with its group in the periodic table. Three examples are the Cr, Fe, and Ni. They have six, eight, and ten valence electron, respectively. In order to complete their valence shell they require six, five, and

four carbonyl ligands, respectively. They form the compounds $Cr(CO)_6$, $Fe(CO)_5$, and $Ni(CO)_4$. $Cr(CO)_6$ has an octahedral symmetry(O_h), $Fe(CO)_5$ has a trigonal bipyramidal symmetry (D_{3h}), and $Ni(CO)_4$ has a tetrahedral symmetry (T_d). These complexes are depicted in Figure 3.1 [60].


Cr(CO)$_6$
O$_h$

Fe(CO)$_5$
D$_{3h}$

Ni(CO)$_4$
T$_d$
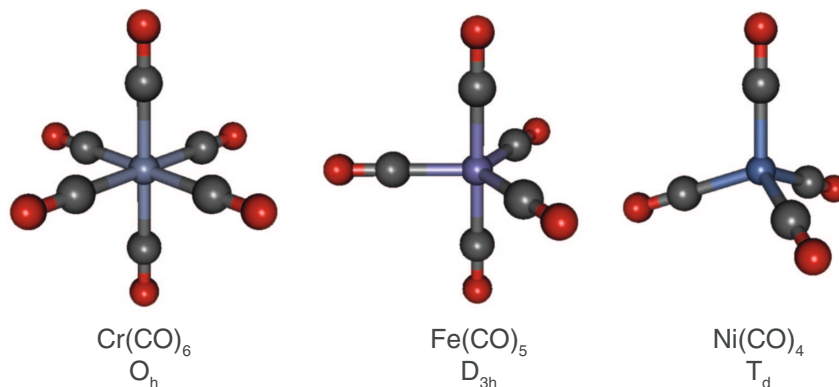
Figure 3.1: Sketched is the structure and symmetry of three metal carbonyls.

Many transition metals with an odd number of valence electrons form multinuclear complexes and take a range of different structures. By forming multinuclear complexes even these complexes can reach a count of 18 valence electrons. One examples is $Mn_2(CO)_{10}$: Here, the 18 electron rule applies to each of the two metals. One manganese provides seven valence electrons, each of the five carbonyls provides two electrons, and one electron is shared via the Mn-Mn bond. This leads to a total of 18 valence electrons.

In multinuclear metal carbonyls, one carbonyl can share a bond with multiple metal atoms. Ligands bound to only metal are called the ligand terminal. Ligands bound to several metals are called the ligand bridging i. e., $di-\mu$ or $tri-\mu$ bridging ligand if the bond is shared with two or three metals, respectively. In $Co_2(CO)_8$, two carbonyls can function as bridging ligands.

Let us now understand how the bond between the carbon and the oxygen and the bond between the metal and the carbonyls are formed. In free CO (gas phase) the two atoms, carbon and oxygen, are linked by a triple bond. The bond is $112.8\,pm$ long. The molecular orbitals are formed as a combination of atomic orbitals. The orbitals on the bond axis are termed σ-orbitals, off axis orbitals are termed π-orbitals. The molecular orbitals of CO are illustrated in Figure 3.2. The orbitals are numbered starting at the lowest energy (1σ and 2σ are not shown). The top orbitals are higher in energy, but the energetic distance of the orbitals is not to scale. The σ orbitals have a character similar to the atomic s orbitals. The electron density is close to the nucleus. The electron density of the π orbitals extends further away from the center, similar to the atomic p orbitals. The orbitals 1σ, 2σ, 3σ, 5σ, and 1π are bonding. Electrons occupying these orbitals strengthen the molecular bond. The orbitals $4\sigma^*$, $2\pi^*$, and $6\sigma^*$ are anti-bonding orbitals, which is indicated by the star. Electrons in anti bonding orbitals weaken the bond.

Let us now consider the bond between a carbonyl and a metal atom. The carbonyl
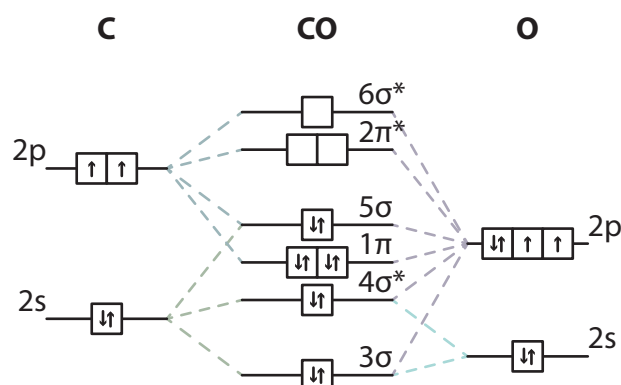
Figure 3.2: This molecular orbital diagram illustrates the electronic configuration of carbon monoxide

5σ orbital donates electron density to the vacancies in the metal d or p orbitals. The metal d orbital can donate into the empty carbonyl $2\pi^*$ orbital. The process is termed σ donation - π backdonation or backbonding and is illustraded in Figure 3.3. It is well described by Atkins et al. [61]. The occupation of the $2\pi^*$ is only anti-bonding with respect to the $C-O$ bond. The backdonation builds a $M-CO$ bond at the cost of the $C-O$ bond strength [62–65]. The backdonation is essential to the $M-CO$ bond. Ti^{4+} has no electrons available for the π backdonation. A stable $Ti^{4+}(CO)_n$ complex has not been found yet [66].

On one hand, the carbonyl can stabilize electron rich metal centers because it is a great π-acceptor. On the other hand, such a metal carbonyl complex can easily be destabilized by excitation. The relatively small dissociation energy offers flexibility during a reaction and is crucial for the catalytic performance.
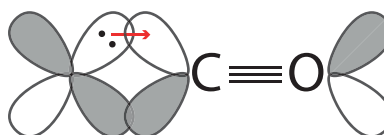

Figure 3.3: Illustration of the backbonding in a metal carbonyl.

This picture gives the impression that only few of the metal and carbonyl orbitals participate in the bonding. However, calculations show that the situation is not quite that simple. The involved orbitals hybridize and form new molecular orbitals. Each atomic orbital can contribute to several molecular orbitals. In $Fe(CO)_5$, the molecular orbitals with $Fe(3d)$ character are numerous, see Figure 3.4. The following discussion focuses on the dynamics of these hybridized orbitals.

Several experimental techniques have contributed significantly to our understanding of the bonding and the dynamics of metal carbonyls, e.g. spectroscopy with photoelectrons, infrared and visible light, and transient ionization. In the following, a summary of the most important findings is presented.

The vibrational frequency ν_{CO} of the $C-O$ bond can be measured with infrared (IR) spectroscopy. The frequency indecates the strength of the ligand bond and the bonding
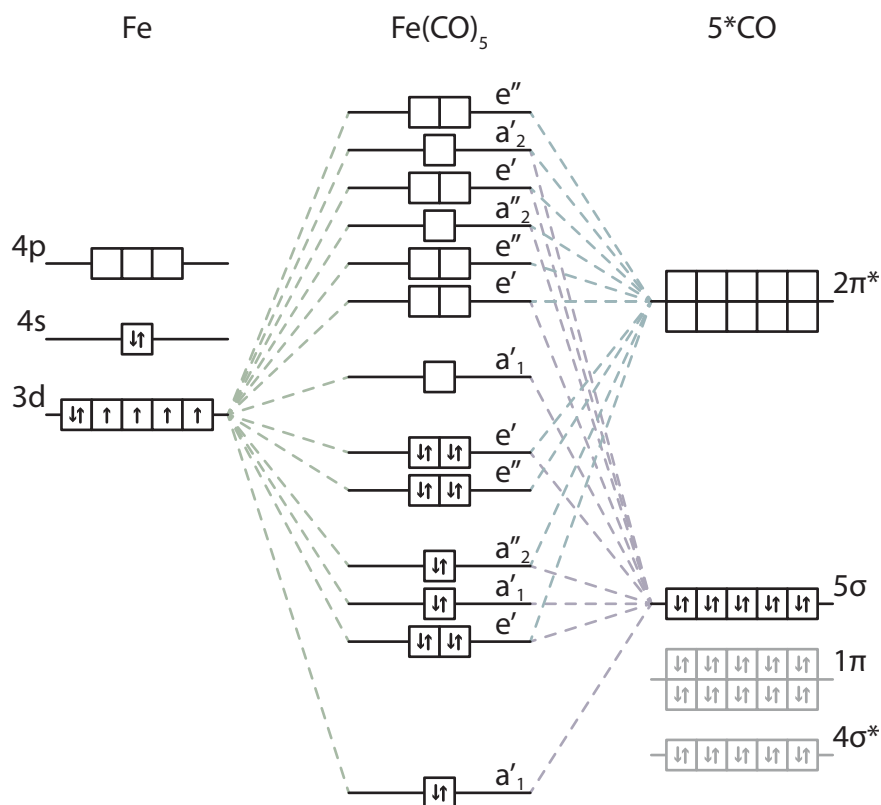
Figure 3.4: Depicted is a simplified diagram of the molecular orbitals participating in the metal-carbonyl bond with iron $3d$ character.

between the metal and the ligand [63]. A high frequency coincides with a strong and short bond. For an unbound carbon monoxide ν_{CO} is $2143\,cm^{-1}$ [67]. In many metal carbonyls ν_{CO} has a lower value, see Table 3.1. This indicates that the bond in the carbonyl is weakened compared to the free CO.

The metal hexacarbonyls $M(CO)_6$ in the sixth group (Cr, Mo, and W) show a similar ν_{CO} [66, 68]. The distance between the metal and the carbon increases for the heavier elements. This makes sense, as orbitals with a greater average distance to the metal core participate in the bonding thus elongating the metal-carbonyl bond.

The distance of the CO bond is about the same in these three hexacarbonyls. This is surprising as the electronegativity increases strongly towards W i. e., 1.66 for Cr, 2.16 for Mo, and 2.36 for W. However, from the perspective of the backdonation these atoms are similar. Atomic Cr and Mo both have five d electrons and five d vacancies available, whereas W has four d electrons and six vacancies.

In the fourth period ν_{CO} increases for transition metals of a higher group. This correlates with a decrease in the CO bond distance.

$V(CO)_6^-$, $Cr(CO)_6$, and $Mn(CO)_6^+$ differ strongly in their ν_{CO} although all three complexes have the same amount of valence electrons and ligands. The amount of charge available for the σ and the π system plays an important role. The spin state and the oxidation state also impact the bond distance [62]. Calculations complement the IR data and target the question whether the σ-bond or the π-bond contributes more. After several decades the discussion is not concluded. Photoelectron spectroscopy is a technique which partially distinguishes between the σ and the π system. The results

from visible spectroscopy will help us to understand the photoelectron spectra.

	ν_{CO}/cm^{-1} [66]	ν_{CO}/cm^{-1} [68]	d_{MC}/pm	d_{CO}/pm
CO	2143	-	-	112.8 [69]
$V(CO)_6$	1976	1989	210.5 [70]	113.8 [70]
$Cr(CO)_6$	2000	2000	191.8 [71]	114.1 [71]
$Mn_2(CO)_{10}$	2013	-	181.1 - 186.5 [72]	112.4-113.4 [72]
$Fe(CO)_5$	2023	2016, 2038	180.7 (ax.) [73]	115.2 [73]
	2023	2016, 2038	182.7 (eq.) [73]	115.2 [73]
$Co_2(CO)_8$	2044	-	180 (t.) - 190 (b.) [74]	-
$Ni(CO)_4$	2057	2061	183.8 [75]	114.1 [75]
$Cr(CO)_6$	2000	2000	191.8 [71]	114.1 [71]
$Mo(CO)_6$	2004	2003	206.3 [76]	114.5 [76]
$W(CO)_6$	1998	2000	205.8 [76]	114.5 [76]
$V(CO)_6^-$	1860	-		
$Cr(CO)_6$	2000	2000	191.8 [71]	114.1 [71]
$Mn(CO)_6^+$	2090	2115		

Table 3.1: Vibrational frequencies of the CO bond and bond distances in metal carbonyls.

UV-vis absorption spectroscopy allows for the probing of the unoccupied valence states. The first UV-vis absorption spectrum of iron pentacarbonyl in the liquid phase was recorded in 1969 [77]. The first absorption spectrum of iron pentacarbonyl in the gas phase for wavelengths $200\,nm - 350\,nm$ was published in 1989 [78]. This spectrum is shown in Figure 3.5. It includes a wide absorption band at wavelengths below $300\,nm$.
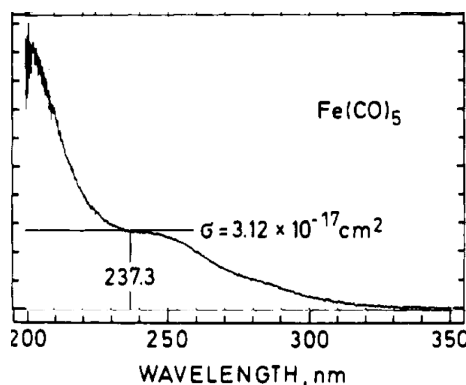

Figure 3.5: Shown is the UV-visabsorption spectrum of iron pentacarbonyl [78].

Three excited states, a^1E', $^1A_2''$, and b^1E' can be reached with a $266\,nm$ photon via an optically allowed transition [78]. The a^1E' state is equivalent to the $1^1E'$ state, the b^1E' state is equivalent to the $2^1E'$ state in the nomenclature used by Trushin

et al. Calculations by Rubner et al. and Wernet et al. confirm that the dominating contribution to the absorption derives from metal-to-ligand charge transfer (MLCT) transitions $(d \rightarrow \pi^*_{CO})$ in the range $240\,nm - 290\,nm$ to the states $^1A''_2$ and b^1E' [79, 80]. The values of these transitions are summarized in Table 3.2. The calculations have been carried out under the assumption of a D_{3h} and a C_{2v} symmetry. The error for the values in the first two columns is less than $5\,\%$ [79]. The same values are compared in Figure 3.6. In all calculations the ligand field (LF) state a^1E' has the lowest energy. The difference between the two MLCT states, $^1A''_2$ and b^1E', is with $\Delta E < 0.3\,eV$ in all calculations small compared to the difference between the MLCT and the LF state.

state	CASSCF / eV [79]	MR-CCI / eV [79]	RASSCF / eV [81]
$^1A'_1 \rightarrow a^1E'$	3.98	3.30	4.6
$^1A'_1 \rightarrow a^1E'$	4.04	3.56	
$^1A'_1 \rightarrow {}^1A''_2$	4.87	4.59	5.2
$^1A'_1 \rightarrow b^1E'$	4.82	4.88	5.2
$^1A'_1 \rightarrow b^1E'$	4.75	4.87	5.0

Table 3.2: Transition energies for the $Fe(CO)_5$ ground state to the electronically excited states.
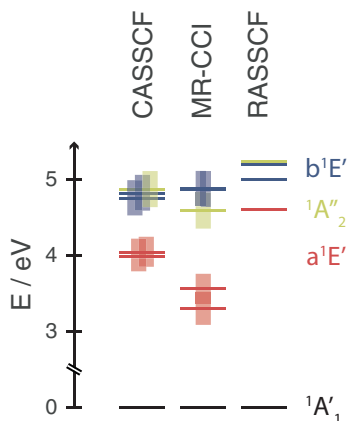
Figure 3.6: Illustrated are the transition energies for the $Fe(CO)_5$ ground state to the electronically excited states [79][81]

How much energy is required to detach one of the $Fe(CO)_5$ ligands? The electron affinity for $Fe(CO)_5$ has been determined to be between $(2.1 - 2.4\,eV)$ [82, 83]. This energy is required to detach the first ligand. The dissociation can be induced effectively if the photon energy coincides with the energy of the allowed transitions to the excited states. The dynamics of the dissociation take place on a sub picosecond timescale. They have been investigated by transient ionization.

Yardley et al. studied the distribution of the fragments $Fe(CO)_n$, $n = 0, ..., 5$ as a function of the excitation wavelength. An extensive fragmentation of the molecule was

observed. Yardly et al. and others tended towards a sequential dissociation [84, 85]. The first time-resolved PES experiment supported a concerted dissociation mechanism. The fragments $n = 2, 3, 4$ of $Fe(CO)_n$ were found within $100\,fs$ after the excitation with $400\,nm$ pulse. The fragments $n = 1, 0$ appeared after $230\,fs$ [86, 87].

Snee et al. studied the dissociation of $Fe(CO)_5$ in the liquid phase. They could not find fragments $n < 4$ and consequently argued for a sequential dissociation mechanism. Today we know that $Fe(CO)_5$ decays to $Fe(CO)_4$ which can transfer its excess energy to the solvent before dissociating further [88].

The model of a sequential dissociation was also supported by the results of gas phase transient ionization experiments which showed an increase in the delay with decreasing fragment size [9].

Trushin et al. induced the photodissociation of $Fe(CO)_5$ in the gas phase with an ultrafast pump pulse. The arrival times of the ionic fragments were recorded to extract the time constants of the reaction steps.

They used the experimental data with a temporal resolution of $182\,fs$ to model the excited state dynamics. Four time constants were required to model the pathway of the wave packet leading from the electronically excited $Fe(CO)_5$ to the lowest singlet state of $Fe(CO)_4$. Within this model, the molecule is lifted in energy from the $^1A_1$ ground state to the excited state upon absorption of a $266\,nm$ photon, see Figure 3.7. Two different MLCT states can be reached with this energy the $1A_2''$ and the $2E'$ state. Trushin et al. argue that the velocity of the following dynamic requires that the majority of the direct excitation ends up in the $2E'$ state. The potential energy curve of the $2E'$ state as function of the reaction coordinate is steeper than the curve of the $1A_2''$ state [89]. The two states are close in energy and the molecule can quickly transition from the $2E'$ state to the $1A_2''$ state and return. Whether one or two of these MLCT states are initially populated is experimentally difficult to distinguish. With the time constant $\tau_1 = 21\,fs$ the population of both of these states shifts to the LF state $1E'$. From here the wave packet moves on the $1E'$ surface along the $q(e')$ coordinate. This coordinate is likely the $Fe-C$ bond distance or the $C-O$ bond distance. This movement is associated with the time constant $\tau_2 = 15\,fs$. The next time window $\tau_3 = 30\,fs$ is associated with the movement on the same surface along the $Fe-CO$ bond elongation. The structure of the molecule rearranges via a non-Berry pseudorotation while the first ligand is disjointed [90]. $Fe(CO)_4$ is primarily generated in the $^1B_2$ state, an electronically excited state. The fourth time constant $\tau_4 = 47\,fs$ is associated with the transition to the lowest singlet state of $Fe(CO)_4$ via internal conversion through a Jahn-Teller-induced conical intersection. Sufficient energy remains in the vibrational modes of $Fe(CO)_4$ to drive an additional reaction. $Fe(CO)_4$ decays to $Fe(CO)_3 + CO$. The decay is associated with $\tau_5 = 3300\,fs$ [9].

Figure 3.7: Illustration of the model for the photoinduced dynamics in $Fe(CO)_5$ by Trushin et al. A wave packet travels along the potential energy surface while the first two ligands are disjointed and the geometry of the molecule rearranges [9].

3.2 The Photoinduced Dynamics of Iron Pentacarbonyl

Can the Trushin model be supported with time-resolved photoelectron data? Before we get into the details of the data, the nomenclature in the multi-electron picture has to be introduced. The states are labeled with numbers, upper case letters, and apostrophes. The letter refers to the symmetry of the orbital or state. The superscript number in front of the letter refers to the spin state, for instance ^1E indicates a singlet state and ^3E indicates a triplet state. For molecular states, the regular sized number in front of the letter enumerates states of the same symmetry according to their energy. This implies that the order of the states can depend on the results of a calculation and that the terms can switch depending on the results!

For the experiments presented in this thesis, $Fe(CO)_5$ was used as purchased from Sigma-Aldrich with a $99.99\,\%$ purity. The sample was evaporated into the vacuum chamber. The chamber pressure with the sample was kept at $2 \cdot 10^{-6}\,mbar$. The background pressure without a sample was at $6 \cdot 10^{-8}\,mbar$. The photodissociation was induced with an ultrafast $263\,nm$ pulse and the PE spectrum was probed with an ultrafast XUV pulse ($23.25\,eV$) for the delays $-750\,fs < t < 600\,fs$ in steps of $20\,fs$. This set of spectra has been recorded numerous times and summed. A retardation potential of $3\,V$ blocked slow electrons. The differences in the PE signal are small because the dynamic is induced only in a fraction ($< 5\,\%$). Still, a wealth of information can be extracted from this experimental data set.

The PE spectrum of $Fe(CO)_5$ in the range of $E_{bin} < 20\,eV$ is shown in Figure 3.8 a) and b). In the logarithmic representation it could appear as if data points are missing in the region $2\,eV < E_{bin} < 4\,eV$. The background was so low in this region that for some data points zero counts were collected. Here, these data points with $log(0) = -\inf$ are omitted. The spectrum can be separated into three bands, see Figure 3.8 a) one to three. The intensities within these bands have been assigned to individual states, based on calculations [91]. The first two bands at $E_{bin} = 8.26\,eV$ and $E_{bin} = 9.60\,eV$ have been assigned to the states $1^2E'$ and $1^2E''$, respectively. These states correspond to an $Fe(CO)_5^+$ where the $HOMO$ or the $HOMO^{-1}$ is ionized. Since these two molecular orbitals have a strong metal character i.e., $Fe(3d) + CO(2\pi) + Fe(4p)$ and $Fe(3d) + CO(2\pi)$, I will refer to the two peaks in the spectrum as metal or $Fe(3d)$ lines.
The third band can be assigned to states with a large ligand character i.e., in the final ionic state one orbitals with a ligand character is ionized [91]. The bands one and two are discussed first, the third band will be discussed later in this section.

The traces of $Fe(3d)$ lines reflect the dynamics induced by the $263\,nm$ pump pulse, see Figure 3.8 c). At early delays $-700\,fs < t < -250\,fs$ the intensity remains constant for both states. At larger delays, $-250\,fs < t$, the intensity decreases. For $1^2E''$ the intensity remains constant after the initial decrease. Whereas for $1^2E'$ the intensity rises again at delays $200\,fs < t$. For now, the focus is on the delays around $-100\,fs < t < 100\,fs$. The two level dynamic is fit for the delays $-700\,fs < t < 200\,fs$ at $E_{bin} = 8.26\,eV$ and for the delays $-700\,fs < t < 600\,fs$ at $E_{bin} = 9.60\,eV$ with an energy window of $0.4\,eV$ around the maximum. The fit function is constructed from the complementary error function $erfc$

$$I(t) = a \cdot erfc((t - t_0)/\sigma) + c \tag{3.1}$$

with the amplitude a, the time t, the center t_0, the width σ, the background c, and the intensity $I(t)$. The following values are taken from the fit. The intensity of the $1^2E'$ state decreases by $2.42\,\%$ at a delay of $(-128 \pm 50)\,fs$. The intensity of the $1^2E''$ state decreases by $4.72\,\%$ at a delay of $(-48 \pm 20)\,fs$. Both dynamics are related to the depletion of the $Fe(CO)_5$ ground state via the pump pulse. Why do the delays differ by $80\,fs$? It is likely that the trace at $9.60\,eV$ represents not only the depletion of a single species but a convoluted dynamic. The peak at $4.5\,eV$ in Figure 3.8 b) is the $Fe(3d)$ line of $Fe(CO)_5$ in the excited state and will be discussed in detail below. The peaks in the ligand region could also be shifted by a similar amount and the peak flank from $13.6\,eV$ would then appear at $9.84\,eV$ and contribute to the trace. The ligand region will be discussed later in this section. There we will see that the falling edges are located at delays between $-200\,fs$ and $-47\,fs$ depending on the energy. On
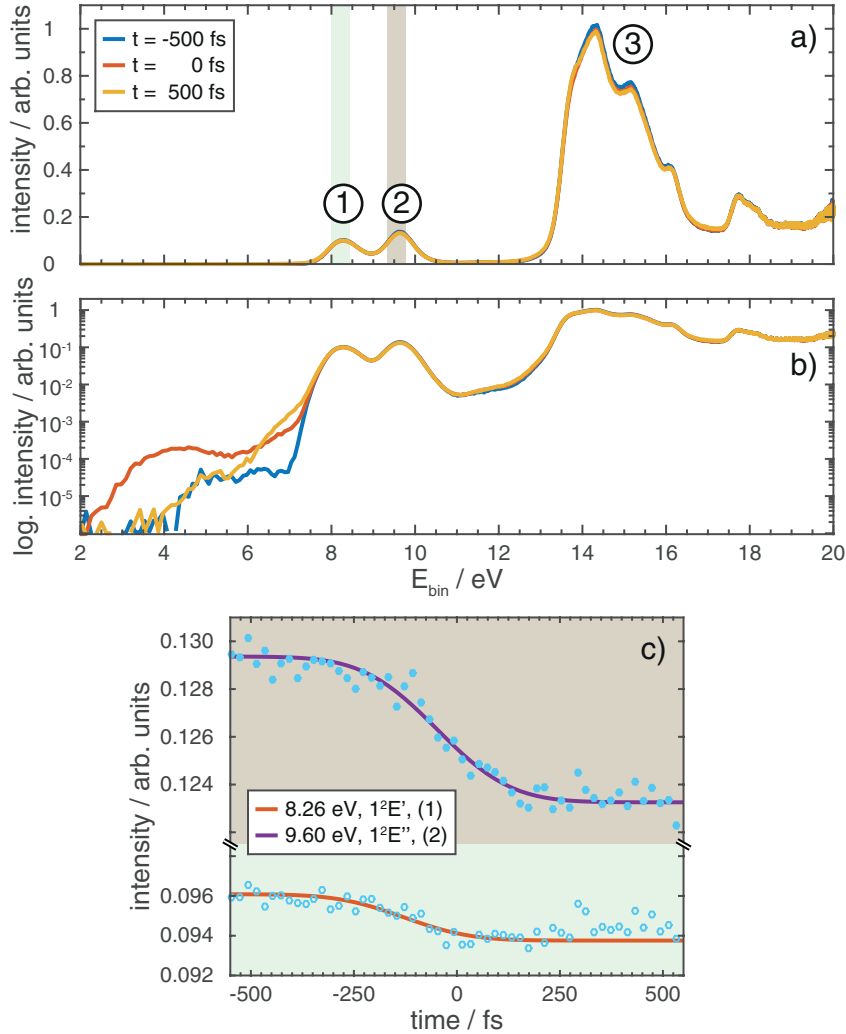
Figure 3.8: Photoelectron spectra of $Fe(CO)_5$ before and after pumping with $263\,nm$ photons in linear (a) and logarithmic (b) representation. (c) Traces of the two intensity maxima $E_{bin} = 8.26\,eV$ and $E_{bin} = 9.60\,eV$

one hand, it is surprising that the center of the decreases of the traces are located around a delay of $-100\,fs$ compared to the center of the sideband. On the other hand, the sideband was determined with an accuracy of only $26\,fs$. The difference is well below the overall temporal resolution of $262\,fs$. The analysis is not affected by this difference since absolute times are not discussed.

Changes in the spectrum of $Fe(CO)_5$ are observed at binding energies below the $Fe(3d)$ lines i.e., $2\,eV < E_{bin} < 8\,eV$. A new peak appears temporarily but its intensity is so low compared to the $Fe(3d)$ lines it becomes only evident in the logarithmic representation, see Figure 3.8 b). The dynamics can be displayed in a representation of the intensity as function of both energy and delays between the pump and probe pulse. This is shown in the two dimensional map in Figure 3.9. In the following the details of this map are studied using the cuts in the dimension of energy and time.
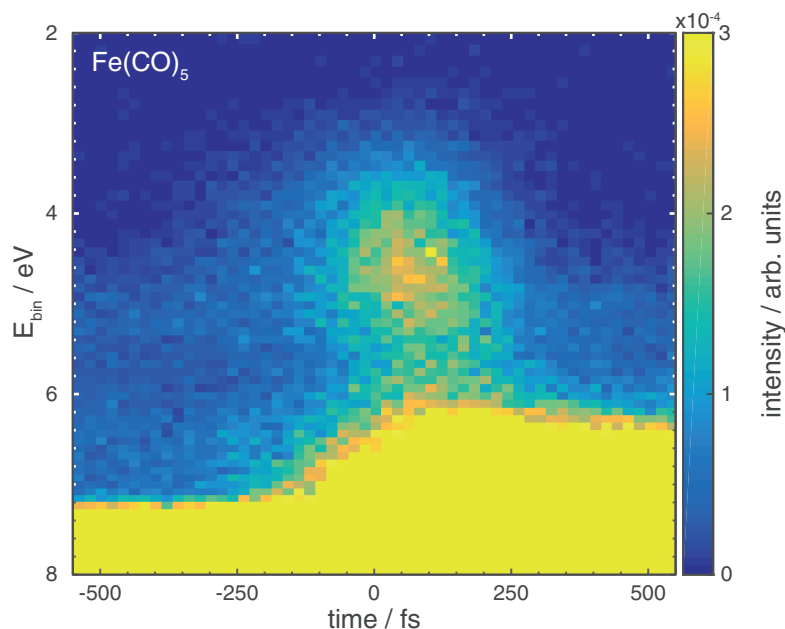
Figure 3.9: Photoelectron spectrum of $Fe(CO)_5$ excited state as function of energy and time.

The earliest rise of intensity in the spectrum after the depletion of the $1^2E'$ and $1^2E''$ states is found a binding energy of $E_{bin} = 4.4\,eV$. The intensity is about 200 times weaker than the $1^2E'$ signal. The short lived signal has its center at positive delays. A sideband of the $Fe(3d)$ line should be located at $t = 0\,fs$ and at an energy of $E_{bin} = 8.26\,eV - 4.71\,eV = 3.55\,eV$. Therefore, the possibility that the short lived signal is a sideband is excluded. Based on calculations by Rubner et al. this signal is assigned to the electronically excited intermediate state, an MLCT state, of $Fe(CO)_5$ [79].

Are the data in agreement with the model by Trushin? Can we find two close lying MLCT states and the LF state? The data are fit with three different models to answer these questions. At early delays ($-500\,fs$) and a binding energy of $E_{bin} < 4\,eV$ we detect no specific signal. Between $4\,eV < E_{bin} < 7\,eV$ there is a weak signal which stays constant over the full investigated delay range. This constant weak signal derives from a contamination with another harmonic (H13) and is, hence, subtract ($I'(t) = I(t) - I(t = -600\,fs)$). At higher energies, $6\,eV < E_{bin}$, the signal of the $1^2E'$

state can be found. This signal shifts to a lower binding energy for larger delays, which we will study later in detail. One can observed how the signal around $E_{bin} = 4.5\,eV$ rises and vanishes in the range of $-200\,fs$ to $+200\,fs$, see Figure 3.10 a) and b). This signal reflects the first population of a state after pumping. The signal shifts towards a higher energy for larger delays. The highest intensity is reached at $60\,fs$. The data are fit at $\pm 50\,fs$ of this center with the first model: a simple Gaussian

$$G(E) = a\,exp\left(-\frac{(E-E_0)^2}{2\sigma^2}\right) \tag{3.2}$$

The corresponding traces at $13\,fs$ and $133\,fs$ are shown in Figure 3.10 c), the corresponding fits are shown in Figure 3.10 d). The centers are located at $(4.50 \pm 0.19)\,eV$ and $(4.71 \pm 0.09)\,eV$. The difference between the two, $0.21\,eV$, is close to the predicted difference between the MLCT states [79]. This indicates the involvement of at least two excited states in this specific energy region.

The intensity as a function of time for $400\,meV$ energy slots is shown in Figure 3.11 a) and b). At lower binding energies, $3\,eV < E_{bin} < 5.2\,eV$, the dynamics of the excited state(s) can be observed. The rise time of the signals in the range $3\,eV < E_{bin} < 5.2\,eV$ is similar. The signal at energies $E_{bin} > 5.2\,eV$, on the other hand, appears at greater delays. The slope of the falling edge differs significantly for the traces at energies $E_{bin} > 4\,eV$.

At higher binding energies a signal can be found which belongs at negative delays to the $Fe(CO)_5$ $1^2E'$ state. At positive delays a shift of the rising edge from $7\,eV$ to $6\,eV$ can be observed. The signal in the region $6\,eV < E_{bin} < 7\,eV$ decays much slower than any excited state of $Fe(CO)_5$ or $Fe(CO)_4$. The curve at $6.8\,eV$ has a lifetime of above $500\,fs$. I will later discuss this signal in detail and reason that it can be assigned to a $Fe(CO)_4$ species.

The spectra at the delays $13\,fs$ and $113\,fs$ indicate two excited states at the energies $4.50\,eV$ and $4.71\,eV$. The traces at these two energies are fit with the second model: an exponentially modified Gaussian (EMG)

$$EMG(t) = \frac{a\sigma}{d}\sqrt{\frac{\pi}{2}}exp^{\frac{2\sigma^2}{d^2}-\frac{t-t_0}{d}}\,erfc\left[\frac{1}{\sqrt{2}}\left(\frac{\sigma}{d}-\frac{t-t_0}{\sigma}\right)\right] + c \tag{3.3}$$

The centers are located at $45\,fs$ and at $50\,fs$. The decay times are both $5\,fs$. However, the smallest time constant found in the photodissociation in metal carbonyls is $12.5\,fs$ [89]. The temporal resolution in these experiments is not sufficient to claim an even shorter time constant. In the following I will refer to these decay times as $\tau < 10\,fs$.
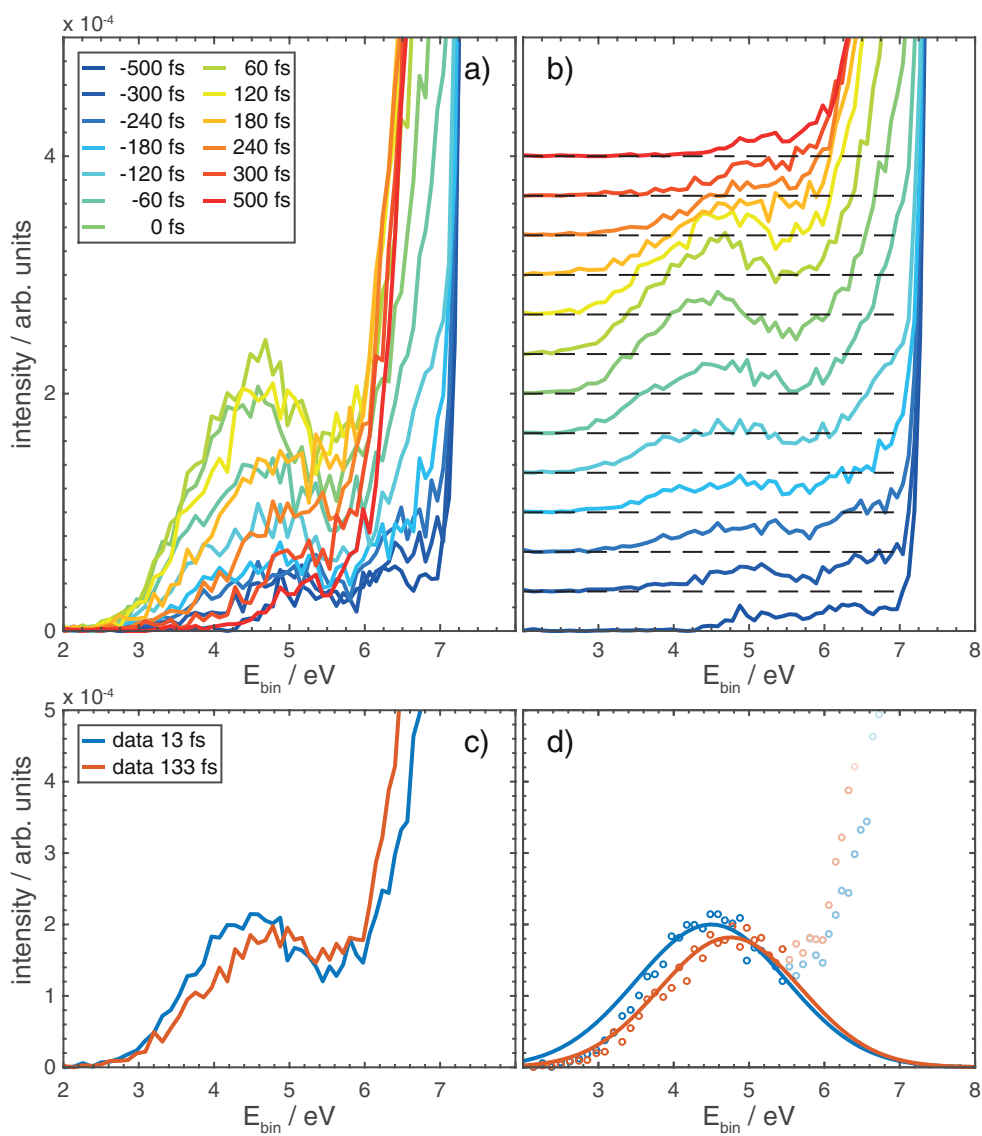
Figure 3.10: Spectrum of the electronically excited state of $Fe(CO)_5$ at various delays in (a) regular and (b) stacked representation. A shift of the intensity maximum can be observed if the spectra at a delay of $13\,fs$ and $133\,fs$ are compared. (d) A Gaussian fit of these maxima indicates a difference of $0.21\,eV$.
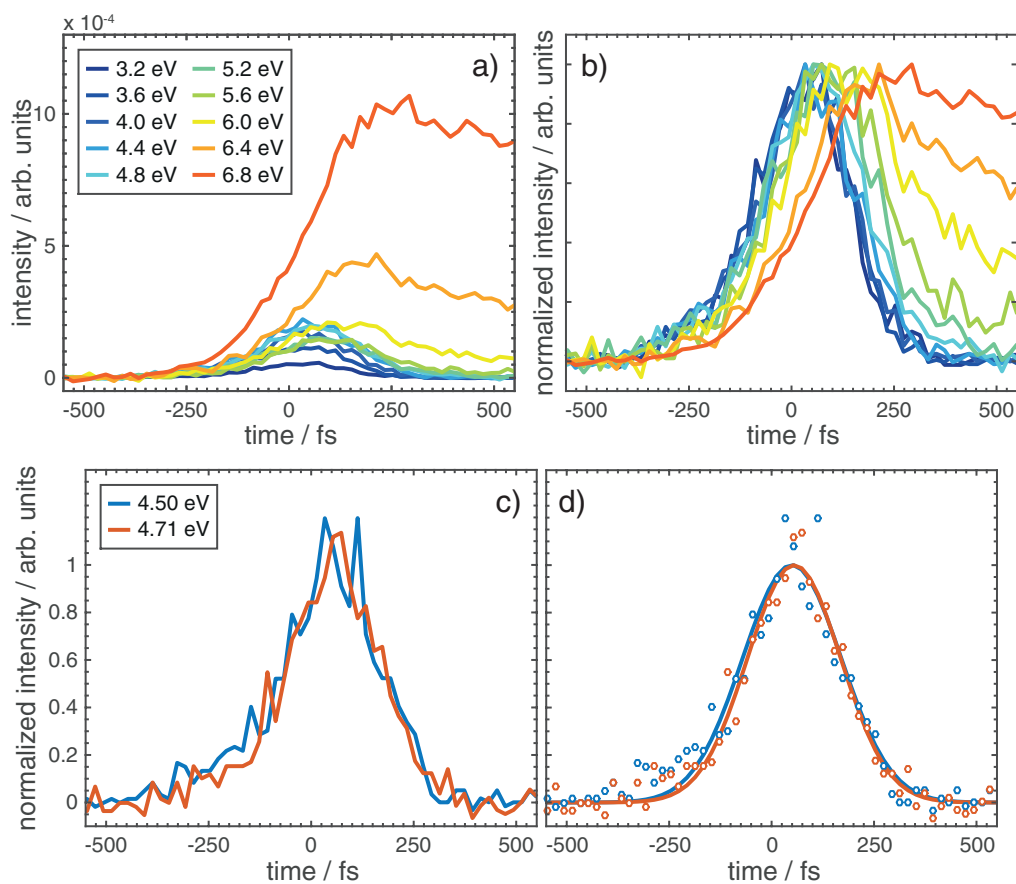
Figure 3.11: Traces of the $Fe(CO)_5$ excited state signal at selected energies with intensities (a) as measured and (b) normalized to the maximum of each trace. (c) The traces at $4.50\,eV$ and $4.71\,eV$ and (d) their EMG fits. The two traces are normalized to the maximum of the fit. The center of the two fits differ by $4.5\,fs$.

We have seen an indication for the involvement of more than one excited state from the perspective of the spectra and the traces. The data are now fit with the third model: two 2D-Gaussians in the time and energy domain ($2.0\,eV$ to $5.5\,eV$). Preferably, the data would be fit with an EMG-based model for the temporal component of the signal, however, the signal to noise level requires the simpler model. The difference between the two 2D-Gaussians is fixed to the proposed $21\,fs$ and $0.2\,eV$. The intensity ratio is kept at $1/1$. The position and width in time and energy as well as the intensity are fit parameters. These restrictions are well justified as we have learned from fitting the spectra, see Figure 3.10, and from fitting the traces, see Figure 3.11.

The data, the two fits, and the components of the two fits are presented in Figure 3.12. The quality of the fit reaches a value of $R^2 = 0.91$. The data are equally well fit with a single 2D Gaussian, however, considering the shift in energy and time, the two-2D Gaussian fit seems more realistic. The two Gaussians are centered in time at $(40 \pm 2)\,fs$ and $(61 \pm 2)\,fs$ and in energy at $(4.45 \pm 0.02)\,eV$ and $(4.65 \pm 0.02)\,eV$, confirming the previous findings.

In summary, two states with an energy difference of $0.21\,eV$ have been found by fitting two spectra at different delays with the first model. Fitting the traces at these energies with the second model allowed for the extraction of the population dynamics of the two states. They are located at a delay of $45\,fs$ and $50\,fs$ and decay both in less than $10\,fs$.

The parameters for the difference in energy from the first fit model and the difference in time proposed by Trushin have been used for the third model. This third model is based on two states and fits the data well. Here the peaks are located at $(40 \pm 2)\,fs$ and $(61 \pm 2)\,fs$. The peaks in the spectra can be interpreted as the two excited MLCT state states $^1A_2''$ and b^1E', in agreement with the model of Trushin.

A model based on a single 2D Gaussian fits the data equally well. However, the quality of the data is not sufficient to distinguish between the involvement of a single or two MLCT states.

If the assignment of the two excited states as MLCT states is correct, then there is no single peak which could be associated with the LF excited state of $Fe(CO)_5$. The LF state is expected close in time to the MLCT states and, based on the ground state calculations, at $(0.4 - 1.0)\,eV$ below the MLCT states, see Figure 3.13. Instead a decrease of the intensity towards higher binding energy up to $E_{bin} < 6\,eV$ and increasing delays can be observed. The low intensity is interpreted as an indicator that the wave packet moves quickly along the potential energy surface without crossing an intermediate state with a minimum.

To visualize the associated change in energy as function of time, the PE intensity is normalized for each energy slot to a range between zero and one. This ignores the absolute population and merely serves as an illustration, see Figure 3.14.
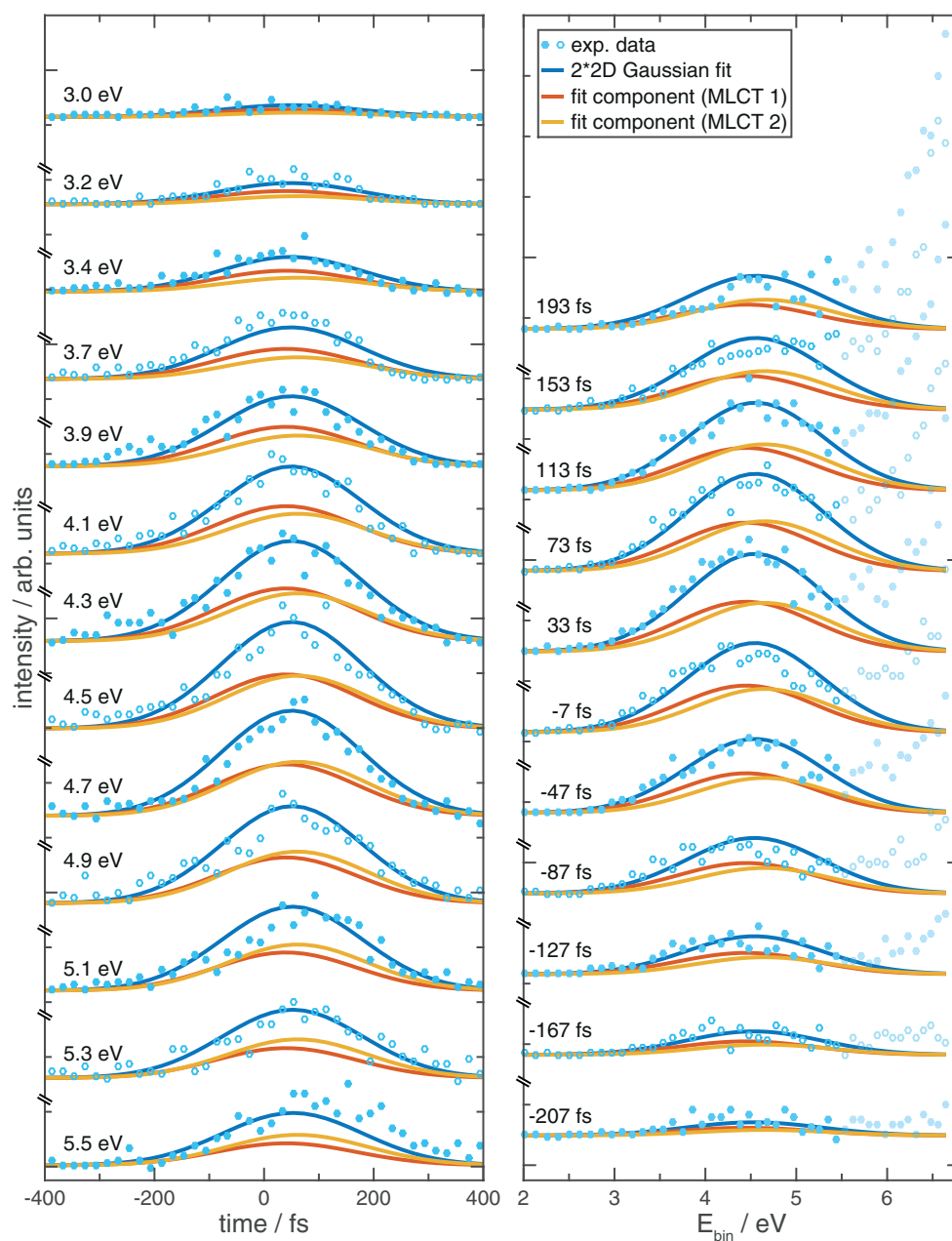
Figure 3.12: Cuts through the 2D photoelectron signal of $Fe(CO)_5$ are presented for selected energies (left) and for selected delays (right). The experimental data were fit with a model containing two 2D Gaussians, representing the MLCT states $1A_2''$ and $2E'$ (red and yellow). The transparent data points were not included in the fitting procedure.
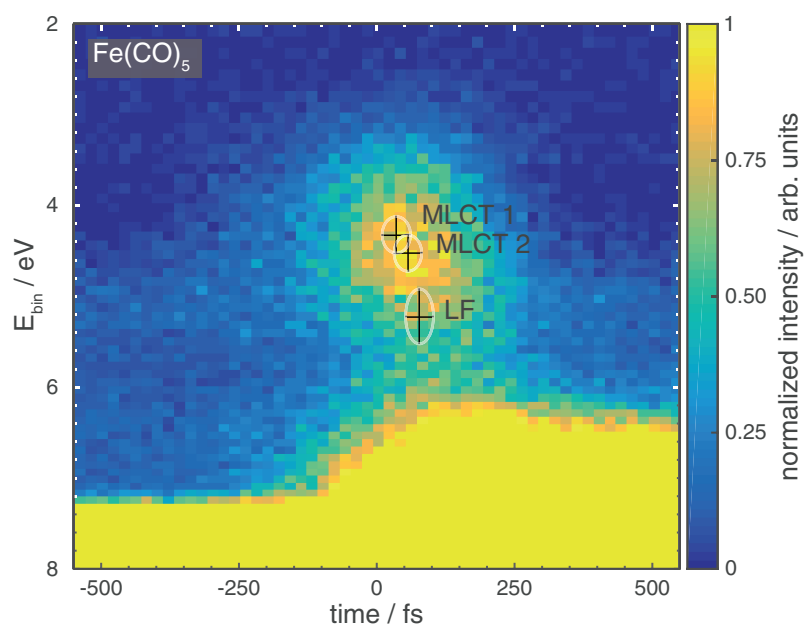
Figure 3.13: Marked on the map are the two MLCT states and the region where the ligand field excited state of $Fe(CO)_5$ is expected according to Trushin [9].
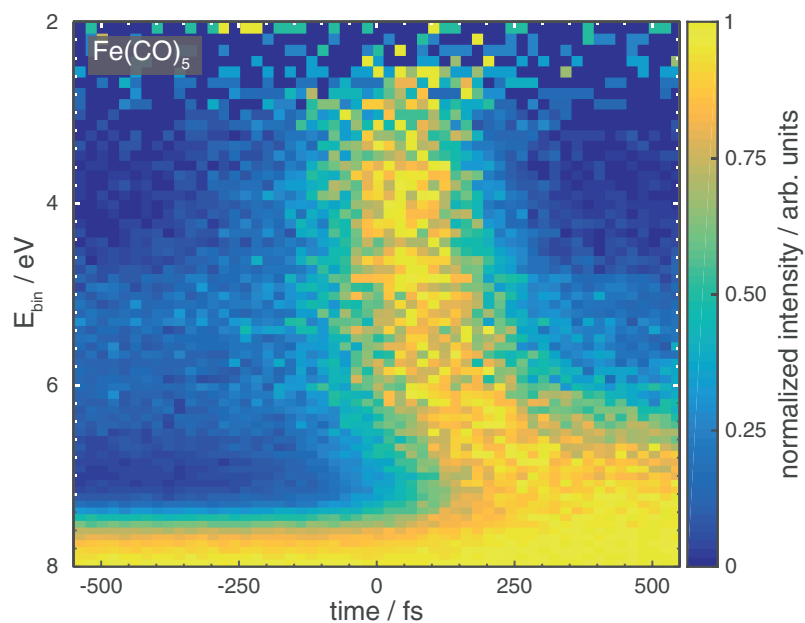
Figure 3.14: The spectra of the $Fe(CO)_5$ excited state normalized to the maximum along each energy channel representing the movement of the wave packet, independent of the population.

A high pump fluence can cause nonlinear effects. Are the dynamics that we have observed still in the linear regime? The spectra of $Fe(CO)_5$ at an average pump power of $P_{avg} = (0.06 - 1.41)\,mW$ which corresponds to a pulse energy of $P_{pulse}(263\,nm) = (63 - 470)\,nJ$. The spectra as function of the time of flight at a delay of $6.2\,ps$ are shown in Figure 3.15 a). Note that the relative peak intensities are different in the dimension of 'time of flight' compared to the dimension of 'energy' due to the nonlinear conversion between the two. This representation allows to show the absolute counts. All spectra of metal carbonyls shown in this thesis were probed at about $5500\,counts/s$. The differences spectra are calculated by subtracting the spectrum recorded at $P_{avg} = 0.06\,mW$ from each of the other spectrum. These difference spectra are shown in Figure 3.15 b). The effective change in the region of the $Fe(3d)$ lines is shown in Figure 3.15 c). I find that the pump effect i.e., the integrated absolute intensity in the $Fe(3d)$ region of the difference spectra, dependence linearly on the pulse energy in the range used in the experiments. The red curve is a linear fit of the data.
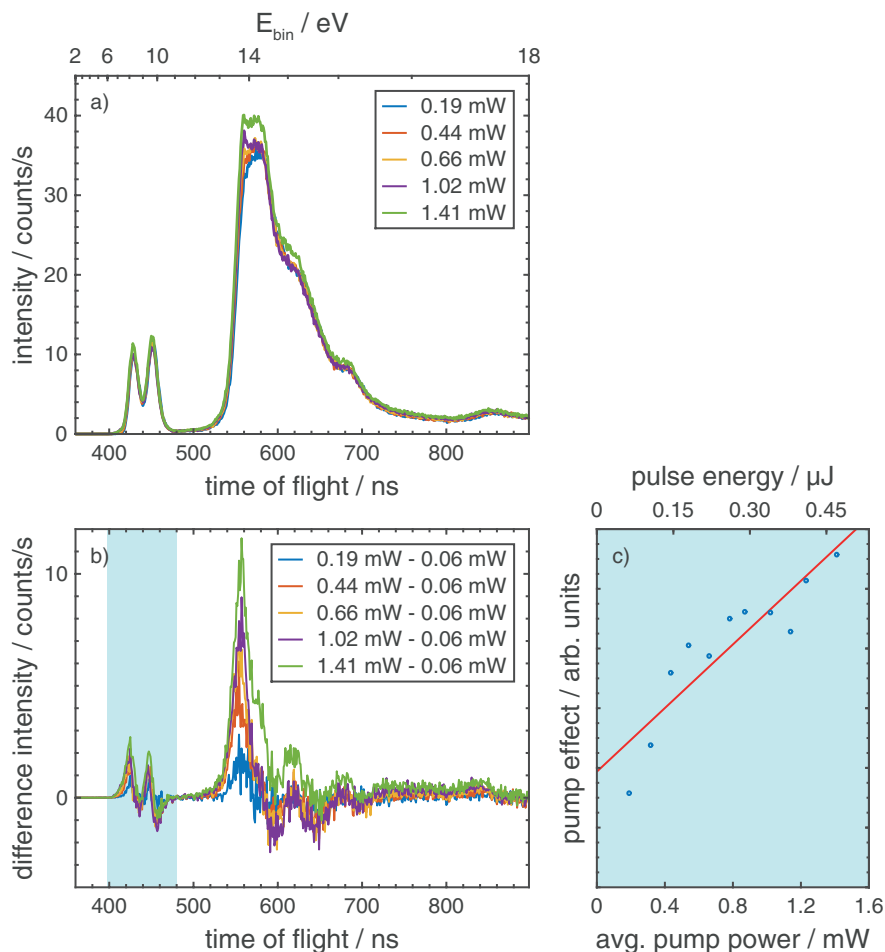
Figure 3.15: a) The spectrum of $Fe(CO)_5$ recorded at various pump powers at a delay of $6.2\,ps$. b) Difference spectra of a) i.e., the spectrum at a pump power of $P_{avg} = 0.06\,mW$ is subtracted from the spectra at a specific pump power. The integral of the $Fe(3d)$ region (blue region) is shown in Figure c). The pump pulse had energy of $P_{pulse}(263\,nm) = (63 - 470)\,nJ$ at a frequency of $3\,kHz$ and Gaussian beam profile with a FWHM of $H = 135\,\mu m$ and $V = 77\,\mu m$.

If we further follow the dynamics of the wave packet, we have to keep in mind that one of the ligands is already disjoint and the molecule rearranges towards the geometry of $Fe(CO)_4$. The molecule is left with excess energy from the $263\,nm$ pump. Trushin et al. predicted that the dissociation leads to a $Fe(CO)_4$ molecule in the electronically excited $^1B_2$ intermediate state from where it passes to the lowest singlet state $^1A_1$. Can we find evidence of this intermediate state in the photoelectron spectra? Can we deconvolute the spectra to calculate the spectrum of pure $Fe(CO)_4$, although the concentration is below $5\,\%$?

The spectra at delays $200\,fs < t$ are the sum of the $Fe(CO)_4$, the CO, and the $Fe(CO)_5$ spectra. A model is set up for the extraction of the $Fe(CO)_4$ spectra $I_{Fe(CO)_4}$ from the sum I_{sum}

$$I(t)_{sum} = c_1(t)\,I_{Fe(CO)_5}(t) + c_2(t)I_{Fe(CO)_4}(t) + c_3(t)I_{CO}(t) \qquad (3.4)$$

Where $c_1(t)$, $c_2(t)$, and $c_3(t)$ are the concentrations of $Fe(CO)_5$, $Fe(CO)_4$, and CO in the probing volume. At early delays, $t < -500\,fs$ the spectrum represents the signal of a pure $Fe(CO)_5$ sample. A pure CO spectrum has been recorded separately. $Fe(CO)_4$ and $Fe(CO)_5$ are assumed to have the same cross section. The sum of $I_{Fe(CO)_5}(t)$ and $I_{Fe(CO)_4}(t)$ remains constant in a region of the spectra with no contribution of I_{CO} because the molecules are to slow to exit the probing volume within a delay range of $\pm 10\,ps$. From this conservation of molecules $c_1(t) + c_2(t) = const$ follows. We are only interested in the ratio and, hence, we can choose $const = 1$:

$$c_1(t) = 1 - c_2(t) \qquad (3.5)$$
$$I_{sum} = (1 - c_2(t))I_{Fe(CO)_5} + c_2(t)I_{Fe(CO)_4} \qquad (3.6)$$

This is valid for $E_{bin} < 13\,eV$, where CO does not contribute intensity, see Figure 3.16 a). No experimental method is available for the determination of the coefficients $c_2(t)$. $c_2(t = 500\,fs)$ is increased gradually and the pure $I_{Fe(CO)_5}(t = -500\,fs)$ is subtracted with the restriction that the intensities must remain positive.

I tried to subtract the CO spectrum with the same boundary condition. Even for a CO concentration below $1\,\%$ the intensities turn negative. The reason has not been found yet. Without the subtraction of the CO spectrum a peak at $14\,eV$ remains at large delays, see Figure 3.16 b), which was not observed by Wernet et al. [92]. However, the signal at $E_{bin} < 13\,eV$ should not be affected. This spectrum of $Fe(CO)_4$ is referred to as scaled difference intensity.

I observe that the $Fe(3d)$ lines of $Fe(CO)_4$ are located at a lower binding energy, compared to the $Fe(3d)$ lines of $Fe(CO)_5$. The splitting between the two $Fe(3d)$ lines is smaller in $Fe(CO)_4$ than in $Fe(CO)_5$.

After the arrival of the pump pulse the intensity of the $Fe(CO)_4$ $Fe(3d)$ lines increase, see Figure 3.16 d). The lower energy trace at $5.9\,eV$ decreases again to almost zero at large delays. The traces at larger energies however do not seem to decay completely. Additional time-resolved PE spectra for the range of several picoseconds confirm this impression. The traces, binned and non binned, up to $1\,ps$ are shown in Figure 3.16 e). They reveal peak short in time close to the rising edge and a signal lasting for picoseconds. This short lived signal is an indicator for yet another intermediate state. The long lived signal is assigned to the lowest singlet state $^1A_1$ of $Fe(CO)_4$. The weaker short lived signal is extracted by subtracting a two dimensional model of the long lived signal of the $^1A_1$ state. The model is composed of a Gaussian in the energy dimension

$G(E)$ and the sum of an EMG $EMG(t)$ and a Gaussian $G(t)$ in the dimension of time.

$$I(E,t) = G(E) \cdot EMG(t)G(t) \tag{3.7}$$

The time-averaged spectrum ($500\,fs < t < 600\,fs$) is fit with the energy dependent Gaussian component $G(E)$ for $E_{bin} < 9.32\,eV$, see Figure 3.16 c). The center is located at $7.93\,eV$ with a width of $0.79\,eV$. The width of the fit is overestimated and a reduction of the width to $0.60\,eV$ improves the model. At this center energy the trace is fit in time $EMG(t)G(t)$, see Figure 3.16 f). The Gaussian component in time $G(t)$ represents the short signal, the EMG component the long signal. The energy dependent Gaussian is combined with the time dependent EMG component to the two dimensional model of the signal of the $^1A_1$ state. The model data is subtracted from the pure $Fe(CO)_4$ data set.

We are now left with filtered spectra that should show the intermediate state. At energies $E_{bin} < 6\,eV$ the excited states species of $Fe(CO)_5$ contributes significantly to the spectrum, as discussed in the beginning of this section. The data are fit in the range of $5.98\,eV < E_{bin} < 8.13\,eV$ and $-600\,fs < t < 400\,fs$ where the contribution from other species is low. The two dimensional model of the fit consists of an energy depended Gaussian and a time dependent EMG, see Figure 3.16. The center in energy dimension is located at $7.40\,eV$, the center in the time dimension is located at $(83 \pm 8)\,fs$. The lifetime is $< 10\,fs$.

The difference in time with respect to the first excited state, $^1A_2''$ or b^1E', of $Fe(CO)_5$ is $43\,fs$. Trushin proposed that the $^1B_2$ state of $Fe(CO)_4$ is reached $66\,fs$ after excitation. A lifetime of less than $10\,fs$ is found for the $^1B_2$ state by fitting the PE data. In the Trushin model the fourth time constant τ_4 is assigned to the transition from the $^1B_2$ to the $^1A'$ state of $Fe(CO)_4$. τ_4 is with $47\,fs$ significantly larger than the lifetime found with the PE data. The center of the fit of the $^1B_2$ state is located at $7.40\,eV$, about $0.63\,eV$ below the lowest singlet state of $Fe(CO)_4$ ($7.93\,eV$) or $0.82\,eV$ below the ground state of $Fe(CO)_5$.

Wernet et al. calculated the energy of the $^1B_2$ and $^1A_1$ states of $Fe(CO)_4$ for five different geometries. They predict the $^1B_2$ to be located $2.6\,eV$ to $3.7\,eV$ below the $^1A_1'$ $Fe(CO)_5$ ground state depending on the species type i. e., triplet, singlet, or excited. The lowest singlet state $^1A_1$ of $Fe(CO)_4$, of the same species, is located between $2.0\,eV$ to $2.9\,eV$ above the $Fe(CO)_5$ ground state. The difference between the $^1B_2$ and the $^1A_1$ states is in three cases $(0.6 - 0.7)\,eV$ and in two cases $(1.1 - 1.2)\,eV$ [80]. The short lived signal at $E_{bin} = 7.40\,eV$ is assigned to the $^1B_2$ state $Fe(CO)_4$, based on the proximity in time to the value predicted by Trushin et al. and the proximity in energy to the value predicted by Wernet et al.

We now have the binding energy for the $^1A_1'$ state of $Fe(CO)_5$ and the $^1B_2$ and the $^1A_1$ states of $Fe(CO)_4$. Wernet et al. have calculated the energies for these three states in order to determine the spin state for three possible geometries of $Fe(CO)_4$. The geometries are optimized for the triplet ground state, the lowest singlet state, and the excited state ($^1B_2$) of $Fe(CO)_4$: $Fe(CO)_4T$, $Fe(CO)_4S$, and $Fe(CO)_4E$, respectively. The energy difference between the $^1B_2$ and the $^1A_1$ states of $Fe(CO)_4$ is the same for the $Fe(CO)_4T$ and the $Fe(CO)_4E$ geometry: $\Delta E = 0.9\,eV$. For the $Fe(CO)_4S$ geometry the energy difference is larger: $\Delta E = 1.1\,eV$ [80].
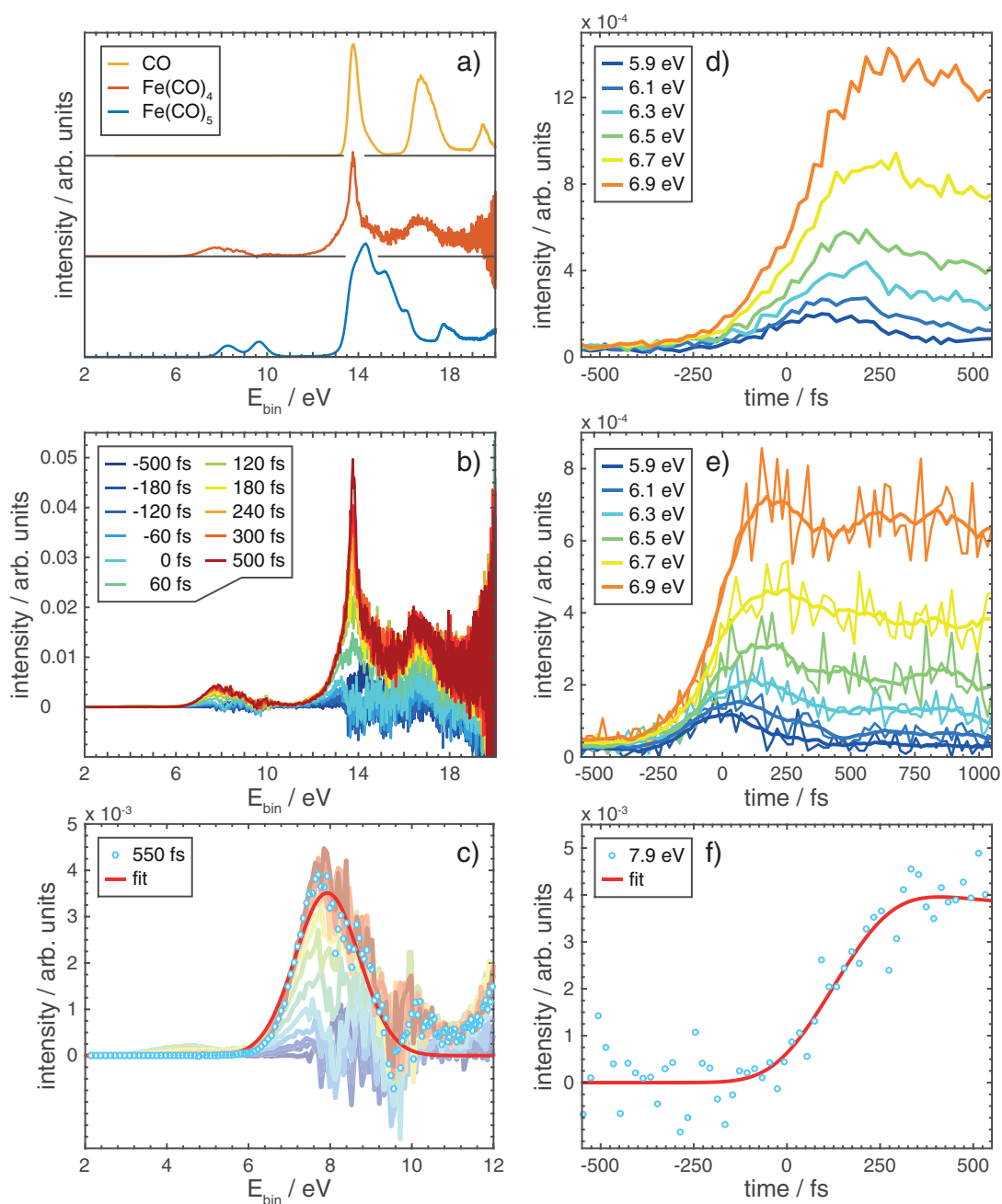
Figure 3.16: Shown are (a) the extracted pure spectra of $Fe(CO)_5$, $Fe(CO)_4$, and CO, (b) the pure spectrum of $Fe(CO)_4$ ($^1A_1$) at selected delays and (c) at a delay of $550\,fs$ fit with a Gaussian.
Traces of the pure $Fe(CO)_4$ spectrum at selected energies for (d) femtosecond and (e) picosecond delays. A trace of the $Fe(CO)_4$ maximum at $7.92\,eV$ with its fit.

We have to be careful when comparing the theoretical to the experimental data. The calculations refer to the ground state and the experiment measures the corresponding final ionic state. Calculations which include the excitation and the ionization are computationally demanding and exceed the scope of this thesis. The experimental energy difference fits well to the calculated difference for a $Fe(CO)_4T$ and $Fe(CO)_4E$
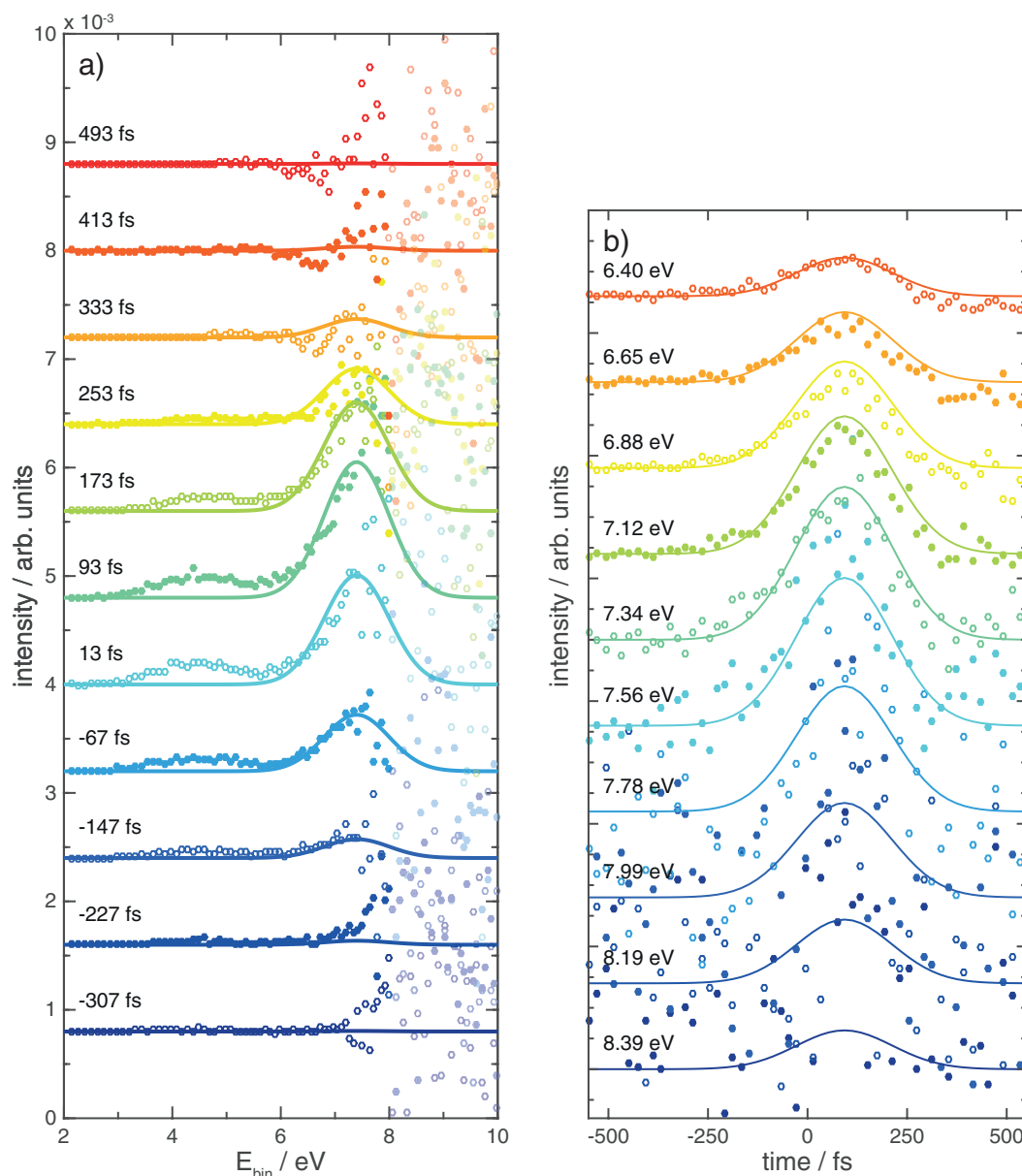
Figure 3.17: Shown are (a) the spectra and (b) the traces of the $Fe(CO)_4$ excited state ($^1B_2$) with cuts of the 2D-Gaussian fit.

geometry. But the energy difference between the $^1B_2$ and the $^1A_1$ states of $Fe(CO)_4$ and the $^1A_1'$ states of $Fe(CO)_5$ is much smaller in the experiment. A calculation which includes the final ionic state would allow to interpret the experimental data with a higher confidence.

Apart from these calculations it is rather difficult to speculate on the geometry of the intermediate species of $Fe(CO)_4$. With an effective valence electron count of 16 $Fe(CO)_4$ does not satisfy the 18 electron rule. This is why $Fe(CO)_4$ is much more reactive than $Fe(CO)_5$. The structure of $Fe(CO)_4$ has been determined experimentally by Ihee et al. [93]. They found $Fe(CO)_4$ in the singlet state $^1A_1$. Later studies also observed the triplet ground state in solution. According to the Trushin model, $Fe(CO)_4$ in the gas phase does not occur in the triplet ground state.

geometry	$E(^1B_2)/eV$	$E(^1A_1)/eV$	$\Delta E/eV$
Fe(CO)4T	2.6	2.0	0.6
Fe(CO)4S	3.2	2.1	1.1
Fe(CO)4E	3.5	2.9	0.6

geometry	$E_{bin}(^1B_2)/eV$	$E_{bin}(^1A_1)/eV$	$\Delta E/eV$
exp. data	0.82	0.29	0.53

Table 3.3: Calculated energy of the $^1B_2$ and the $^1A_1$ states of $Fe(CO)_4$ with respect to the $^1A_1'$ ground state of $Fe(CO)_5$, as well as the measured energy for the final ionic state of the $^1B_2$ and the $^1A_1$ states of $Fe(CO)_4$ with respect to the $^1A_1'$ ground state of $Fe(CO)_5$ [81].

The data discussed so far does not indicate a decay of the $Fe(CO)_4$ ground state species within $9\,ps$. At first glance, this seems to contradict the proposed decay time of $\tau_{Fe(CO)_4} = 3300\,fs$. However, the contribution of $Fe(CO)_3$ in the spectrum is expected to be very small, the binding energies of the $Fe(CO)_3$ photoelectron lines are assumed to be similar to those of $Fe(CO)_4$. The only indication for further dissociation of $Fe(CO)_4$ in other PES experiments was based on the CO photoelectron signal [92]. Here, this CO signal is very small in the experiments and can explain the negligible contribution of $Fe(CO)_3$ in the present experiments.

This concludes the analysis of the first two bands of the $Fe(CO)_5$ photoelectron spectra. I have found intensity maxima which I assigned to the electronic ground state of $Fe(CO)_5$ and to the lowest singlet state of $Fe(CO)_4$, as well as to the intermediate states of electronically excited $Fe(CO)_5^*$ and $Fe(CO)_4^*$. The experiment presents the first direct observation of the intermediate states $Fe(CO)_5^*$ and $Fe(CO)_4^*$ $^1B_2$ in the gas phase with photoelectron spectroscopy. I have determined the delay t_0 of these states with respect to the cross-correlation signal of the pump and probe pulses, as well as their decay time τ with various fit models. The results are summarized in Table 3.4. The energies of these states have been compared to the literature data throughout the analysis. Do we now have a basis to interpret the PE spectra and learn about the excited state dynamics? Yes! We can combine the discussed fit models to illustrate how the molecule transitions between the states as a function of time. The PE spectra and the fits of the excited state region are shown in Figure 3.18 a) and b). Figure 3.18 a) is identical to Figure 3.9. We can now compare these spectra with the various fits that I have discussed in this section so far. The combined fits are shown in figure 3.18 b). At negative delays the two $Fe(CO)_5$ states $1^2E'$ and $1^2E''$ are depopulated by the pump pulse. Hereupon, the molecule transitions into the intermediate MLCT states of $Fe(CO)_5$, most likely $^1A_2''$ or b^1E'. The molecule then dissociates into CO and $Fe(CO)_4$ in the vibrationally hot and electronically excited intermediate state $^1B_2$. This intermediate then decays to the $^1A_1$ state, the lowest singlet state of $Fe(CO)_4$. A comparison of the time constants and decay times to the model proposed by Trushin can be found below, see section 3.4.
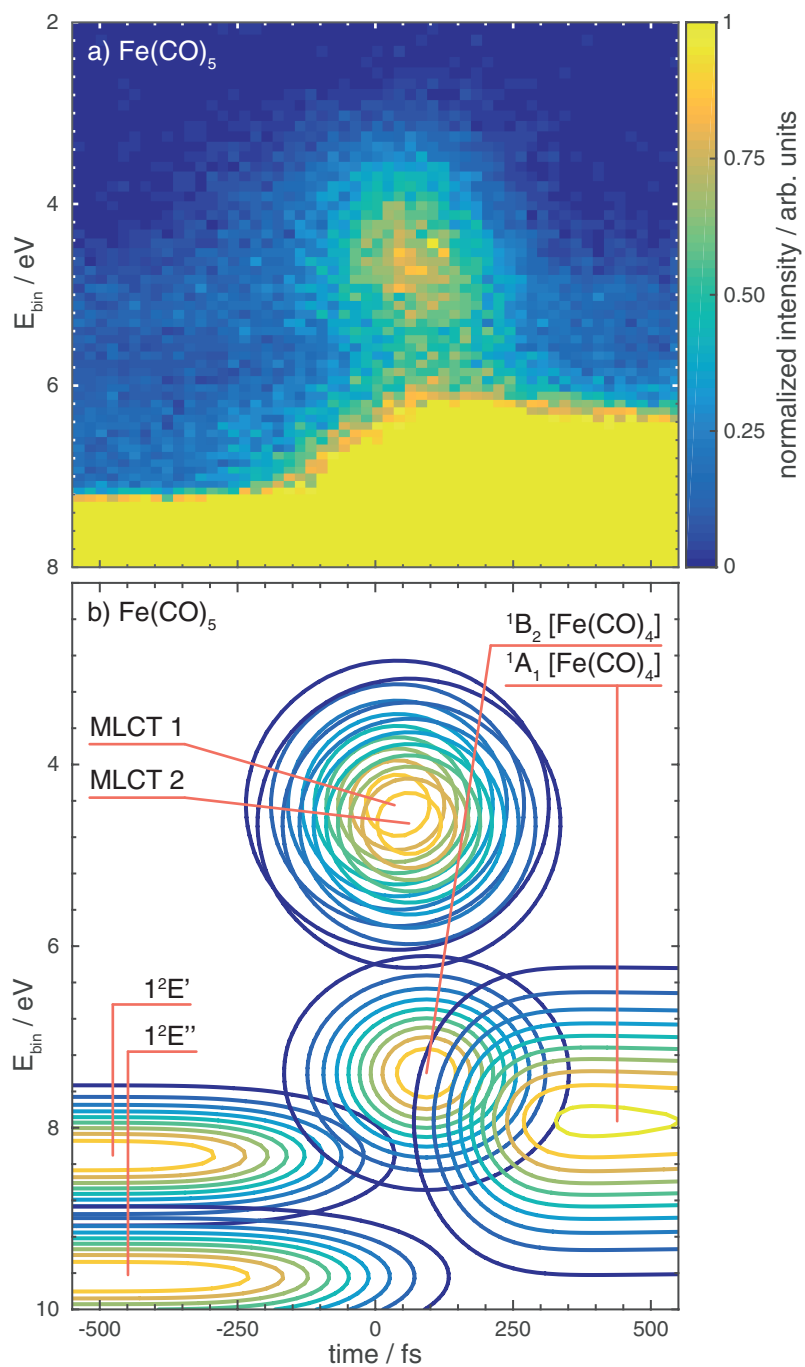
Figure 3.18: Shown are a) the spectra $Fe(CO)_5$ and b) the 2D fits.

| state	E_{bin}/eV	t_0/fs	τ/fs
$Fe(CO)_5$ $(1^2E')$	8.22	-	-
$Fe(CO)_5^*$ (MLCT 1)	4.50	40	< 10
$Fe(CO)_5^*$ (MLCT 2)	4.71	61	< 10
$Fe(CO)_4^*$ $(^1B_2)$	7.40	83	< 10
$Fe(CO)_4$ $(^1A_1)$	7.93	88	-

Table 3.4: Summary of the energies and time constants of the experimentally observed states.

So far we focused on the charge dynamics from the perspective of the states with a strong $Fe(3d)$ character. We will now move our attention to the $Fe(CO)_5$ states with a predominant ligand character. We can directly compare these states of $Fe(CO)_5$ with the states of free CO. We find three peaks in the spectrum of CO for binding energies below $20\,eV$, see Figure 3.19 a). They are located at $13.78\,eV$, $16.73\,eV$, and $19.45\,eV$. The intensity maxima are associated with the highest occupied molecular orbitals of CO: the 5σ, the 1π, and the 4σ molecular orbitals, see Figure 3.19 a). These energies deviate less than $0.5\,eV$ from the literature data [13]. In the photoelectron spectrum of $Fe(CO)_5$ there are several peaks with a strong carbonyl character for similar binding energies. Peaks in the range $13\,eV < E_{bin} < 17\,eV$ have a strong contribution from the $CO(5\sigma)$ and $CO(1\pi)$ orbitals. Peaks in the range $17\,eV < E_{bin} < 20\,eV$ have a strong contribution from the $CO(4\sigma)$ orbitals, see Figure 3.19 b) [91, 94, 95]. We can see that photoelectron spectroscopy allows for the observation of the dynamics of the CO separately for the states with 5σ, 1π, and 4σ character. For $Fe(CO)_5$ we can observe the dynamics of the states with a $Fe(3d)$, $CO(5\sigma + 1\pi)$, and $CO(4\sigma)$ character separately. It would be desirable to further discriminate the contribution of the states with a 5σ and a 1π character in the region between $13\,eV$ and $17\,eV$.
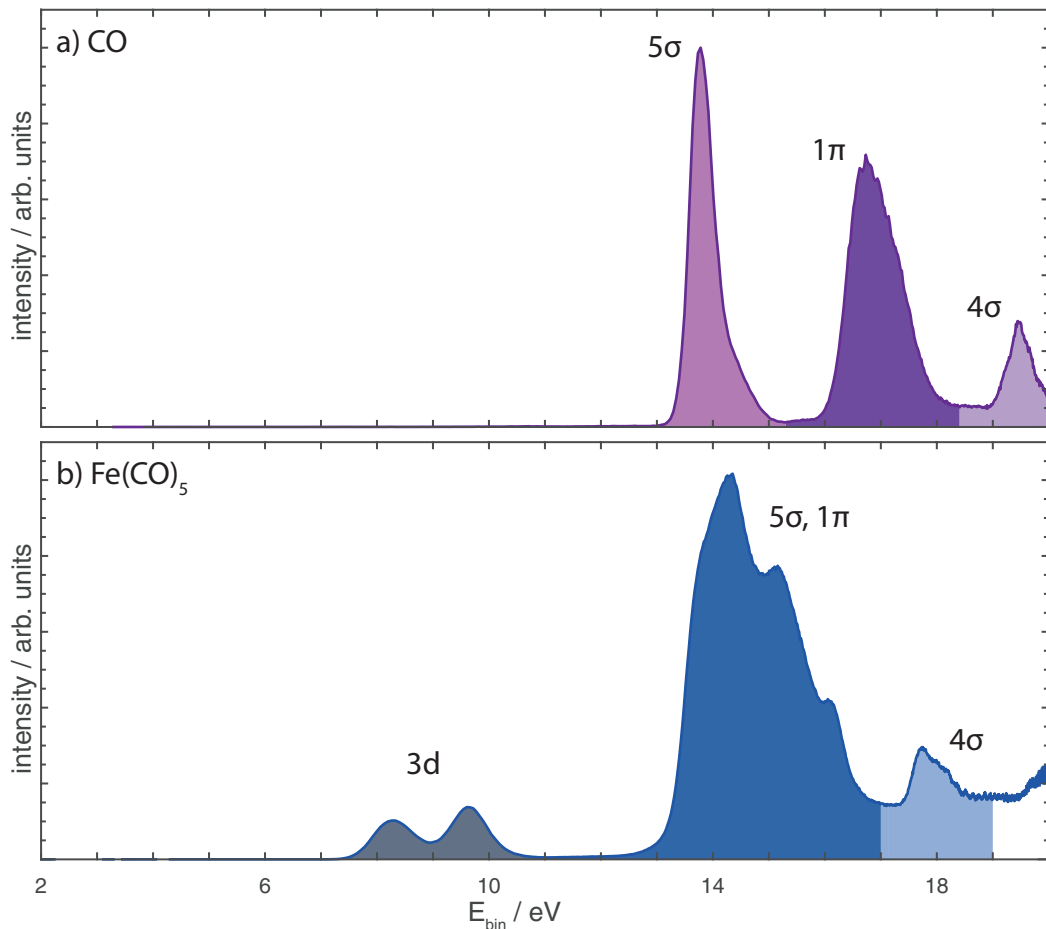
Figure 3.19: A static spectrum of a) CO and b) $Fe(CO)_5$ with peak assignment.

The spectrum is divided according to the changes of the intensity one can identify three regions, b, c, and d. For $11.5\,eV < E_{bin} < 13.5\,eV$ the intensity increases, for $13\,eV < E_{bin} < 17\,eV$ the intensity decrease, and for $17\,eV < E_{bin} < 19\,eV$ the intensity does not change significantly for increasing delays, see Figure 3.20.
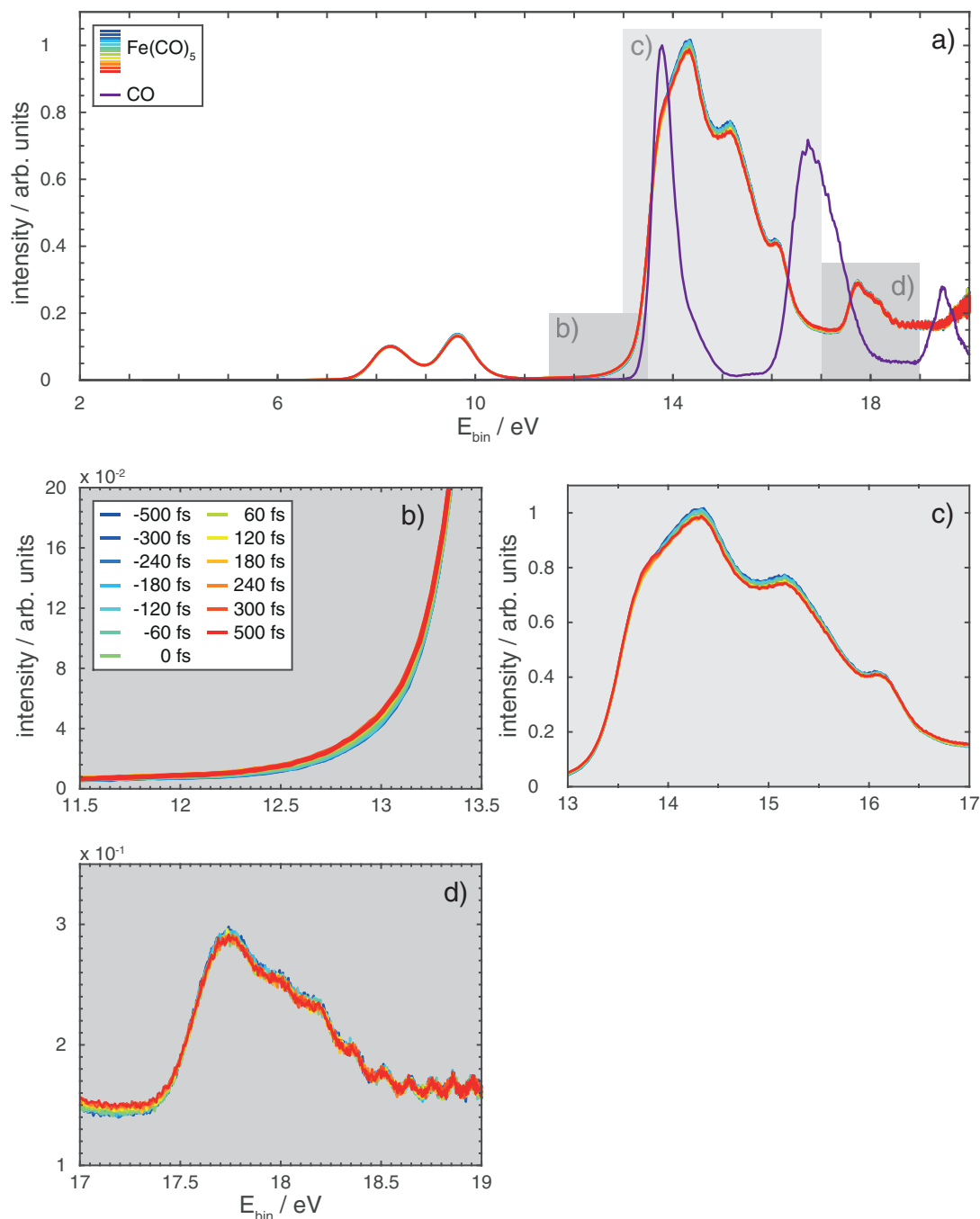
Figure 3.20: Spectra of $Fe(CO)_5$ at different delays.

The difference spectra help to further discriminate these regions. They are calculated by subtracting the spectrum at early delays from the spectra at larger delays. The $Fe(3d)$ lines shift to lower energies ($\Delta E_1 = 0.69\,eV$, $\Delta E_2 = 0.70\,eV$) for increasing delays. At higher energies I have identified seven regions, one to seven, see Figure 3.21 a). The

traces of these regions differ significantly with respect to each other, see Figure 3.22. In region one ($11.5\,eV < E_{bin} < 13.5\,eV$) the intensity rises after t_0. Most likely this rise reflects the formation of $Fe(CO)_4$. The difference between the centers of the $Fe(CO)_5$ and $Fe(CO)_4$ $3d$ lines is about one eV. We can assume that the peaks with ligand character shift by a similar amount. If this is the case then the rise in region one is caused by a shift of the large band ($13\,eV < E_{bin} < 17\,eV$) to lower binding energies. In region two ($13.5\,eV < E_{bin} < 13.9\,eV$) the intensity first decrease and later increases again. It is possible that this is due to energy shifts of multiple peaks or that we see the decrease and increase of multiple species. In the regions three to five ($14.0\,eV < E_{bin} < 16.3\,eV$) and seven ($17.4\,eV < E_{bin} < 19.0\,eV$) the intensity decreases after t_0. The intensity decreases in the range $11\,eV < E_{bin} < 16.5\,eV$. The envelope of the intensity decrease partially resembles the mirrored spectrum of $Fe(CO)_5$, see Figure 3.21. It is likely that we observe the overall decrease of the entire $Fe(CO)_5$ signal and a rise of the CO signal. The rise in region six is most likely an indicator for the formation of free CO. The energy coincides with the energy of the $CO(1\pi)$ peak.

I have fit the traces of all seven regions with an $erfc$ function, see 3.2. The centers are located in the range $-149\,fs < t_0 < 123\,fs$ but show no clear trend.

Can we interpret the data in the framework of the $\sigma - \pi$ backdonation? While one carbonyl dissociates from the complex the overlap between the carbonyl and the iron valence orbitals becomes smaller therefore the backbonding decreases. Electron density flows back from the molecular orbitals with $CO(2\pi^*)$ character to the orbitals with $Fe(3d)$ character. At the same time the orbitals with $Fe(3d)$ character return electron density to the orbitals with $CO(5\sigma)$ character. It is hence difficult to speculate about the dynamics of $Fe(3d)$ band intensity. Within this picture an increased population of the $CO(5\sigma)$ orbital should yield an intensity increase of the peak associated with a state of $CO(5\sigma)$ character, that is a final state with an ionized $CO(5\sigma)$ orbital.

The experimental data do not indicate such dynamics. I find an overall decrease of the intensity for the states with a dominant $CO(5\sigma, 1\pi)$ character with three exceptions. The sharp peak at $E_{bin} = 13.8\,eV$ and the broader peak at $17.0\,eV$ can be attributed to the formation of free CO. The depletion relates to the reduction of $Fe(CO)_5$ in the probing volume. The corresponding $Fe(CO)_4$ states are shifted to lower energies. Shifts in energy can indicate changes in the hybridization. Last but no least, we can discuss the changes of the state with $CO(4\sigma)$ character. The 4σ peak of free CO is located at $19.45\,eV$ which is $1.70\,eV$ above the peak with $CO(4\sigma)$ character in the iron complex. One could expect that during the dissociation the 4σ peak separates into two peaks. One remaining at $17.7\,eV$ and one splitting off and shifting towards $17\,eV$ for increasing delays. This however can not be observed. The changes in intensity with time are small and no shift in energy can be detected.

The observed changes in intensity and energy reflect convoluted dynamics and their interpretation remains speculative. Several ways can be taken in order to improve our understanding of the $\sigma - \pi$ backdonation trough time-resolved photoelectron spectra of $Fe(CO)_5$. The statistics should be improved through longer acquisition times. An angular-resolved measurement increases the sensitivity for the difference between the σ and the π system. The sensitivity is greatest if the light is polarized, the measurement is angular resolved, the molecules are anisotropic, and the molecules
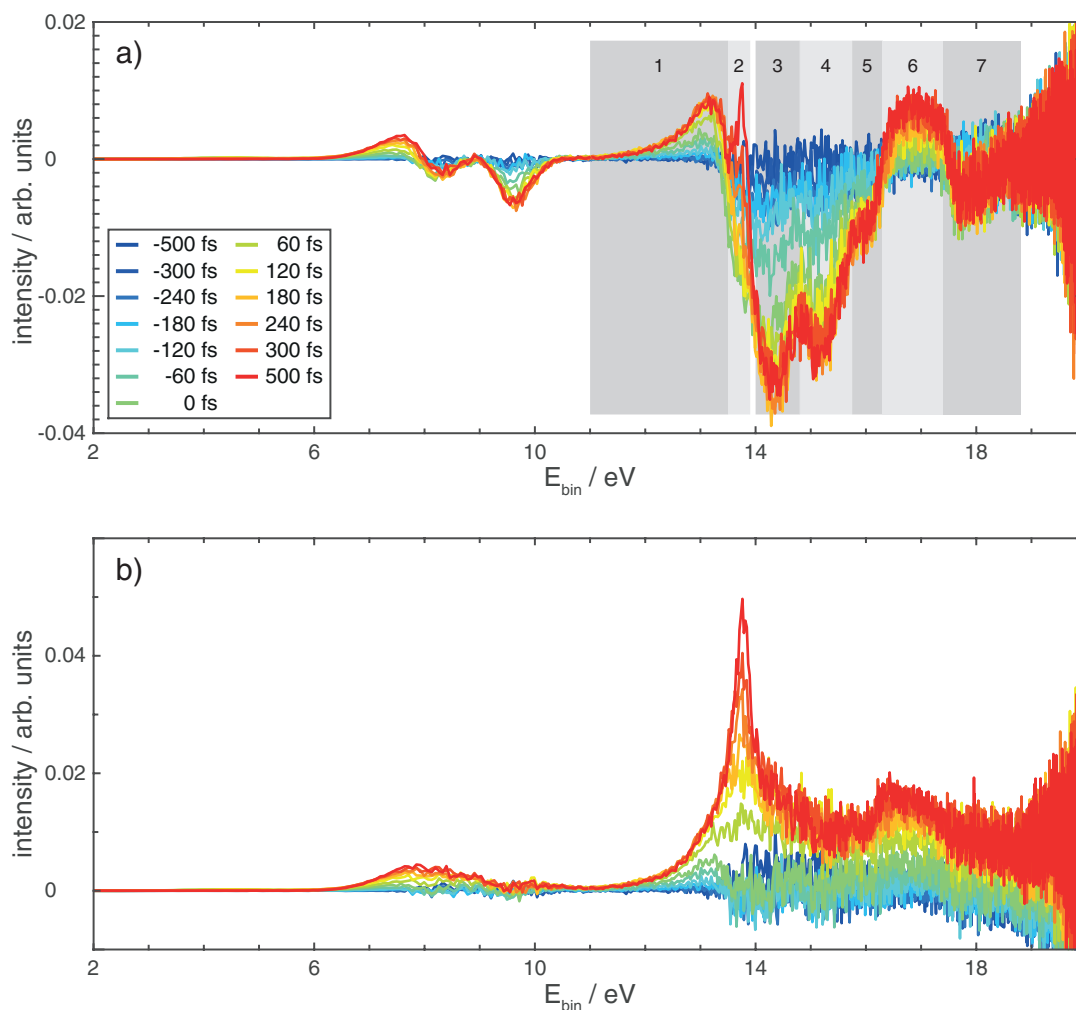
Figure 3.21: Differnce spectra and scaled differences of $Fe(CO)_5$ at various delays.

are aligned. An increase in the energy resolution as well as calculations with a more precise peak assignment and stronger separation of the contributions between σ and π character of the spectroscopic lines will facilitate the interpretation. The results of the photoelectron spectroscopy on $Fe(CO)_5$ are complicated and their interpretation is challenging. We can improve our understanding of the photoelectron spectra of $Fe(CO)_5$ with These calculations should include the ionic final state. As long as the required theory is in development I suggest a systematic study of the photoelectron spectra of various transition metal carbonyls. The mono-nuclear metal carbonyls of group six are a singular target for such a study. $Cr(CO)_6$, $Mo(CO)_6$, and $W(CO)_6$ are of octahedral symmetry. The valence configuration of the metals is similar, see Table 3.5. The photodissociation can be induced in all three hexacarbonyls with $266\,nm$ photons [96]. The ionization energy for the valence orbitals of these metals is also similar. I have measured the ultrafast dynamics of $Cr(CO)_6$ in the gas phase with trPES as a first step in this comparison. The results will be discussed in the next section.
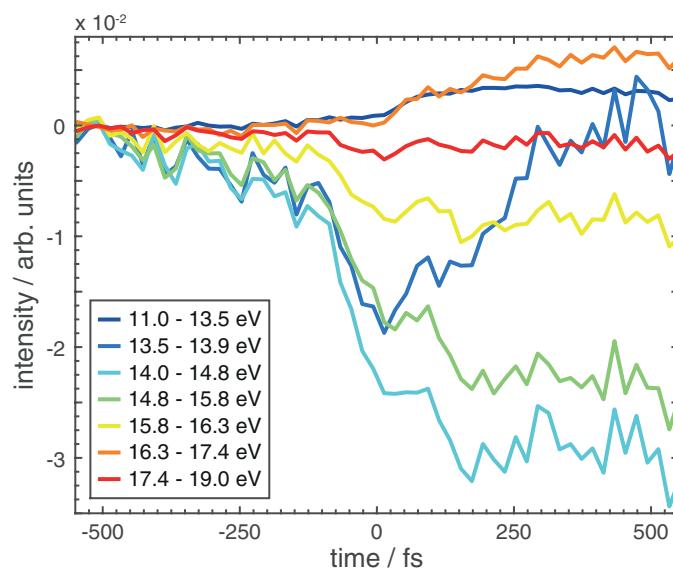
Figure 3.22: Traces of the $Fe(CO)_5$ spectra at selected energies.

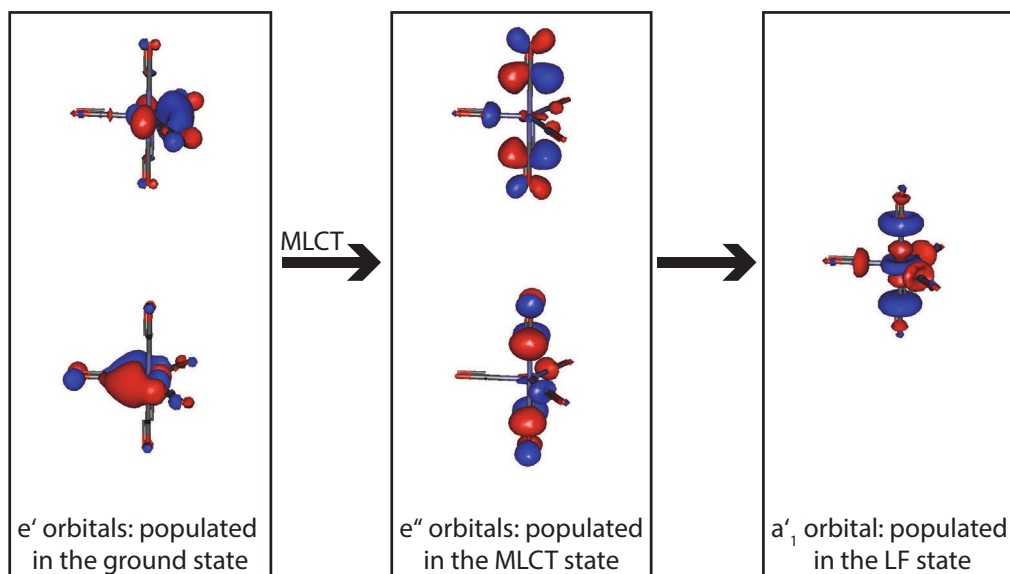| element	electronic configuration
Cr	$[Ar]3d^5 4s^1$
Mo	$[Kr]4d^5 5s^1$
W	$[Xe]4f^{14} 5d^4 6s^2$
Fe	$[Ar]3d^6 4s^2$

Table 3.5: The valence electronic configuration of selected transition metal atoms.

Which ligand leaves the $Fe(CO)_5$ complex first?

The D_{3h} symmetry of $Fe(CO)_5$ leads to two types of ligands, two axial and three horizontal ligands. The electron density of $Fe(CO)_5$ in the ground state was calculated with density functional theory (DFT) including numerical frequencies [P. Midema private communication]. The results give an idea of the orbitals. In the ground state the e' HOMOs are occupied. The electron density is located in the horizontal plane but not on the M-CO bond axes. The excitation via a $266\,nm$ photon causes an MLCT. The e' orbitals depopulate and the e'' orbitals populate. Here the electron density is located further away from the central metal atom on the axial ligands. In the LF state it is the a_1' orbital which is populated. The e'' orbitals are empty. The electron density of the a_1' orbital is located on all M-CO axes with a higher amount of electron density on the axes with the axial ligands.

The depopulation of the e' orbitals clearly weakens the bond to ligands in the horizontal plane. The population of the e'' orbitals strengthens the bond to the axial ligands. But the dissociation does not start in the MLCT state. During the transition to the LF state we populate the anti-bonding a_1' orbital weakening all ligand bonds, the axial bonds slightly more. We also loose the additional strength on the axial orbitals. In this context it would therefore be plausible that an axial ligand dissociates first. To improve this approximation a calculation of the orbitals in the excited state is required.

e' orbitals: populated in the ground state e'' orbitals: populated in the MLCT state a'$_1$ orbital: populated in the LF state

Figure 3.23: Depicted are the selected calculated valence orbitals of $Fe(CO)_5$.

3.3 The Photoinduced Dynamics of Chromium Hexacarbonyl

The UV-vis absorption spectrum of chromium hexacarbonyl ($Cr(CO)_6$) in a solution of ethanol, isopentane, and ethyl ether has been recorded by Wrighton et al., see Figure 3.24, and it was recently discussed by Villaume et al. [97, 98]. The calculations of the UV-vis absorption spectrum indicate that metal centered states and MLCT states can be excited by a $266\,nm$ pulse [99].
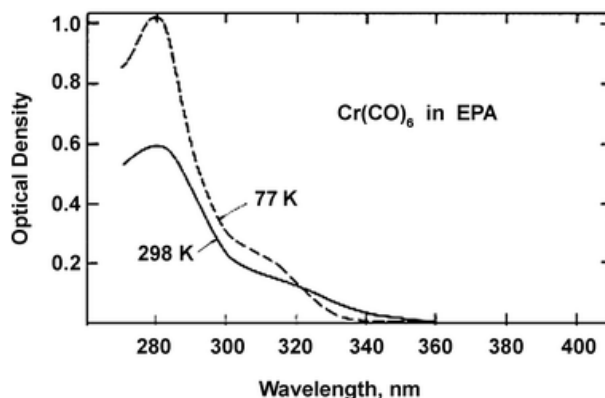

**Figure 3.24:** The UV-Vis spectrum of $Cr(CO)_6$ [97]

The static photoelectron spectrum has been recorded by Higginson et al. and Nilsson et al. [100, 101]. The peaks in the spectrum have been assigned based on calculations. As in the spectrum of $Fe(CO)_5$ there is a peak at $8.53\,eV$ in the spectrum of $Cr(CO)_6$ with a strong metal $3d$ character, the $Cr(3d)$ line. However, there is only one $Cr(3d)$ but two $Fe(3d)$ lines. This is due to the difference in the symmetry of the two complexes. $Cr(CO)_6$ has an octahedral symmetry, $Fe(CO)_5$ has a trigonal bipyramidal symmetry. The difference between the equatorial ligands and the axial ligands in $Fe(CO)_5$ splits the atomic $Fe(3d)$ orbitals in the unoccupied a_1' and the occupied e'' and e' orbitals [95, 102]. e'' and e' are not degenerate. The $3d$ orbitals of the atomic Cr split in the complex to form the unoccupied e_g^* and the occupied t_{2g} orbitals that represent the LUMO and HOMO, respectively. e_g^* and t_{2g} are not further split because all ligands are equivalent in $Cr(CO)_6$.
In the spectrum $Cr(CO)_6$ of Between $11\,eV$ and $20\,eV$ peaks with a ligand character dominate [100, 101, 103].

For my experiments I have used $Cr(CO)_6$ as purchased from Sigma-Aldrich with a $98\,\%$ purity. The solid sample was sublimated at a temperature of $24°C$ into the vacuum chamber. During the experiment chamber pressure was at $p = 5 \cdot 10^{-6}\,mbar$. The sample was pumped with $263\,nm$ femtosecond pulses and probed with $23.25\,eV$ femtosecond pulses. I assume no shift of the temporal overlap t_0 between the two experiments.

I have recorded the excited state dynamics of $Cr(CO)_6$ in the gas phase with time-resolved photoelectron spectroscopy for the first time. The spectrum is shown in Figure 3.25 a) and b). It can be separated into two regions. Region one includes the valence states with a strong $Cr(3d)$ character, region two includes valence states with

a strong ligand character. The peak with the metal character is located at $8.53\,eV$. It has been assigned to a state where the $2t_{2g}$ orbital is ionized [100].

The intensity of the $Cr(3d)$ line decreases for increasing delays. The center of the depletion of peak one is located at $t_0 = -68\,fs$, see Figure 3.25 c). The difference in time to the sideband is similar to the difference found between the $Fe(3d)$ lines and the sideband. As discussed above this discrepancy will not impact the results.
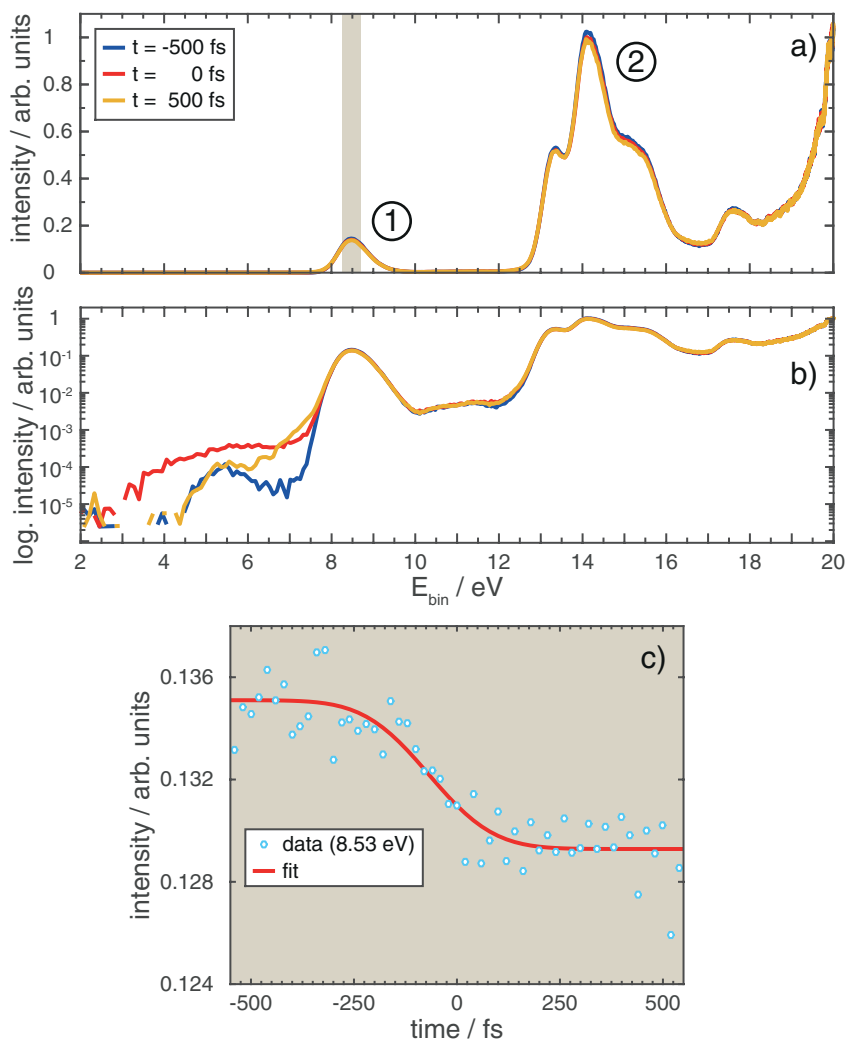
Figure 3.25: The photoelectron spectrum of $Cr(CO)_6$ in a) linear and b) logarithmic representation. c) the trace of peak one at $8.53\,eV$.

The dynamics of the $3d$ line of $Cr(CO)_6$ in the electronically excited state is shown in 3.26. I observe a fast transition of the excited state population to higher binding energies. This is in contrast to $Fe(CO)_5$ where I found a detectable intermediate state at comparable delays, compare Figure 3.26 and 3.27.

I can identify a background signal. It is located at about $5.5\,eV$ and independent of the delay. As in the case of the spectra of $Fe(CO)_5$ I assume that this background derives from a contamination of another harmonic (H13). This other harmonic signal would project the $Cr(3d)$ line onto an a binding energy of $5.44\,eV$.
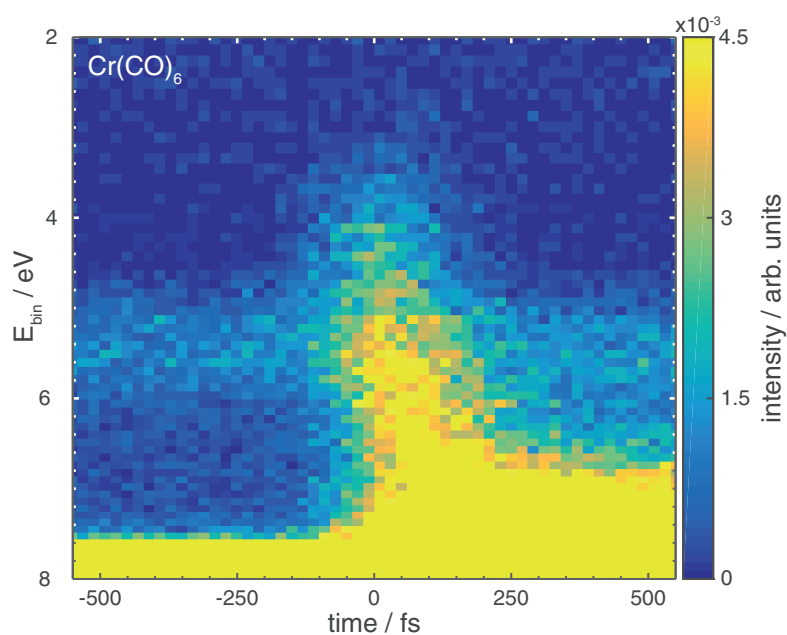
Figure 3.26: Photoelectron spectrum of $Cr(CO)_6$ excited state as function of energy and time
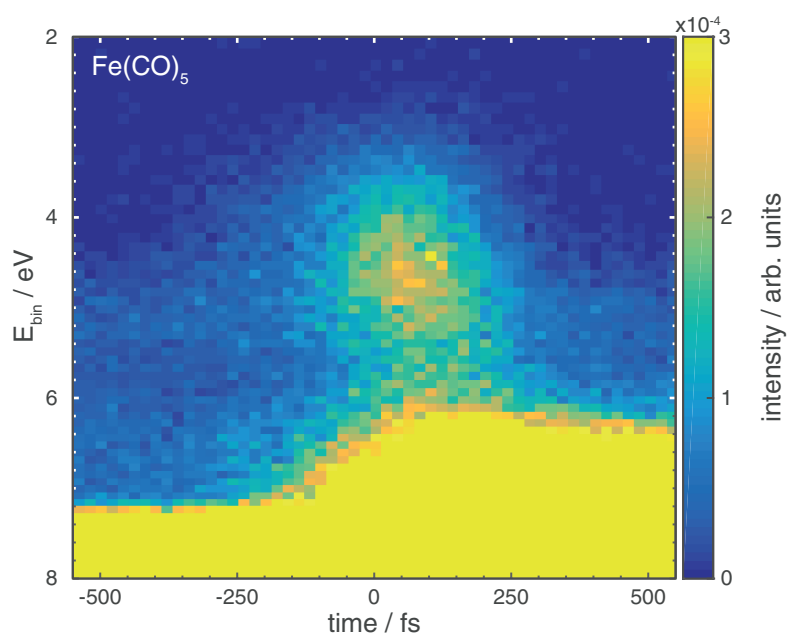
Figure 3.27: Photoelectron spectrum of $Fe(CO)_5$ excited state as function of energy and time

Models for the photodissociation have been proposed by Trushin et al. and Paterson et al. [104, 105]. According to their model the excitation with a $266\,nm$ photon causes the dissociation of the complex on a sub-$100\,fs$ timescale [89, 104]. It is assumed that the light promotes a wave packet to a high MLCT state ($^1T_{1u}$) state from where the wave packet relaxes to a lower MLCT state ($^1T_{2u}$). From this second MLCT state the molecule dissociates one carbonyl group [89, 106]. These early dynamics have been

simulated [105].

Calculations (DFT/MRCI, TDDFT/B3LYP, and MS-CASPT2) agree with the experimental result, the lowest excited state 1^1T_{1u} is located at about $4.44\,eV$. The second lowest excited state, 2^1T_{1u}, is located at $5.48\,eV$ [99].

Crespo-Otero et al. argue that a number of dark states in this energy region can borrow intensity from the T_{1u} state via vibronic coupling [99]. In the photoelectron spectra I can not identify a specific excited stated, see Figure 3.28. The region $2\,eV < E_{bin} < 5.6\,eV$ is populated simultaneously. While states in the region $5.6\,eV \leq E_{bin}$ are populated at increasing delays. The population appears to occur over a broader energy range and less specific than in the iron complex. This is in agreement with the theory of the coupled states.

Traces of the experimental data further support this model, see Figure 3.29. The states in the range $2.0\,eV < E_{bin} < 5.6\,eV$ are populated roughly simultaneously. The lifetime of these states is slightly shorter and the population shifts earlier to higher binding energies relative to the iron complex. The faster dynamics are in agreement with the model proposed by Trushin et al. They claim that the first dissociation step from $Cr(CO)_6$ to $Cr(CO)_5 + CO$ takes $31\,fs$ [89].

We can compare this model with the PE spectra. The intensity as a function of time and energy is shown in Figure 3.29. Similar to the dynamics in $Fe(CO)_5$, excited states are populated quickly after t_0 and decay on the femtosecond timescale. The $Cr(3d)$ line shifts to higher energies for increasing delays. This can be seen by the edge shift. The shift can be quantified with the help of the difference spectra. When comparing positive delays with negative delays the $Cr(3d)$ line at $8.53\,eV$ looses intensity and a second line appears at $7.78\,eV$. This is most likely the $Cr(3d)$ line of $Cr(CO)_5$.
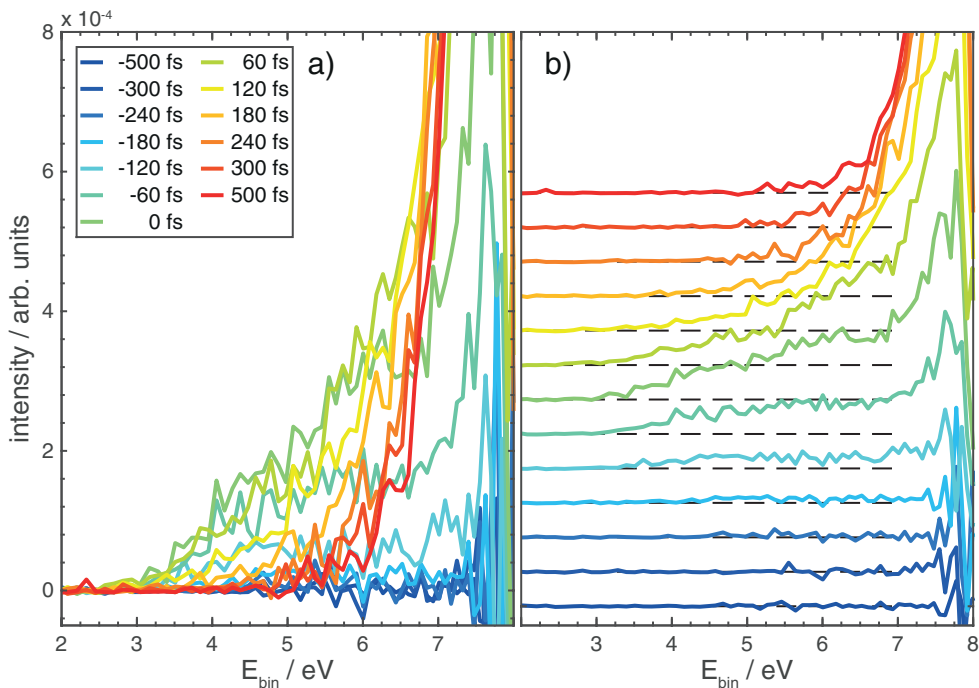
Figure 3.28: Photoelectron spectrum of the $Cr(CO)_6$ excited state region at different delays. The background signal (contamination with another harmonic) was subtracted.
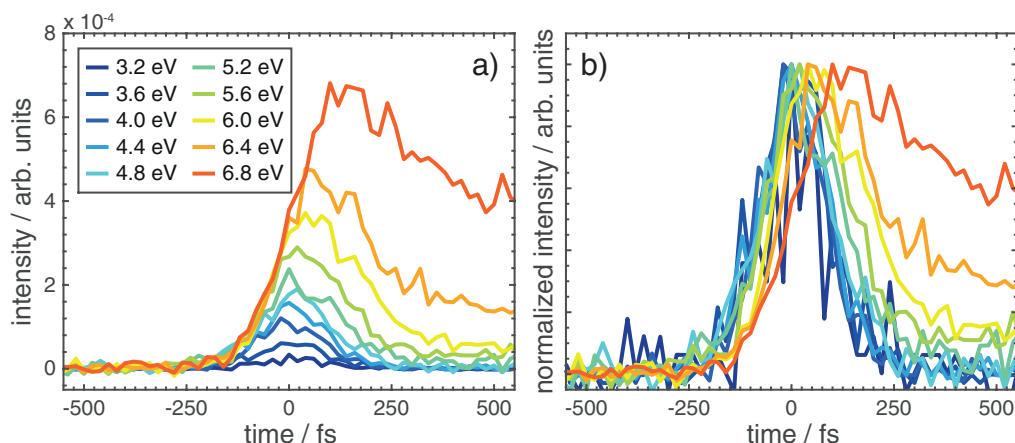
Figure 3.29: Traces of the $Cr(CO)_6$ excited state region at different energies. Non-normalized (a) and normalized (b) intensities.

The PE spectrum of $Cr(CO)_6$ at various delays is shown in Figure 3.30 a). The ligand region of the spectrum is structured similarly to the spectrum of $Fe(CO)_5$. Based calculations these features have been assigned to states. The peaks above $10\,eV$ have a dominant ligand character. The peak at $13.5\,eV$ has been assigned a $CO(5\sigma) + Cr(3d)$ character. The peak at $14.1\,eV$ has a $CO(1\pi)$, the peak around $15.5\,eV$ has a $CO(1\pi)$ character, and the peak at $17.6\,eV$ has a $CO(4\sigma)$ character [101, 107]. The values in my experiments deviate less than $0.3\,eV$ from the literature data.

The difference spectra for the same data are shown in Figure 3.30 b). I can observe a shift of the $Cr(3d)$ line towards a lower binding energy for increasing delays. The shift is $\Delta E = 0.84\,eV$ and hence slightly larger than the shift of the two $Fe(3d)$ lines ($\Delta E = 0.69\,eV$, $\Delta E = 0.70\,eV$). In the ligand region we can observe the same dynamics as in $Fe(CO)_5$. There is an overall intensity decrease indicating the reduction of $Cr(CO)_6$. Intensity rises in three energy regions. The rise at $E_{bin} = 12.5\,eV$ is most likely linked to the rise of the $Cr(CO)_5$ spectrum at lower energies. The rise at $13.8\,eV$ and $16.8\,eV$ derives from the formation of free CO.

The overall dynamics in the $Cr(CO)_6$ spectrum are similar to the ones observed in $Fe(CO)_5$. A direct comparison of the excited state dynamics permits me to state that the population of the first excited state and the following relaxation occur on the same timescale as the dynamics in $Fe(CO)_5$. Most likely the progression is faster in the Cr complex. This point will be examined in the future with an in-depth analysis of the photoelectron spectra of $Cr(CO)_6$. The first impression of a fast decay time, compared to $Fe(CO)_5$, is in agreement with literature data [104, 105, 108].
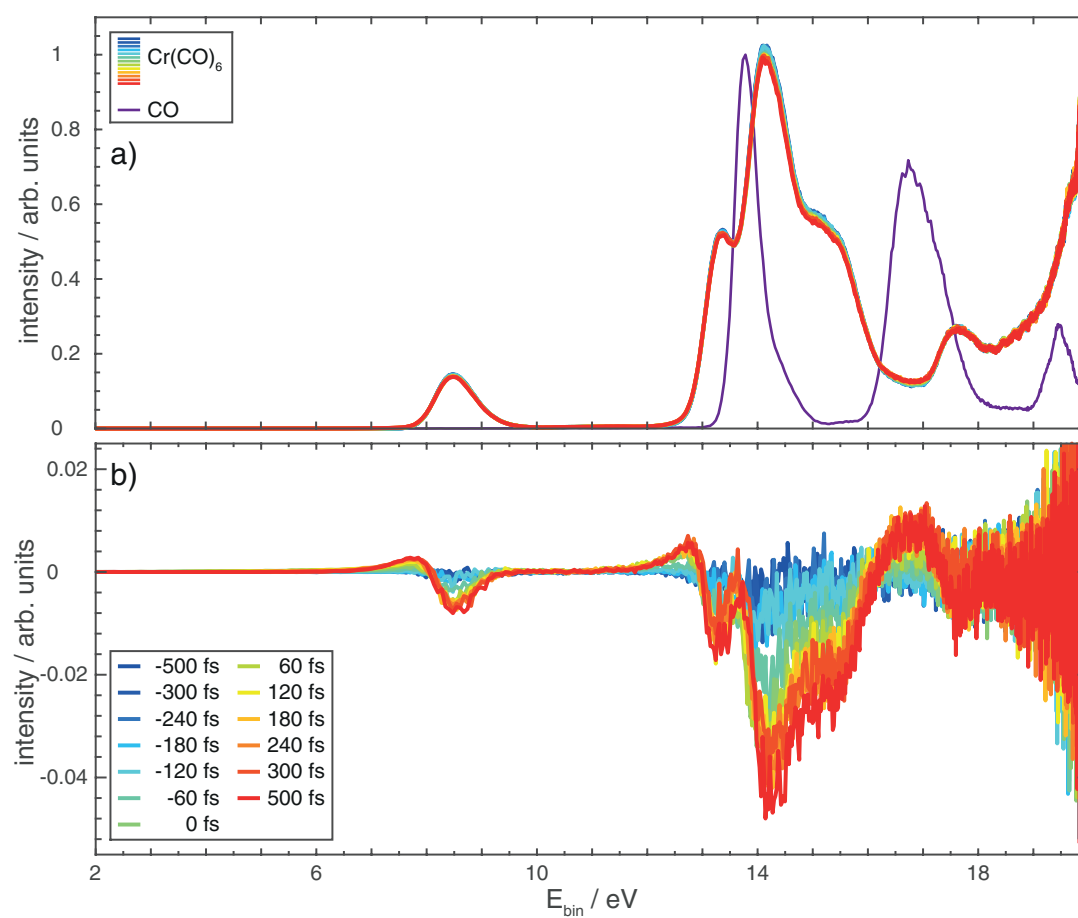
Figure 3.30: Photoelectron spectrum of $Cr(CO)_6$ excited at different delays and the photoelectron spectrum of CO.

3.4 The Differences of the Electronic Dynamics Coupled to Nuclear Motion

In the past, many reactions have been successfully modeled in the Born-Oppenheimer approximation. The approximation assumes that the motion of the electrons can be separated from the motion of the nuclei. For ultrafast reactions this approximation can break down. In order to know, whether the approximation is valid in a specific reaction both the dynamics of the electrons and the dynamics of the atomic nuclei should be measured and compared. Experimental data for the nuclear dynamics of $Fe(CO)_5$ or $Cr(CO)_6$ on the femtosecond timescale are not available yet. In the models for the photodissociation of both $Fe(CO)_5$ and $Cr(CO)_6$ the electronic dynamics are coupled to the nuclear dynamics. Let us investigate if we can interpret the PES results, and specifically the differences between the spectra of the two complexes, in agreement with the model.

The PE spectra covering the photodissociation of $Fe(CO)_5$ and $Cr(CO)_6$ are shown in Figure 3.31 a) and b). In the spectrum of $Fe(CO)_5$ the excitation leads to a detectable intermediate. A peak is located at about $4.6\,eV$ and $50\,fs$. The intensity decreases towards higher energy and larger delays with a minimum in energy at about $5.5\,eV$. At even higher energies $7.4\,eV$ and larger delays the intensity increases again towards $7.4\,eV$.

The PE spectra of $Cr(CO)_6$ are different. At a delay around $0\,fs$, the intensity increases over the energy range between $4.0\,eV$ and $5.0\,eV$. In contrast to $Fe(CO)_5$, there is not a single peak, but rather a band. For larger delays, the intensity shifts towards higher energies. At delays of $500\,fs$, the low energy flank is located at about $7.4\,eV$. The spectra are shown again in Figure 3.31 c) and d), but here the intensities are normalized to one along each energy channel. We can see that the detectable initial state of $Fe(CO)_5^*$ starts at lower energies with respect to the peak found in the spectra of $Cr(CO)_6^*$ at the same delays. The $Fe(CO)_5^*$ peak slides to larger energies for an increasing delay. In $Cr(CO)_6$, the transition of the peak from lower to higher energies for increasing delays occurs faster.

I have interpreted the spectra of $Fe(CO)_5$ on the basis of the discussion around the UV-vis spectrum of $Fe(CO)_5$ and the model for the excited state dynamics proposed by Trushin et al. [9]. This model is summarized in Figure 3.32 a). It consists of five time constants $\tau_{1,...,5}$. The first three time constants are relevant for the dynamics of $Fe(CO)_5$, while the last two are relevant for the dynamics of $Fe(CO)_4$. The pump pulse excites the molecule into the $2^1E'$ MLCT state. The depicted reaction coordinate $q(e')$ is very likely the bond distance $Fe-C$ or $C-O$. Along this coordinate, the degeneracy of each of the $2^1E'$ state and $1^1E'$ LF state is lifted. The wave packet can transition from the $2^1E'$ to the $1^1A_2''$ MLCT state and back or move directly along the $2^1E'$ potential. Both $2^1E'$ and $1^1A_2''$ are only weakly repulsive [9]. The transition from the $2^1E'$ to the $1^1E'$ state is associated with the first time constant $\tau_1 = 21\,fs$ [9]. The wave packet moves faster on a steeper curve, therefor the reaction speed can depend on this slope. The $1^1E'$ state has a steeper potential energy curve than the $2^1E'$ state. I believe that the peak at $4.6\,eV$, Figure 3.31 a) reflects the dynamic on the $2^1E'$ state potential energy curve. In $Fe(CO)_5$, the reaction occurs mainly along the two potential curves of the $2^1E'$ and $1^1E'$ state. Along this path, $q(e')$ increases
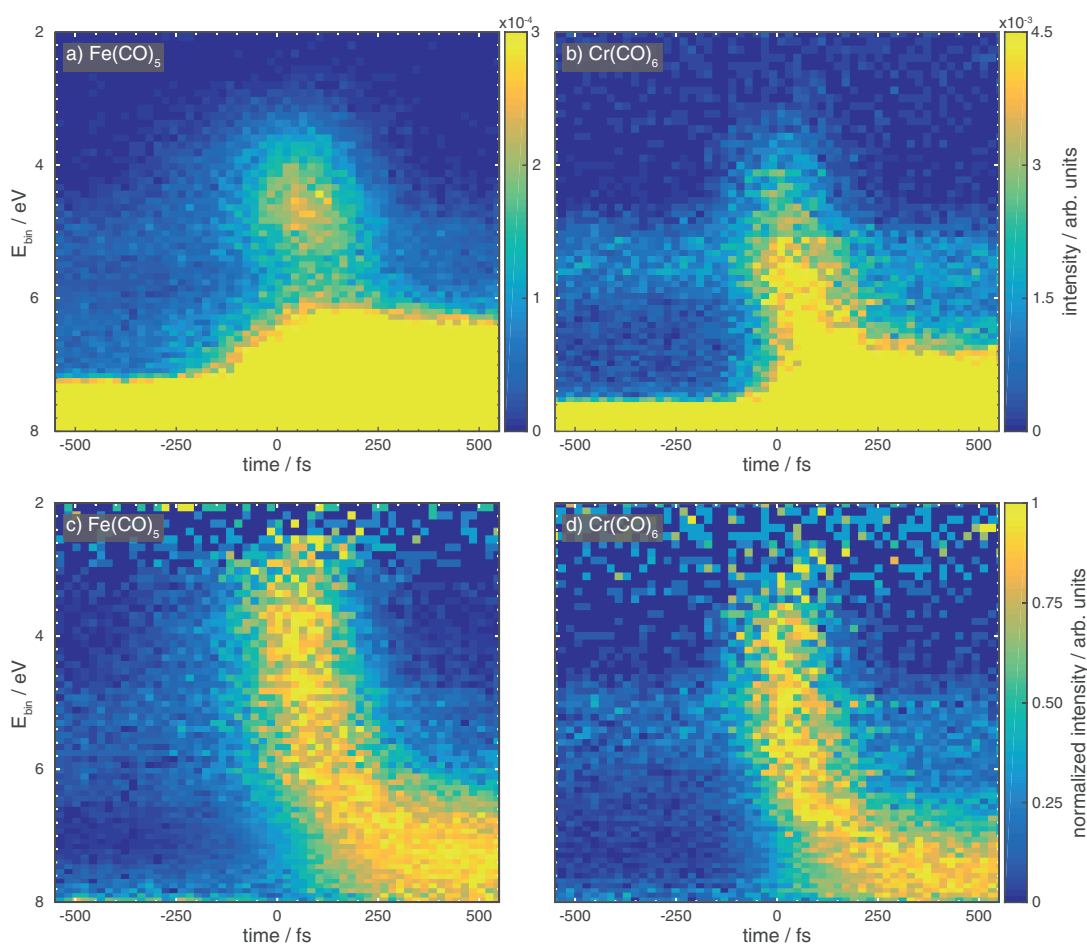
Figure 3.31: Time-resolved PE spectra of $Fe(CO)_5$ and $Cr(CO)_6$ during the photodissociation. The data of $Fe(CO)_5$ [a) and c)] are the same is in Figure 3.9 and 3.14. The data of $Cr(CO)_6$ [b)] are the same is in Figure 3.26.
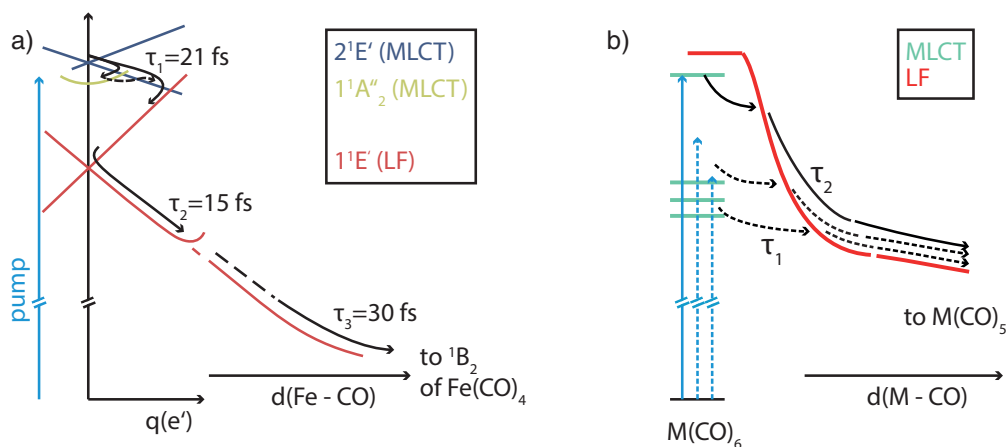

Figure 3.32: An illustration of the movement of the wave packet along the potential energy curves in a) $Fe(CO)_5$ and b) $M(CO)_6$. In b), the solid lines indicate the pathway after an excitation with $270\,nm$. The dashed lines indicate the pathway after an excitation with $318\,nm$ and $345\,nm$ as discussed in the text. a) is a detail of Figure 3.7. (Adapted from [9] and [89])

between these two states above the crossing, whereas it decrease below the crossing. From a mechanistic perspective, it takes time to slow the stretch motion down and reverse the direction. The movement on the $1^1E'$ curve along the $q(e')$ coordinate is associated with the second time constant $\tau_2 = 15\,fs$, while the movement along the $d(Fe-CO)$ coordinate is associated with the third time constant $\tau_3 = 30\,fs$.

The $^1B_2\ Fe(CO)_4^*$ state is reached only after the third time constant. From the $^1B_2$ state, the wave packet transitions to $^1A_1$ the lowest singlet state of $Fe(CO)_4$. The transition is associated with the time constant τ_4. $Fe(CO)_4$ in the $^1A_1$ state dissociates into $Fe(CO)_3 + CO$. τ_5 is the time constant of this dissociation.

The absorption of a single $266\,nm$ photon causes in both the iron and chromium complex the population of an MLCT states with an ungerade ('u') symmetry. A transition from the ground state to a pure LF state with a gerade ('g') symmetry is symmetry forbidden. Due to the mixing of the states, the transition can still occur, but it carries a low oscillator strength [98, 108]. These transition have been assigned to absorption maxima in the UV-vis spectrum of $Cr(CO)_6$, see Figure 3.33.
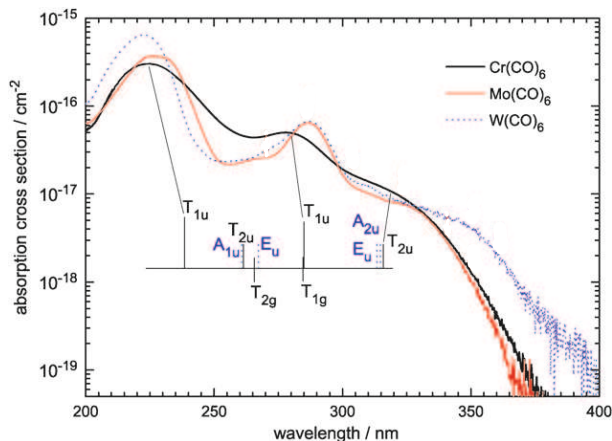
Figure 3.33: Gas-phase UV-vis absorption spectra for the metal hexacarbonyls $M(CO)_6$ ($M = Cr, Mo, W$). (Adapted from [108])

These MLCT states are not strongly dissociative states. The LF state, on the other hand, is a dissociative state, but is not primarily populated with the pump pulse [9, 108]. It is therefore expected that the wave packet crosses from the MLCT state to a particular LF state, it is only then that the molecule dissociates.

According to Kosma et al. in $Cr(CO)_6$, this LF state is higher in energy than the MLCT states in the ground state geometry. With increasing $Cr-CO$ distance, the LF decreases strongly in energy [108]. This is illustrated in Figure 3.32 b). The population of the MLCT state(s) can transition over to the LF potential energy curve. In the hexacarbonyls, the progression of the reaction does not require a reversion of the reaction coordinate which could explain why a single electronically excited intermediate state can note be detected in the spectra. The transition from the MLCT states to the LF state and the change in energy of the LF state occur too quickly.

In the spectra of $Fe(CO)_5$, I could detect at least one intermediate state which is localized in energy. I have observed the population of the MLCT state during the early excited state dynamics of $Fe(CO)_5$. With the resolution in my experiment, it is not

possible to discriminate whether, after this initial excitation, only one MLCT state or two MLCT states close in energy ($4.50\,eV$, $4.71\,eV$) are involved. My findings are in agreement with the Trushin model.

in the spectra of $Cr(CO)_6^*$, I could not detect an intermediate state which is localized in energy. The swift shift of the intensites in the spectra of both $Fe(CO)_5$ and $Cr(CO)_6$ likely reflects the movement of the wave packet along the LF potential. A similar observation can be made in calculated photoemission spectra of Br_2. The spectra are shown in Figure 3.34. At a delay of $0\,fs$, the intensities can be assigned to molecular orbitals. During the photodissociation, these orbitals change their character, their energy, and transform into atomic orbitals [109]. I have discussed such a continuous change in the energy of a state, see Figure 2.2 c) section 2.1.

Whether the population of a specific state can be detected depends on the resolution of the experiment and on the velocity of the reaction. The difference in velocity of the photodissociation in $Fe(CO)_5$ and $Cr(CO)_6$ can be partly explained as result of the coupling of the electronic dynamics to the nuclear motion. During the dissociation of $Fe(CO)_5$ the direction of the nuclear motion has to change twice. The first turning point is located at the conical intersection which connects the MLCT curve and the LF curve, the second turning point is located at the ground state geometry where the LF potential curve is degenerate. However, no change in direction is required during dissociation of $Cr(CO)_6$.
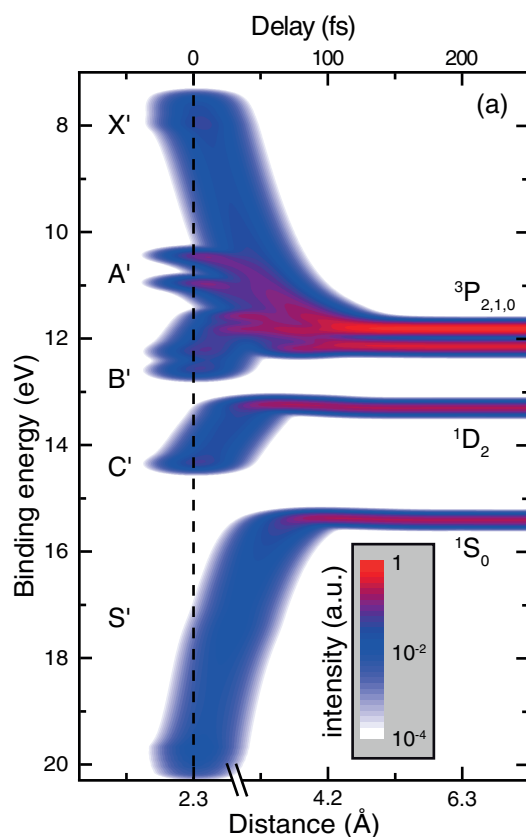
Figure 3.34: The calculated photoelectron spectra of Br_2 during the photodissociation. (The figure is adapted from [109])

Let us now compare the steps after the dissociation for $Fe(CO)_5$ and $Cr(CO)_6$. In the PE spectra of $Fe(CO)_5$, I have identified the intermediate state $^1B_2$ of $Fe(CO)_4^*$. This state is reached $(43 \pm 8)\,fs$ after the initial population of the first MLCT state. The time is consistent with the $(66 \pm 5)\,fs$ proposed by Trushin. However, it would also be consistent with a second scenario. If the initial MLCT state would be dissociative, then the duration of the path to the $^1B_2$ state is determined by the first two time constants of the Trushin model. The $^1B_2$ state should then be reached after $36\,fs$. This scenario is unlikely because the MLCT states are only slightly repulsive, and the slopes of the LF potentials are much steeper. A dissociation path only along an MLCT potential energy curve should therefore be slower.

In earlier studies of $M(CO)_6$ ($M = Cr, Mo, W$), Trushin et al. assumed that the initial population of the T_{1u} MLCT state first relaxes to a lower MLCT state T_{2u} before it crosses over to the dissociative LF state $^1T_{1g}$. The two time constants τ_1 and τ_2 were associated with the relaxation from $^1T_{1u}$ to $^1T_{2u}$, and $^1T_{2u}$ to $^1T_{1g}$, respectively. $Cr(CO)_6$ dissociates with a lifetime equal to the sum of the first three time constants $\tau_{d,old} = \tau_{1,old} + \tau_{2,old} + \tau_{3,old} = 53\,fs$, see table 3.6 [96]. With an improved time-resolution and a variable pump wavelength, Trushin et al. were able to acquire new experimental data for the purpose of revising their model for the relaxation pathway in $Cr(CO)_6$. They found an even shorter first time constant of $\tau_{1,new} = 12.5\,fs$, as opposed to the old $\tau_{1,old} = 23\,fs$, and they suggested the existence of an even faster pathway directly from $^1T_{1u}$ to the LF state, see Tabel 3.6 [89]. The faster direct path outcompetes the longer path across the second MLCT state, see Figure 3.35. The short relaxation time indicates that the two potential energy curves are connected via a crossing or an avoided crossing [89].

	$\tau_{1,old}/fs$	$\tau_{2,old}/fs$	$\tau_{3,old}/fs$	$\tau_{d,old}/fs$
$Cr(CO)_6$	23 ± 1	10 ± 1	20 ± 2	53 ± 2

	$\tau_{1,new}/fs$	$\tau_{2,new}/fs$		$\tau_{d,new}/fs$
$Cr(CO)_6$	12.5 ± 0.5	18 ± 2		31 ± 2

	τ_1/fs	τ_2/fs	τ_3/fs	τ_d/fs
$Mo(CO)_6$	30 ± 1	20 ± 2	35 ± 2	85 ± 2
$W(CO)_6$	46 ± 1	23 ± 2	30 ± 2	99 ± 2
$Fe(CO)_5$	21 ± 2	15 ± 5	30 ± 3	66 ± 6

Table 3.6: Time constants for the dissociation dynamics of hexacarbonlys and iron pentacarbonyl [9, 89, 96].

In fact, if the excitation is performed at different wavelengths i.e., $162\,nm - 282\,nm$, different MLCT states are populated initially, but the relaxation to a LF state occurs in all cases. To be exact, the relaxation paths lie on the same potential energy surface (LF), but meet only in the excited product state S_1 of $Cr(CO)_5$. The decay of the LF state is now associated with the second time constant. The path towards the dissociation is now modeled as follows: the pump pulse excites the wave packet from the ground state into one of the MLCT states. During the vibration of the $M-CO$ bond the population of the MLCT state transitions to the LF curve via a crossing or

an avoided crossing, see Figure 3.35. From here, the complex dissociates. The lifetime of $Cr(CO)_6$ $\tau_{d,new}$ after the excitation with a $270\,nm$ pulse is now equal to the sum of the first two time constants $\tau_{d,new} = \tau_{1,new} + \tau_{2,new} = 31\,fs$.

$$\text{M(CO)}_6 \xrightarrow{\tau_{d,new}} \text{M(CO)}_5 + \text{CO}$$
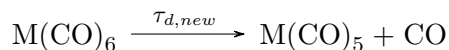
The thorough analysis of the $Cr(CO)_6$ PE spectra will allow for the identification of the $Cr(CO)_5$ state and, thereby, the check for $\tau_{d,new}$.
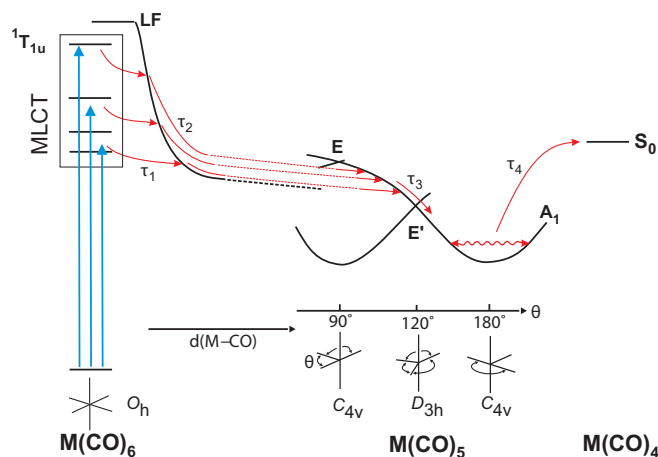
Figure 3.35: Movement of the wave packet along the potential energy curves in $Cr(CO)_6$ for different pump wavelengths [89].

We have seen fundamental differences of the dissociation pathways in $Fe(CO)_5$ and $Cr(CO)_6$. The starting point of the pathways depends on the energy of the unoccupied orbitals. A specific orbital can be selected via the photon energy of the pump pulse. The route of the wave packet occurs along the potential energy curves of the different states. The wave packet can cross from one curve to another curve radiationless where there are crossings. The slope of the curves as a function of the reaction coordinate and hence the location of the crossings is influenced by the type of ligand. From these aspects, we understand that the pathways depends on properties of the complex in the ground state. However, predicting the potential energy curves and the course along these curves remains a challenge. With this work, I can confirm the existing model of the photodissociation in $Fe(CO)_5$. By confirming this model, we have taken another step towards the goal to understand the dynamics of two prototype catalysts.

Chapter 4

Summary and Outlook

This thesis is composed of two topics. The first topic covers a setup for pump-probe photoelectron spectroscopy based on high harmonic generation. The second topic covers the application of this setup to study the molecular dynamics of $Fe(CO)_5$ and $Cr(CO)_6$.

I have moved an existing high harmonic setup to a new laboratory, improved it, and characterized it extensively. A laser delivers $1.7\,\mu J$ pulses at a center wavelength of $800\,nm$ at a rate of $3\,kHz$. The pulses are split, for a pump-probe scheme. The photon energy of the pump pulses can be increased via second and third harmonic generation in a BBO. The energy of the probe beam is increased via high harmonic generation in a gas cell. If the cell is filled with argon, photon energies of $38.75\,eV$ can be reached. A higher photon flux of up to $10^{11}\,ph/s$ can be generated with xenon, however the photon energy is limited to $29.45\,eV$. A specific energy can be selected with a grating monochromator.

Photon energies of $E_{H01} = 1.58\,eV$, $E_{H02} = 3.15\,eV$, $E_{H03} = 4.71\,eV$ are now available for pumping samples, thereby extending the existing setup. The pump pulse energies are $P_{pulse}(H01) = 360\,\mu J$ and $P_{pulse}(H03) = 6\,\mu J$. For probing, photon energies from $E_{H11} = 17.05\,eV$ to $E_{H25} = 38.75\,eV$ are available. The pulse duration of the higher harmonic is as short as $98\,fs$. The temporal resolution for experiments with a $H01$ pump and $H15$ probe is $111\,fs$. For a combination of the $H03$ pump and $H15$ probe, a resolution of $262\,fs$ has been measured.

With this setup, I have studied the sub-picosecond excited state dynamics of $Fe(CO)_5$ and $Cr(CO)_6$. For the first time, the intermediate electronically excited states of $Fe(CO)_5$ and $Fe(CO)_4$ in the gas phase were directly observed with time-resolved photoelectron spectroscopy. This demonstrates that the setup is well suited to probe chemical dynamics on the femtosecond timescale.

For $Fe(CO)_5$, I have detected intermediate states during the photodissociation. I have measured the occurrence in time with respect to the pump signal, the energy, and, in some cases, the decay time for intermediate MLCT states of $Fe(CO)_5$, as well as for the singlet excited state, and the lowest singlet state of $Fe(CO)_4$.
The peaks associated with the excited states of $Fe(CO)_5$ are located at $40\,fs$ and $61\,fs$ with respect to the temporal overlap established with the sidebands. The decay

time of these two states is $< 10\,fs$, and hence, below the detection limit. If only one MLCT state is assumed, then this stated would be located at $49\,fs$. A state that could be associated with the LF state is not observed. The electronically excited $^1B_2$ state of $Fe(CO)_4^*$ and the $^1A_1$ state of $Fe(CO)_4$ have been observed. They are located at $83\,fs$ and $88\,fs$ with respect to the sideband center. The decay of the $^1B_2$ state is also $< 10\,fs$. These results of the states with a strong metal character are conclusive and confirm the model for the photodissociation by Trushin et al. [9]. The results of the states with a ligand character were so far inconclusive. They require a refined model to further separate the contribution from the σ-type and π-type ligand states. A future improvement of time and energy resolution as well as a longer data-acquisition will improve the quality of the spectra. The higher quality might allow the distinction between a dissociation scenario of $Fe(CO)_5$ with one or two MLCT states.

In the spectra of $Cr(CO)_6$ I could not detect intermediate states localized in energy and time as is the case in the spectra of $Fe(CO)_5$. Possibly several states are initially populated simultaneously. The peak associated with the excited state(s) slides towards higher energies for increasing delays. This progression appears faster than in the spectra of $Fe(CO)_5$. The analysis of the $Cr(CO)_6$ spectra is still in progress.

According to Trushin et al., the pathway for the photodissociation is similar for the two complexes in the sense that a $266\,nm$ photon causes an excitation from the ground state to an MLCT state [89]. From the MLCT state, the molecule transitions to a dissociative LF state. According to Trushin, this reaction is faster in $Cr(CO)_6$ [9, 89]. The times observed in my spectra largely confirm the time constants in the Trushin model for the reaction of $Fe(CO)_5$.

The experiments covered in this thesis present a valuable contribution to the ongoing discussion of the excited state dynamics of metal carbonyls. I have discussed how we can improve our understanding of the spectra with the help of calculations which include the final ionic state.

The photoelectron spectra in this thesis are limited in energy range by the photon energy of the HHG. The valence states are particularly sensitive to the bonding. The core states, on the other hand, are less sensitive to the bonding, but offer an element selective perspective. The photodissociation dynamics can be probed at the metal, carbon, and oxygen atoms separately. Such experiments would complement the valence spectra. The short pulse length and high photon energies can be reached at free electron laser such as the free-electron-laser in Hamburg (FLASH).

It would also be interesting to complement the excited state dynamics of $Fe(CO)_5$ and $Cr(CO)_6$ with additional systems. These could include $Mo(CO)_6$, $W(CO)_6$, and $Ni(CO)_4$. Although the pathway in the hexacarbonyls $Mo(CO)_6$ and $W(CO)_6$ is as direct as in $Cr(CO)_6$, the reaction is slower than in $Fe(CO)_5$ [96]. The time-resolved PE spectra of the valence region will allow for the identification of whether or not stationary intermediate states are involved. In $Ni(CO)_4$, no direct direct dissociative pathway exists from the electronically excited $Ni(CO)_4^*$ to the product $Ni(CO)_3$. The intermediate $Ni(CO)_4^*$ can only decay via fluorescence. This process is orders of magnitude slower than the radiationless decay. The metal carbonyls $Mo(CO)_6$ and $W(CO)_6$ are currently being investigated in our group by my successor.

List of Publications

Publications

I **A High Harmonic Setup for Probing Chemical Dynamics on the Femtosecond Timescale**
H. Schröder; R. Jay; R. Mitzner; C. Weniger; Ph. Wernet; A. Föhlisch
in manuscript

II **Mapping ligand coordination, spin and electron density changes in $Fe(CO)_5$ dissociation with x-ray laser spectroscopy**
Ph. Wernet, T. Leitner, I. Josesfsson, T. Mazza, H. Schröder, M. Beye, K. Kunnus, S. Schreck, P. Radcliffe, S. Düsterer, M. Meyer, M. Odelius, A. Föhlisch
in manuscript

III **Mapping chemical interactions in real-time: Femtosecond photoelectron spectroscopy reveals the valence electron rearrangements during Br2 dissociation**
Ph. Wernet, J. Gaudin, K. Godehusen, O. Schwarzkopf, H. Schröder, M. Odelius, W. Eberhardt
in manuscript

IV **Viewing the Valence Electronic Structure of Ferric and Ferrous Hexacyanide in Solution from the Fe and Cyanide Perspectives**
K. Kunnus, W. Zhang, M. G. Delcey, R. V. Pinjari, P. Miedema, S. Schreck, W. Quevedo, H. Schröder, A. Föhlisch, K. Gaffney, M. Lundberg, M. Odelius, Ph. Wernet
The Journal of Physical Chemistry B 120 (29): 7182-7194 (2016)

V **L-Edge X-Ray Absorption Spectroscopy of Dilute Systems Relevant to Metalloproteins Using an X-Ray Free-Electron Laser.**
R. Mitzner, J. Rehanek, J. Kern, S. Gul, J. Hattne, T. Taguchi, R. Alonso-Mori,R. Tran, C. Weniger, H. Schröder, W. Quevedo, H. Laksmono, R. G. Sierra, G. Han, B. Lassalle-Kaiser, S. Koroidov, K. Kubicek, S. Schreck, K. Kunnus, M. Brzhezinskaya, A. Firsov, M. P. Minitti, J. J. Turner, S. Moeller, N. K. Sauter, M. J. Bogan, D. Nordlund, W. F. Schlotter, J. Messinger, A. Borovik, S. Techert, F. M. F. de Groot, A. Föhlisch, A. Erko, U. Bergmann, V. K. Yachandra, Ph. Wernet, J. Yano
The Journal of Physical Chemistry Letters 4 (21): 3641-3647 (2013)

VI   **Experimental and Computational X-Ray Emission Spectroscopy as a Direct Probe of Protonation States in Oxo-Bridged Mn IV Dimers Relevant to Redox-Active Metalloproteins.**
B. Lassalle-Kaiser, T. T. Boron, V. Krewald, J. Kern, M. A. Beckwith, M. U. Delgado-Jaime, H. Schroeder, R. Alonso-Mori, D. Nordlund, T-C. Weng, D. Sokaras, F. Neese, B. Bergmann, V. K. Yachandra, S. DeBeer, V. L. Pecoraro, J. Yano
Inorganic Chemistry 52 (22): 12915-12922 (2013)

VII   **Electronic Structural Changes of Mn in the Oxygen-Evolving Complex of Photosystem II during the Catalytic Cycle**
P. Glatzel, H. Schroeder, Y. Pushkar, T. T. Boron, S. Mukherjee, G. Christou, V. L. Pecoraro, J. Messinger, V. K. Yachandra, U. Bergmann, J. Yano
Inorganic Chemistry 52 (10): 5642-5644 (2013)

Acknowledgments

I would like to thank all those who have supported this work. So many of my colleagues and friends helped me in the time of need. They discussed the experiments and the results and with me, they inspired, and thought me.

I am grateful for the guidance and the freedom which my two supervisors Alexander Föhlisch and Philippe Wernet gave me. The discussions with you helped me to master the daily challenges in the laboratory.

The work presented in this thesis is a team effort and would not have been possible without the help of my colleges. A special thanks goes to Rolf Mitzner and Christian Weniger for keeping the laser lasing and Raphael Jay who spend countless hours in the lab with me preparing and measuring the metal carbonyls. It was a lot of fun to share the experiments at X-ray sources with my colleagues Simon Schreck, Kristjan Kunnus, Wilson Quevedo, Sebastian Eckert, and many more.

At day and night, I could count on the support from the staff of the Helmholtz-Zentrum Berlin, whether it be a flange, a rushing order for the workshop, or just some mussel power to lift the heavy concrete blocks.

Piter Miedema was so kind to perform some basic calculations on the metal carbonyls in the ground state.

I will not forget the fantastic moral support of my fellow PhD students Markus Kubin, Markus Hantschmann, Nele Thielemann-Kühn, and Sergej Solopow.

I would also like to thank Prof. Simone Techert and Dr. Tim Laarmann for the review of this thesis, as well as Prof. Markus Gühr, Prof. Dieter Neher, and Prof. Oliver Rader for completing the committee.

The love and support by family and friends have made all this possible. For this, I am especially grateful to Francesca Tosin, Marc Cyr, Johannes Mebert, Martin von Helversen, Til Bartel, and Oliver Neitzke.

Thank you all

Bibliography

[1] M. Appl, in *Ullmann's encyclopedia of industrial chemistry* (Wiley-VCH Verlag GmbH & Co. KGaA, Weinheim, Germany, 2006).

[2] M. D. Fryzuk, „Inorganic chemistry: Ammonia transformed", Nature **427**, 498 (2004).

[3] J. Yano and V. Yachandra, „Mn 4 Ca Cluster in Photosynthesis: Where and How Water is Oxidized to Dioxygen", Chemical Reviews **114**, 4175 (2014).

[4] A. H. Zewail, „Femtochemistry: Atomic-Scale Dynamics of the Chemical Bond", The Journal of Physical Chemistry A **104**, 5660 (2000).

[5] P. D. B. König, ed., *Chemical Photocatalysis* (DE GRUYTER, 2013).

[6] S. A. Macgregor, O. Eisenstein, M. K. Whittlesey, and R. N. Perutz, „A theoretical study of [M(PH3)4] (M = Ru or Fe), models for the highly reactive d8 intermediates [M(dmpe)2] (dmpe = Me2PCH2CH2PMe2). Zero activation energies for addition of CO and oxidative addition of H2", Journal of the Chemical Society, Dalton Transactions, 291 (1998).

[7] R. Asatryan and E. Ruckenstein, „Mechanism of iron carbonyl-catalyzed hydrogenation of ethylene. 1. Theoretical exploration of molecular pathways.", The journal of physical chemistry. A **117**, 10912 (2013).

[8] M. Poliakoff and J. J. Turner, „Die Struktur von [Fe(CO)4] - ein neues Kapitel einer langen Geschichte", Angewandte Chemie **113**, 2889 (2001).

[9] S. A. Trushin, W. Fuss, K. L. Kompa, and W. E. Schmid, „Femtosecond Dynamics of Fe(CO) 5 Photodissociation at 267 nm Studied by Transient Ionization", The Journal of Physical Chemistry A **104**, 1997 (2000).

[10] C. Nordling, E. Sokolowski, and K. Siegbahn, „EVIDENCE OF CHEMICAL SHIFTS OF THE INNER ELECTRONIC LEVELS IN A METAL RELATIVE TO ITS OXIDES (CU, CU2O, CUO)", Arkiv for Fysik **13**, 483 (1958).

[11] E. Sokolowski, C. Nordling, and K. Siegbahn, „Chemical Shift Effect in Inner Electronic Levels of Cu Due to Oxidation", Physical Review **110**, 776 (1958).

[12] D. W. Turner and M. I. A. Jobory, „Determination of Ionization Potentials by Photoelectron Energy Measurement", The Journal of Chemical Physics **37**, 3007 (1962).

[13] T. D. Thomas, „X-Ray Photoelectron Spectroscopy of Carbon Monoxide", The Journal of Chemical Physics **53**, 1744 (1970).

[14] J. H. Eland, *Photoelectron spectroscopy : an introduction to ultraviolet photo-electron spectroscopy in the gas phase* (London : Butterworth, 1974).

[15] J.-C. Diels, *Ultrashort LaserPulse Phenomena* (2006).

[16] C. Rullière, ed., *Femtosecond Laser Pulses*, Advanced Texts in Physics (Springer New York, New York, NY, 2005).

[17] M. Wollenhaupt, A. Assion, and T. Baumert, in *Springer handbook of lasers and optics* (Springer New York, New York, NY, 2007).

[18] T. H. Maiman, „Stimulated Optical Radiation in Ruby", Nature **187**, 493 (1960).

[19] P. A. Franken, A. E. Hill, C. W. Peters, and G. Weinreich, „Generation of Optical Harmonics", Physical Review Letters **7**, 118 (1961).

[20] R. W. Boyd, *Nonlinear Optics*, Nonlinear Optics Series (Elsevier Science, 2008).

[21] J.-y. Zhang, J. Y. Huang, H. Wang, K. S. Wong, and G. K. Wong, „Second-harmonic generation from regeneratively amplified femtosecond laser pulses in BBO and LBO crystals", Journal of the Optical Society of America B **15**, 200 (1998).

[22] M. Brass, *Handbook of optics: v.1: Fundamentals, techniques, and design*, Vol. 32, 10 (1995).

[23] S. Ghimire, A. D. DiChiara, E. Sistrunk, P. Agostini, L. F. DiMauro, and D. A. Reis, „Observation of high-order harmonic generation in a bulk crystal", Nature Physics **7**, 138 (2011).

[24] M. Hohenleutner, F. Langer, O. Schubert, M. Knorr, U. Huttner, S. W. Koch, M. Kira, and R. Huber, „Real-time observation of interfering crystal electrons in high-harmonic generation", Nature **523**, 572 (2015).

[25] G. H. C. New and J. F. Ward, „Optical Third-Harmonic Generation in Gases", Physical Review Letters **19**, 556 (1967).

[26] A. McPherson, G. Gibson, H. Jara, U. Johann, T. S. Luk, I. A. McIntyre, K. Boyer, and C. K. Rhodes, „Studies of multiphoton production of vacuum-ultraviolet radiation in the rare gases", Journal of the Optical Society of America B **4**, 595 (1987).

[27] A. L'Huillier and P. Balcou, „High-order harmonic generation in rare gases with a 1-ps 1053-nm laser", Physical Review Letters **70**, 774 (1993).

[28] C. Spielmann and H. Zacharias, „Extrem harmonisch", Physik Journal **11**, 37 (2012).

[29] P. B. Corkum, „Plasma perspective on strong field multiphoton ionization", Physical Review Letters **71**, 1994 (1993).

[30] L. V. Keldysh, „Ionization in the field of a string electromagnetic wave", Journal of Experimental and Theoretical Physics **20**, 1307 (1965).

[31] I. Shchatsinin, „Free Clusters and Free Molecules in Strong , Shaped Laser Fields", PhD thesis (Freie Universität Berlin, 2009).

[32] A. Rundquist, „Phase-Matched Generation of Coherent Soft X-rays", Science **280**, 1412 (1998).

[33] C. Winterfeldt, C. Spielmann, and G. Gerber, „Colloquium: Optimal control of high-harmonic generation", Reviews of Modern Physics **80**, 117 (2008).

[34] T. Pfeifer, C. Spielmann, and G. Gerber, „Femtosecond x-ray science", Reports on Progress in Physics **69**, 443 (2006).

[35] T. Leitner, „Ultrafast processes in molecules visualized with femtosecond pump-probe photoelectron spectroscopy", PhD thesis (Technische Universität Berlin, 2012).

[36] P. Wernet, J. Gaudin, K. Godehusen, O. Schwarzkopf, and W. Eberhardt, „Femtosecond time-resolved photoelectron spectroscopy with a vacuum-ultraviolet photon source based on laser high-order harmonic generation.", The Review of scientific instruments **82**, 063114 (2011).

[37] I. Velchev, W. Hogervorst, and W. Ubachs, „Precision VUV spectroscopy of Ar I at 105 nm", Journal of Physics B: Atomic, Molecular and Optical Physics **32**, L511 (1999).

[38] E. B. Saloman, „Energy Levels and Observed Spectral Lines of Xenon, Xe I through Xe LIV", Journal of Physical and Chemical Reference Data **33**, 765 (2004).

[39] F. Brandi, I. Velchev, W. Hogervorst, and W. Ubachs, „Vacuum-ultraviolet spectroscopy of Xe: Hyperfine splittings, isotope shifts, and isotope-dependent ionization energies", Physical Review A **64**, 032505 (2001).

[40] R. D. Knight and L.-g. Wang, „One-photon laser spectroscopy of the np and nf Rydberg series in xenon", Journal of the Optical Society of America B **2**, 1084 (1985).

[41] T. Leitner, A. A. Sorokin, J. Gaudin, H. Kaser, U. Kroth, K. Tiedtke, M. Richter, and P. Wernet, „Shot-to-shot and average absolute photon flux measurements of a femtosecond laser high-order harmonic photon source", New Journal of Physics **13**, 0 (2011).

[42] V. Ulrich, S. Barth, T. Lischke, S. Joshi, T. Arion, M. Mucke, M. Förstel, A. M. Bradshaw, and U. Hergenhahn, „Photoelectron-Auger electron coincidence spectroscopy of free molecules: New experiments", Journal of Electron Spectroscopy and Related Phenomena **183**, 70 (2011).

[43] K. Kimura, *Handbook of HeI photoelectron spectra of fundamental organic molecules: ionization energies, ab initio assignments, and valence electronic structure for 200 molecules* (John Wiley & Sons Inc, 1981).

[44] C. Iaconis and I. Walmsley, „Spectral phase interferometry for direct electric-field reconstruction of ultrashort optical pulses", in Technical digest. summaries of papers presented at the conference on lasers and electro-optics. conference edition. 1998 technical digest series, vol.6 (ieee cat. no.98ch36178), Vol. 23, 10 (1998).

[45] C. Iaconis and I. Walmsley, „Self-referencing spectral interferometry for measuring ultrashort optical pulses", IEEE Journal of Quantum Electronics **35** (1999).

[46] R. Trebino, K. W. DeLong, D. N. Fittinghoff, J. N. Sweetser, M. A. Krumbügel, B. A. Richman, and D. J. Kane, „Measuring ultrashort laser pulses in the time-frequency domain using frequency-resolved optical gating", Review of Scientific Instruments **68**, 3277 (1997).

[47] P. O'Shea, M. Kimmel, and R. Trebino, „Increased phase-matching bandwidth in simple ultrashort-laser-pulse measurements", Journal of Optics B: Quantum and Semiclassical Optics **4** (2002).

[48] T. E. Glover, R. W. Schoenlein, A. H. Chin, and C. V. Shank, „Observation of Laser Assisted Photoelectric Effect and Femtosecond High Order Harmonic Radiation", Physical Review Letters **76**, 2468 (1996).

[49] A. Bouhal, R. Evans, G. Grillon, A. Mysyrowicz, P. Breger, P. Agostini, R. C. Constantinescu, H. G. Muller, and D. von der Linde, „Cross-correlation measurement of femtosecond noncollinear high-order harmonics", Journal of the Optical Society of America B **14**, 950 (1997).

[50] A. Visco, R. P. Drake, D. H. Froula, S. H. Glenzer, and B. B. Pollock, „Temporal dispersion of a spectrometer", Review of Scientific Instruments **79**, 10F545 (2008).

[51] B. Frietsch, R. Carley, K. Döbrich, C. Gahl, M. Teichmann, O. Schwarzkopf, P. Wernet, and M. Weinelt, „A high-order harmonic generation apparatus for time- and angle-resolved photoelectron spectroscopy.", The Review of scientific instruments **84**, 075106 (2013).

[52] O. Krupin et al., „Temporal cross-correlation of x-ray free electron and optical lasers using soft x-ray pulse induced transient reflectivity", Optics Express **20**, 11396 (2012).

[53] B. Di Bartolo and O. Forte, eds., *Advances in Spectroscopy for Lasers and Sensing* (Springer Netherlands, Dordrecht, 2006).

[54] L. Bergmann and C. Schaefer, *Lehrbuch der Experimentalphysik, Band 6: Festkörper*, edited by R. Kassing (Walter de Gruyter, 2005).

[55] A. Verma, D. Hirsch, C. Glatt, G. Ronnett, and S. Snyder, „Carbon monoxide: a putative neural messenger", Science **259**, 381 (1993).

[56] B. Olas, „Carbon monoxide is not always a poison gas for human organism: Physiological and pharmacological features of CO", Chemico-Biological Interactions **222**, 37 (2014).

[57] T. Lee, F. Benesch, Y. Jiang, and C. G. Rose-Petruck, „Structure of solvated Fe(CO)5: XANES and EXAFS measurements using ultrafast laser plasma and conventional X-ray sources", Chemical Physics **299**, 233 (2004).

[58] L. Mond, C. Langer, and F. Quincke, „L.-Action of carbon monoxide on nickel", Journal of the Chemical Society, Transactions **57**, 749 (1890).

[59] I. Langmuir, „TYPES OF VALENCE", Science **54**, 59 (1921).

[60] K. Nakamoto, *Infrared and Raman Spectra of Inorganic and Coordination Compounds* (John Wiley & Sons, Inc., Hoboken, NJ, USA, 2008).

[61] P. Atkins, T. Overton, J. Rourke, M. Weller, and F. Armstrong, *Shriver and Atkins' Inorganic Chemistry* (OUP Oxford, 2014).

[62] R. K. Hocking and T. W. Hambley, „Database Analysis of Transition Metal Carbonyl Bond Lengths: Insight into the Periodicity of π Back-Bonding, σ Donation, and the Factors Affecting the Electronic Structure of the TM-CO Moiety", Organometallics **26**, 2815 (2007).

[63] S. Katsuki, H. Taketa, and M. Inokuchi, „The Effect of the 3d Transition Metal Substrates on Dissociative Property of the Adsorbed Carbon Monoxide Studied by the Model Potential Xα Method", Journal of the Physical Society of Japan **52**, 2156 (1983).

[64] C. Elschenbroich, *Organometallics* (Wiley-VCH, 2006).

[65] T. Jazzazi, „CO-Sources for the liberation of cellular messenger molecules", PhD thesis (Friedrich-Schiller-Universität Jena, 2013).

[66] R. H. Crabtree, *The Organometallic Chemistry of the Transition Metals* (John Wiley & Sons, Inc., Hoboken, NJ, USA, 2005).

[67] K. P. Huber and G. Herzberg, *Molecular Spectra and Molecular Structure* (Springer US, Boston, MA, 1979).

[68] M. Assefa, J. Devera, A. Brathwaite, J. Mosley, and M. Duncan, „Vibrational scaling factors for transition metal carbonyls", Chemical Physics Letters **640**, 175 (2015).

[69] O. R. Gilliam, C. M. Johnson, and W. Gordy, „Microwave Spectroscopy in the Region from Two to Three Millimeters", Physical Review **78**, 140 (1950).

[70] D. Schmidling, „An electron-diffraction study of the molecular structure of vanadium hexacarbonyl", Journal of Molecular Structure **24**, 1 (1975).

[71] A. Jost, B. Rees, and W. B. Yelon, „Electronic structure of chromium hexacarbonyl at 78 K. I. Neutron diffraction study", Acta Crystallographica Section B Structural Crystallography and Crystal Chemistry **31**, 2649 (1975).

[72] M. R. Churchill, K. N. Amoh, and H. J. Wasserman, „Redetermination of the crystal structure of dimanganese decacarbonyl and determination of the crystal structure of dirhenium decacarbonyl. Revised values for the manganese-manganese and rhenium-rhenium bond lengths in dimanganese decacarbonyl and dirheniu", Inorganic Chemistry **20**, 1609 (1981).

[73] B. Beagley and D. Schmidling, „A re-evaluation of the molecular structure of iron pentacarbonyl", Journal of Molecular Structure **22**, 466 (1974).

[74] G. G. Sumner, H. P. Klug, and L. E. Alexander, „The crystal structure of dicobalt octacarbonyl", Acta Crystallographica **17**, 732 (1964).

[75] L. Hedberg, T. Iijima, and K. Hedberg, „Nickel tetracarbonyl, Ni(CO)4. I. Molecular structure by gaseous electron diffraction. II. Refinement of quadratic force field", The Journal of Chemical Physics **70**, 3224 (1979).

[76] S. P. Arnesen, H. M. Seip, K. Siegbahn, E. Stenhagen, B. Sjöberg, E. Bunnenberg, C. Djerassi, and R. Records, „Studies on the Failure of the First Born Approximation in Electron Diffraction. V. Molybdenum- and Tungsten Hexacarbonyl.", Acta Chemica Scandinavica **20**, 2711 (1966).

[77] M. Dartiguenave, Y. Dartiguenave, and H. B. Gray, „Spectre Electronique du fer Pentacarbonyle-Etude Theorique et Experimentale", lletin de la Societe Chimique de France, Bu, 4223 (1969).

[78] M. Kotzian, N. Roesch, H. Schroeder, and M. C. Zerner, „Optical spectra of transition-metal carbonyls: chromium hexacarbonyl, iron pentacarbonyl, and nickel tetracarbonyl", Journal of the American Chemical Society **111**, 7687 (1989).

[79] O. Rubner, V. Engel, M. R. Hachey, and C. Daniel, „A CASSCF/MR-CCI study of the excited states of Fe (CO) 5", Chemical Physics Letters **302**, 489 (1999).

[80] P. Wernet et al., „Orbital-specific mapping of the ligand exchange dynamics of Fe(CO)5 in solution", Nature **520**, 78 (2015).

[81] K. Kunnus, I. Josefsson, I. Rajkovic, S. Schreck, W. Quevedo, M. Beye, C. Weniger, S. Grübel, M. Scholz, D. Nordlund, W. Zhang, R. Hartsock, K. Gaffney, W. Schlotter, J. Turner, F. Brian Kennedy, and A. Föhlisch, „Identification of the dominant photochemical pathways and mechanistic insights to the ultrafast ligand exchange of Fe(CO)5 to Fe(CO)4EtOH", Structural Dynamics (in press) (2016).

[82] K. E. Lewis, D. M. Golden, and G. P. Smith, „Organometallic Bond Dissociation Energies : Laser Pyrolysis", J. Am. Chem. Soc. **106**, 3905 (1984).

[83] P. C. Engelking and W. C. Lineberger, „Laser photoelectron spectrometry of the negative ions of iron and iron carbonyls. Electron affinity determination for the series Fe(CO)n, n= 0, 1, 2, 3, 4", Journal of the American Chemical Society **101**, 5569 (1979).

[84] J. T. Yardley, B. Gitlin, G. Nathanson, and A. M. Rosan, „Fragmentation and molecular-dynamics in the laser photo-dissociation of iron pentacarbonyl", J. Chem. Phys. **74**, 370 (1981).

[85] M. Poliakoff and E. Weitz, „Shedding light on organometallic reactions: the characterization of tetracarbonyliron (Fe(CO)4), a prototypical reaction intermediate", Accounts of Chemical Research **20**, 408 (1987).

[86] L. Bañares, T. Baumert, M. Bergt, B. Kiefer, and G. Gerber, „Femtosecond photodissociation dynamics of Fe(CO)5 in the gas phase", Chemical Physics Letters **267**, 141 (1997).

[87] L. Bañares, T. Baumert, M. Bergt, B. Kiefer, and G. Gerber, „The ultrafast photodissociation of Fe(CO)[sub 5] in the gas phase", The Journal of Chemical Physics **108**, 5799 (1998).

[88] P. T. Snee, C. K. Payne, S. D. Mebane, K. T. Kotz, and C. B. Harris, „Dynamics of Photosubstitution Reactions of Fe(CO) 5 : An Ultrafast Infrared Study of High Spin Reactivity", Journal of the American Chemical Society **123**, 6909 (2001).

[89] S. Trushin, K. Kosma, W. Fuß, and W. E. Schmid, „Wavelength-independent ultrafast dynamics and coherent oscillation of a metal-carbon stretch vibration in photodissociation of Cr(CO)6 in the region of 270-345nm", Chemical Physics **347**, 309 (2008).

[90] M. Poliakoff and A. Ceulemans, „IR laser induced isomerization of iron tetracarbonyl (Fe(CO)4): a unique example of the Jahn-Teller effect", Journal of the American Chemical Society **106**, 50 (1984).

[91] R. Fukuda, M. Ehara, H. Nakatsuji, N. Kishimoto, and K. Ohno, „Valence ionized states of iron pentacarbonyl and eta5-cyclopentadienyl cobalt dicarbonyl studied by symmetry-adapted cluster-configuration interaction calculation and collision-energy resolved Penning ionization electron spectroscopy.“, The Journal of chemical physics **132**, 084302 (2010).

[92] P. Wernet, T. Leitner, I. Josesfsson, T. Mazza, H. Schröder, M. Beye, K. Kunnus, S. Schreck, P. Radcliffe, S. Düsterer, M. Meyer, M. Odelius, and A. Föhlisch, „Mapping ligand coordination, spin and electron density changes in Fe(CO)5 dissociation with x-ray laser spectroscopy“, (in manuscript).

[93] H. Ihee, J. Cao, and A. H. Zewail, „Ultrafast electron diffraction of transient [Fe(Co)4]: Determination of molecular structure and reaction pathway“, Angewandte Chemie - International Edition **40**, 1532 (2001).

[94] E. Baerends and P. Ros, „The electronic structure of transition metal carbonyl complexes“, Molecular Physics **30**, 1735 (1975).

[95] E. Baerends, C. Oudshoorn, and A. Oskam, „Photoelectron spectra and Xα calculations of iron pentacarbonyl and ethyleneiron tetracarbonyl“, Journal of Electron Spectroscopy and Related Phenomena **6**, 259 (1975).

[96] S. Trushin, W. Fuß, and W. E. Schmid, „Conical intersections, pseudorotation and coherent oscillations in ultrafast photodissociation of group-6 metal hexacarbonyls“, Chemical Physics **259**, 313 (2000).

[97] M. Wrighton and V. Carassiti, „Organometallic Photochemistry“, Inorganica Chimica Acta **42**, 146 (1980).

[98] S. Villaume, A. Strich, C. Daniel, S. A. Perera, and R. J. Bartlett, „A coupled cluster study of the electronic spectroscopy and photochemistry of Cr(CO)6.“, Physical chemistry chemical physics : PCCP **9**, 6115 (2007).

[99] R. Crespo-Otero and M. Barbatti, „Cr(CO)6 photochemistry: Semi-classical study of UV absorption spectral intensities and dynamics of photodissociation“, The Journal of Chemical Physics **134**, 164305 (2011).

[100] B. R. Higginson, D. R. Lloyd, P. Burroughs, D. M. Gibson, and A. F. Orchard, „Photoelectron studies of metal carbonyls. Part 2. - The valence region photoelectron spectra of the group VIA hexacarbonyls“, Journal of the Chemical Society, Faraday Transactions 2 **69**, 1659 (1973).

[101] A. Nilsson, N. Mårtensson, S. Svensson, L. Karlsson, D. Nordfors, U. Gelius, and H. Ågren, „High resolution x-ray photoelectron spectroscopy study of Cr(CO)6 in the gas phase“, The Journal of Chemical Physics **96**, 8770 (1992).

[102] D. R. Lloyd and E. W. Schlag, „Photoionization studies of metal carbonyls. I. Ionization potentials and the bonding in Group VI metal hexacarbonyls and in mononuclear carbonyls and nitrosyl carbonyls of iron, cobalt, and nickel“, Inorganic Chemistry **8**, 2544 (1969).

[103] M. Ohno, W. von Niessen, and F. Tarantelli, „Many-body calculation of the valence photoemission spectrum of Cr(CO)6“, Physical Review B **45**, 1851 (1992).

[104] S. A. Trushin, W. Fuss, W. E. Schmid, and K. L. Kompa, „Femtosecond Dynamics and Vibrational Coherence in Gas-Phase Ultraviolet Photodecomposition of Cr(CO) 6“, The Journal of Physical Chemistry A **102**, 4129 (1998).

[105] M. J. Paterson, P. A. Hunt, M. A. Robb, and O. Takahashi, „Non-adiabatic direct dynamics study of chromium hexacarbonyl photodissociation", Journal of Physical Chemistry A **106**, 10494 (2002).

[106] C. Pollak, A. Rosa, and E. J. Baerends, „Cr-CO Photodissociation in Cr(CO)6 : Reassessment of the Role of Ligand-Field Excited States in the Photochemical Dissociation of Metal-Ligand Bonds", Journal of the American Chemical Society **119**, 7324 (1997).

[107] L. Yang, H. Ågren, L. G. M. Pettersson, J. Guo, C. Såthe, A. Föhlisch, A. Nilsson, and J. Nordgren, „Core Electron Spectroscopy of Chromium Hexacarbonyl. A Comparative Theoretical and Experimental Study", Physica Scripta **59**, 138 (2006).

[108] K. Kosma, S. A. Trushin, W. Fuss, W. E. Schmid, and B. M. R. Schneider, „Photodissociation of group-6 hexacarbonyls: observation of coherent oscillations in an antisymmetric (pseudorotation) vibration in Mo(CO)(5) and W(CO)(5).", Physical chemistry chemical physics : PCCP **12**, 13197 (2010).

[109] P. Wernet, M. Odelius, K. Godehusen, J. Gaudin, O. Schwarzkopf, and W. Eberhardt, „Real-Time Evolution of the Valence Electronic Structure in a Dissociating Molecule", Physical Review Letters **103**, 013001 (2009).

Sworn declaration
Eidesstattliche Erklärung

I declare under penalty of perjury that I have authored this thesis independently and that I have used no other than the declared resources.
The current or a similar version of this thesis has not been submitted to another university neither has it been used in another exam.

Ich erkläre an Eides statt, dass ich die vorliegende Dissertation selbstständig und eigenhändig verfasst sowie keine anderen als die angegebenen Quellen und Hilfsmittel genutzt habe.
Diese Doktorarbeit wurde in der jetzigen oder einer ähnlichen Form noch bei keiner anderen Hochschule eingereicht und hat noch keinen sonstigen Prüfungszwecken gedient.

_____

Henning Schröder